

**Molecular Behavior of Surfactants in
Structural Formation of Low-Water Content
Lamellae and Solubilization Phenomena of
Mixed Micelles**

Kosuke Takeda

2019

Table of Contents

<i>General Introduction</i>	5
<i>Chapter 1. Structure of Hydrated Crystal (L_c), Tilted Gel ($L_{\beta'}$), and Liquid Crystal (L_a) Phases of Linear Alkylbenzene Sulfonate (LAS) Studied by X-ray Diffraction and Molecular Dynamics Simulation</i>	13
1.1. Introduction	13
1.2. Experiment and Simulation Details	15
<i>Sample Preparation and XRD Experiment.</i>	15
<i>Molecular Dynamics Simulation.</i>	16
1.3. Results and Discussion	19
<i>XRD Experiment</i>	19
<i>Comparison of the Experimental and Simulated XRD Patterns</i>	21
<i>Crystal Structures of Other than the Monohydrate System</i>	24
<i>Structural Change Caused by Thermally Induced Phase Transition of LAS</i>	27
1.4. Conclusions	30
<i>Chapter 2. Molecular Behavior of Linear Alkylbenzene Sulfonate in Hydrated Crystal, Tilted Gel, and Liquid Crystal Phases Studied by Molecular Dynamics Simulation</i>	47
2.1. Introduction	47
2.2. Simulation details	49
2.3. Results and Discussion	50
<i>Lateral Diffusion</i>	50
<i>Reorientation of LAS</i>	52
<i>Conformation of Alkyl Chain</i>	55
<i>Origin of Odd-even Effect</i>	58
2.4. Conclusions	60

<i>Chapter 3. Molecular dynamics study of solubilization of cyclohexane, benzene, and phenol into mixed micelles composed of sodium dodecyl sulfate and octaethylene glycol monododecyl ether</i> -----	75
3.1. Introduction -----	75
3.2. Simulation details -----	77
3.3. Results and Discussion -----	79
<i>Structure of mixed micelle</i> -----	79
<i>Hydrophilic group</i> -----	80
<i>Hydrophobic core</i> -----	83
<i>Free energy profiles $\Delta G(r)$ of solute molecules</i> -----	84
<i>Validity of free energy profile calculation</i> -----	84
<i>Stable binding site of solute molecules to mixed micelle</i> -----	85
<i>Surfactant composition dependence of $\Delta G(r)$</i> -----	87
3.4 Conclusions -----	88
<i>Conclusion</i> -----	103
<i>References</i> -----	106
<i>List of Publications</i> -----	120
<i>Acknowledgements</i> -----	121

General Introduction

Understanding of the physicochemical properties of surfactant self-assembly is of key importance in many industrial applications. One of the most important applications of surfactants is the use in detergents. For new detergent development, many technical requirements are raised; e.g., how to improve washing performance, how to prevent dirt from reattaching to clothes,¹ how to control foaming/defoaming,^{2,3} and how to add antimicrobial properties,^{4,5} and so on. Even though these technical issues are closely related to the physicochemical nature of the surfactant molecular self-assembly, product design has hardly been based on molecular theory and current detergent developments still have to rely on trial and error. In this dissertation, we investigate two major technical aspects of surfactant self-assembly in the detergent application using molecular dynamics (MD) simulations, (1) long term stabilization⁶ and (2) improvement of detergency, which are the most basic properties and important for detergent reliability. Here, we analyzed molecular configuration and behavior of the surfactants to contribute to the molecular design of detergents.

Long term stabilization of detergent as a homogeneous liquid is required during manufacturing, transportation, and preservation. Hydrated crystal with low-water content lamellar (L_c phase) precipitates below a temperature known as the Krafft point. The precipitation occurred in a cold climate is unfavorable for liquid detergent since it causes turbidity and solidification. To achieve long term stabilization of the detergents, we need to avoid the precipitation of surfactant crystals. However, the detailed structure of L_c phase

which causes the precipitation has not been clarified so far. Thus, first of all, understanding and characterization of the L_c phase should be required. Then, the phase behavior of surfactant assembly should be investigated. The L_c phase has highly oriented molecular axis with all-*trans* conformation of alkyl chain. At higher temperatures, we obtain relatively disordered sub-phases, such as, gel (L_β), tilted gel ($L_{\beta'}$), and liquid crystal (L_α) phases.⁷ If specific molecular topologies and/or interactions in the L_c phase, which is the main cause of the precipitation, are clarified by determining the lamellar structures and understanding differences of these molecular dynamics, the first technical aspect is expected to be solved.

The improvement of detergency, which is closely related to an enhanced “solubilization” (incorporation of hydrophobic dirt into surfactants micelles⁸⁻¹⁰), is highly required. In order to improve the detergent function, mixing of different surfactant species are often adopted in a practical application. By the mixing, surface tension and critical micelle concentration (CMC) can be decreased,^{8,11} which means that high detergency is achieved with low surfactant content. Also, the actual dirt is often consists of various polar components such as lipids, proteins, and bacteria. Since performance of the detergents depends on the polarity of the solute to be solved, systematic understanding of the complex solubilization behavior of the mixed micelles is required as a function of the mixing ratio of surfactants. The knowledge must contribute much to the design of surfactant mixtures tailored to the cleaning target.

We aimed to clarify the details of molecular structure and behavior of the surfactants and to obtain information based on molecular theory which can work as a development

guideline of new detergents. Here, we carried out MD simulations for the hydrated crystal and mixed micelle systems.

In Chapter 1 and 2, we investigate structure of low-water content lamellae composed of sodium linear alkylbenzene sulfonate (LAS), the most commonly used surfactant in industry. Determination of accurate molecular configuration in the L_c phase precipitated in solution is not straightforward. The accurate molecular configurations have been reported for a few surfactants for various water content, temperature, and pressure. For example, sodium dodecyl sulfate (SDS) has been found to form dihydrate ($\text{SDS}\cdot 2\text{H}_2\text{O}$),⁷ monohydrate ($\text{SDS}\cdot 1\text{H}_2\text{O}$),¹² hemihydrate ($\text{SDS}\cdot \frac{1}{2}\text{H}_2\text{O}$),¹³ $\frac{1}{8}$ hydrate¹⁴ and anhydrate ($\text{SDS}\cdot 0\text{H}_2\text{O}$)¹⁵ as the water content decreases. A determination of the single crystal structure succeeded for anionic surfactants,^{12–14,16} glycolipids,^{17–23} aliphatic acids^{24,25} and phospholipids²⁶ in the L_c phase by single crystal X-ray diffraction (XRD). However, in spite of the importance of LAS as one of the most commonly used liquid detergents, its single crystal structure in the L_c phase has not yet been determined.

“Powder” XRD techniques have been applied to structural analysis of polycrystalline, and they have been successful for inorganic materials. In contrast, the polycrystalline of organic material including the surfactants with low symmetry, the structural identification is difficult due to peak overlap in the diffraction pattern. Smith et al. determined anhydrous crystal structure of SDS¹⁵ using synchrotron powder XRD with systematic trial structure determination for subsequent Rietveld refinement.²⁷ Then, a single crystal of hemihydrate was required as the initial configuration to perform the structural determination. Instead of the trial structure determination procedure, MD simulation can be employed since we are

also interested in the local molecular structures and dynamics of the system after the thermally induced phase transition such as the L_β or L_α phase as described in Chapter 2.

There are two major issues to be overcome to conduct MD simulation of hydrated surfactants in the L_c phase. First, an accurate hydration number of the crystalline surfactant should be obtained. In the L_c phase, a fixed number of water molecules are included in a unit lattice of the hydrated crystal of the surfactant.⁹ Unfortunately, the hydration number of the crystal has not been determined for LAS or many other surfactants. Further, the hydration number may change when a phase transition to the L_β or the L_α takes place.²⁸ Then, the excluded water may come into the hydrophilic inter-bilayer regions. Therefore, a possible change in the hydration number caused by the phase transition should be taken into account in the MD simulation. The second is the initial configuration. Typically, it takes several hours or days to crystallize the hydrated surfactants even experimentally owing to their low structural symmetry. Thus, spontaneous formation of surfactant self-assembly in the L_c phase cannot be expected in the simulation time. Therefore, we must assume the initial configuration to start the MD simulation including the number of water molecules involved in the crystal.

We investigate, in Chapter 1, we solved these two issues with the aid of XRD pattern as reference data in a similar way to other studies on inorganic materials²⁹ and cellulose crystals.³⁰ A series of MD simulations starting from possible LAS crystalline structures have been carried out with five different hydration levels (anhydrate hemi-, mono-, di-, and tetrahydrates) under ambient condition. Further, to understand the structural change during thermally induced phase transition from the L_c to relatively disordered subphases,

additional MD simulations with heating have been performed, and we discuss the disordered structures by comparing with the XRD experiment.

We also investigate the phase behavior of surfactant assembly of LAS in the L_c , $L_{\beta'}$, and L_{α} phases. As discussed in Chapter 1, lamellar structures show various subphases depending on their molecular orientation and dynamics. In the L_c phase, at the lowest temperature, the alkyl groups are regularly arranged in the all-*trans* conformation. A stoichiometric number of water molecules are arranged as hydrating water around the hydrophilic groups of the surfactant.^{7,12,23–25,31,32,13,16–22} In this phase, lateral translational diffusion as well as reorientation attributed to twisting motion around the molecular axis are extremely slow.⁹ In the L_{β} phase, at higher temperatures, conformation of the alkyl groups remains almost all-*trans*. Surfactant molecules in the L_{β} phase show no lateral diffusion, though they show reorientation.^{33,28} In $L_{\beta'}$ phase, surfactant molecules are inclined with respect to the bilayer normal.^{34–36} In the L_{α} phase, at the highest temperature, lateral arrangement of the surfactant molecules and conformation of the alkyl groups are disordered. Surfactant molecules have high mobility with respect to lateral translation and reorientation, and thus the phase exhibits macroscopic fluidity.³⁷ However, the conformation of the surfactants in these lamellar phases is still not fully understood.

Sperline et al. investigated the conformation of SDS^{38–40} and LAS^{41,42} in the L_c phase using infrared spectroscopy (FT-IR) and linear dichroism (LD) measurements. SDS in the L_c phase of a monohydrate crystal has a *gauche* conformation at the alkyl chain segment bound to the OSO_3^- group, whereas it has an all-*trans* conformation in a crystal with different hydration numbers. SDS³⁹ and LAS⁴¹ in the $L_{\beta'}$ phase have alkyl groups inclined

by about 45° with respect to the bilayer normal. It is supposed that the double *gauche* conformation produces a uniform tilt of the alkyl chains, which may allow the surfactant molecules in the $L_{\beta'}$ phase to twist with very low translational diffusivity. A MD simulation study on dipalmitoyl phosphatidylcholine (DPPC) bilayers by Tu et al. tried to investigate a relationship between chain conformation and reorientation in the $L_{\beta'}$ phase.³⁵ It has also been reported that the *gauche* conformation is reduced for SDS and LAS in the L_α phase adsorbed on an Al_2O_3 surface, which is attributed to the strong electrostatic interaction between the head groups (OSO_3^- or SO_3^-) of the surfactants and the matrix surface.^{40,42} We can thus expect that a similar reduction of the *gauche* conformation may occur in the bulk L_α phase with a lower hydration number through salt-bridging among the head groups of the surfactant via counter ions. However, within our knowledge, this has not been previously reported.

In Chapter 2, we investigate the difference of molecular dynamics in the L_c , $L_{\beta'}$, and L_α phases based on 1 μs long MD trajectories. The initial configurations of these phases in this simulation were adopted which obtained by combining XRD and MD simulation in Chapter 1. Further, the differences in terms of lateral translation, reorientation, and conformation patterns of alkyl chain have been analyzed. Then, we discuss the difference in molecular configuration and its behavior that can lead to the precipitation of L_c phase.

In Chapter 3, we investigate solubilization phenomena of mixed micelles composed of several mixing ratios of sodium dodecyl sulfate (SDS) and octaethyleneglycol monododecyl ether (C_{12}E_8). Decrease in surface tension and CMC by the mixing of the surfactants is called synergistic effect. It is explained by non-ideal liquid theory, where a

parameter of intermolecular interaction β is negative, i.e. attractive interaction between different surfactants suggested by Rosen et al.^{43,44} The β has been investigated for several combinations of surfactants.⁸ Furthermore, it has been reported that solubilization is also affected by the species of mixing surfactants.^{45,46} However, there has been no research focusing on the solute molecules in mixed micelles where special interactions may be found.

MD simulations can be used to clarify the influence of mixing of the surfactants on solubilization from a microscopic viewpoint. Though, in fact, they have been applied to the investigation of solubilization in many studies,^{47,48,57,49-56} However, few of them considered mixed micelles, possibly because there are few experimental data on their aggregation number and composition. Mehling et al. have reported systematically prediction studies of partition coefficients of ionizable solutes, $\log P$ and $\log D$, between mixed nonionic/ionic micelles and water by COSMO-RS method.⁵⁸ The predicted values have showed good agreement with some experiments. However, COSMO-RS itself does not present microscopic information of solubilization but estimate $\log P$ values using the information obtained by MD calculations. In order to investigate molecular behavior of the solubilization, that is, microscopic origin of the $\log P$ values, we must conduct MD calculations.

We examine a mixed micelle composed of SDS and C₁₂E₈, for which the aggregation number is known from experiments. The MD simulations were carried out to examine solubilization at various SDS/C₁₂E₈ compositions. From the MD simulations at each composition, the corresponding equilibrium micelle structure was obtained. Then, the free

energy profile, $\Delta G(r)$, for the solubilization of solute molecules from the bulk water into the micelle center was calculated using the thermodynamics integration method based on MD simulations. To focus on the relationship between the molecular interactions and solubilization of solute molecules, the cyclic compounds, cyclohexane, benzene, and phenol, which commonly consist of six carbons (C_6) with similar molecular size and different polarities were examined. Based on $\Delta G(r)$, we discuss the relationship between the solubilization of the solute molecules and the mixing state of the surfactant molecules.

Chapter 1. Structure of Hydrated Crystal (L_c), Tilted Gel ($L_{\beta'}$), and Liquid Crystal (L_a) Phases of Linear Alkylbenzene Sulfonate (LAS) Studied by X-ray Diffraction and Molecular Dynamics Simulation

1.1. Introduction

Surfactants dissolved in aqueous solution show various kinds of self-assembled structures such as micelles, hexagons, lamellas, and reverse micelles, depending on the molecular structure, concentration, and thermodynamic conditions.⁵⁹ In the aqueous solution, surfactants such as sodium dodecyl sulfate (SDS) and sodium linear alkylbenzene sulfonate (LAS) form lamellar structures at high concentrations and micelles at low concentrations. Precipitation of the hydrated crystal (L_c) phase gives rise to turbidity of the aqueous solution and decrease in fluidity. Thus, from a viewpoint of long term storage of solution products such as liquid detergents and cosmetics, prevention of the precipitation as the hydrated crystal in ambient condition is highly required.⁶

As stated in General Introduction, in spite of the importance as most commonly used liquid detergents and other applications, the structural detail of the L_c phase of LAS has not been determined. However, it still not be cleared.

Molecular dynamics (MD) simulation was employed in the Chapter 1 since we are also interested in the local molecular structures and dynamics of the system after the thermally induced phase transition such as the gel (L_β) or liquid crystal (L_α) phase as described later.

There are two major issues to be overcome to conduct MD simulation of hydrated surfactants in the L_c phase. First, an accurate hydration number of the crystalline surfactant should be obtained. In the L_c phase, a fixed number of water molecules are included in a unit lattice of the hydrated crystal of the surfactant.⁹ Unfortunately, the hydration number of the crystal has not been determined for LAS or many other surfactants. Further, the hydration number may change when a phase transition to the L_β or the L_α takes place.²⁸ Then, the excluded water may come into the hydrophilic inter-bilayer regions. Therefore, a possible change in the hydration number caused by the phase transition should be taken into account in the MD simulation. The second is the initial configuration. Typically, it takes several hours or days to crystallize the hydrated surfactants even experimentally owing to their low structural symmetry. Thus, spontaneous formation of surfactant self-assembly in the L_c phase cannot be expected in the simulation time. Therefore, we must assume the initial configuration to start the MD simulation including the number of water molecules involved in the crystal. In Chapter 1, we solved these two problems with the aid of XRD pattern as reference data in a similar way to other studies on inorganic materials²⁹ and cellulose crystals.³⁰ A series of MD simulations starting from possible LAS crystalline structures have been carried out with five different hydration levels (anhydrate hemi-, mono-, di-, and tetrahydrates) under ambient condition.

This chapter is outlined as follows: In Section 1.2., we describe details of sample preparation for LAS, XRD experimental procedure, and conditions of the XRD analysis. We also give modeling of initial crystal configuration and the details of MD simulations. In Section 1.3., we characterize the crystal structure of each hydration number, and verified whether the simulated diffraction patterns agree with the experimental ones or not. Detailed analysis of the diffraction peaks and the cross-sectional structure of the alkyl group are also given for the simulated monohydrate system, which most closely reproduced the experimental diffraction pattern. We discuss the structural change caused by the phase transition to the $L_{\beta'}$ and L_{α} phases based on experimental and simulated diffraction patterns at 360 and 400 K. Finally, we conclude this chapter in Section 1.4.

1.2. Experiment and Simulation Details

Sample Preparation and XRD Experiment.

The hydrophobic moiety of industrially synthesized LAS is typically a dodecyl group. There are six isomers depending on the position of the hydrophilic moiety bound to a carbon in the dodecyl group. In Chapter 1 and 2 focuses on sodium *n*-dodecylbenzene sulfonate, as shown in Figure 1.1, which has no branched alkyl chain and is the most easily crystallized among the isomers. The LAS was synthesized by the method reported by Gray et al.⁶⁰ Recrystallization was performed to remove unreacted substances and excess inorganic salts. The purity was 99.8 % by LC-MS analysis. After drying LAS in a vacuum oven, ion exchange water was added to prepare LAS 80 wt% aqueous slurry. In the DSC

measurement, an endothermic peak was observed in the vicinity of 350 K as reported to be a main transition temperature by Ma et al.⁶¹ After annealing at 353 K for 10 days or more, the slurry temperature was set back to 298 K. SAXSess MC2 (manufactured by Anton Paar, irradiation X-ray source Cu-K α ray, $\lambda = 1.5418 \text{ \AA}$) was employed for the XRD experiments. After the XRD measurement at 298 K, the temperature was raised to 358 K. And the XRD measurement was performed again after 3 hours. The sample was sealed in a closed cell and placed into vacuum X-ray transmission path to conduct the measurement.

Molecular Dynamics Simulation.

Figure 1.2 shows a schematic diagram of the procedure for preparing the hydrated crystal structure of LAS in MD simulations under a three dimensional periodic boundary condition. Assuming anhydrate, hemi, mono, di, and tetrahydrate of LAS, five different initial configurations were prepared by the following procedure: First, molecular structure of LAS with one sodium ion and one water molecule which were located near the hydrophilic moiety was energy-minimized by the steepest descent method.⁶² The LAS molecule was rotated such that the bond vector from “C1” to “S” (see Figure 1.1) was oriented to the bilayer normal (the z -axis). Atom coordinates of the LAS molecule with one sodium ion and one water molecule were copied in the lateral (the x - y plane) direction to form a monolayer composed of 10×10 LAS molecules in a rectangular shape, so as to satisfy the lateral repeat-spacing of alkyl groups as suggested by the measured diffraction pattern described later in Section 1.3. In the same manner, the other monolayer consisting of the same number of LAS molecules was prepared. Then, the initial configuration was

constructed by facing the each monolayer as the upper and lower leaflets of bilayer. Projection planes of the upper and lower alkyl groups were overlapped in the orthogonal direction to the molecular axis. The monohydrate system consisted of 200 LAS, 40 Na⁺, and 40 water molecules was prepared in a rectangular simulation box with the dimension of 38, 42, and 40 Å along the x , y and z axes, respectively. Excess water molecules were removed from the constructed bilayer for anhydrate, and hemihydrate system. To construct dihydrate and tetrahydrate systems, 200 and 600 water molecules were added in the hydrophilic region, respectively. After the energy minimization of these initial configurations, the following series of MD simulations were performed under constant temperature T and pressure P conditions to relax the system. In these MD simulations, with an assumption that the alkyl group of LAS in the hydrated crystal forms all-trans conformation, all dihedral angles in the alkyl chain were constrained to be 180 degree by applying a harmonic constraint with a force constant $K = 100 \text{ kJ/mol/nm}^2$.

First, 100 ps long MD simulation was performed with $T = 3 \text{ K}$ and $P = 10^5 \text{ MPa}$. Subsequently, sequential 16 sets of 100 ps long MD simulations were performed in which given P values were decreased in stepwise fashion from 10^5 MPa to 1×10^4 , 5×10^3 , 2×10^3 , 1×10^3 , and 0.1 MPa . Next, with $P = 0.1 \text{ MPa}$, sequential 60 sets of 100 ps long MD simulations were carried out in which given T values were increased in a stepwise fashion from 5 K to 300 K with 5 K increments. When a large deformation occurred in these relaxation processes, simulations were suspended. Then, a partial region containing four adjacent LAS molecules ($a \times b \times c = 1 \times 2 \times 2$) where the molecules still keep relatively high structural order with the neighboring sodium ions and water molecules were picked up

from the total system. Using this partial system, we reconstructed the total system composed of 200 LAS molecules such that the size of the simulation cell does not change. The MD simulation, then, restarted from this reconstructed structure. This structural relaxation process was repeated until no structural change occurred at $P = 0.1$ MPa and $T = 300$ K.

MD simulations were further performed in which the constraints on the dihedral angles in alkyl groups were gradually removed over 500 ns. Then, MD simulations without any dihedral constraints at ambient condition were performed for 500 ns. Further, to investigate structural changes caused by thermally induced phase transition, additional 500 ns long MD simulations at $P = 0.1$ MPa and 360 K, followed by 500 ns long MD simulations at $P = 0.1$ MPa and 400 K were performed for each system.

Details of MD simulations are as follows: The temperature was controlled by the velocity scaling method during a process of initial structural relaxation, while the Nosé-Hoover thermostat⁶³ was used after the final stage of the modeling cycle. The Parrinello-Rahman barostat⁶⁴ was chosen to control the pressure tensor, which allows the simulation unit cell to deform into any parallelepiped shapes. The fully flexible cell is desired to simulate a structural change from the L_c to other phases. For the numerical integration of the Newton's equations of motion, the leap-frog method was adopted with a time step of 2 fs. The distance of covalent bonds involving hydrogen atoms were constrained by the LINCS algorithm.⁶⁵ The rigid TIP3P model⁶⁶ was adopted for water, while the CHARMM force field⁶⁷ with the partial charges proposed by He et al.⁶⁸ was adopted for LAS. The Lennard-Jones interaction was smoothly truncated by applying a switching function from

10 to 12 Å. The particle mesh Ewald (PME) method ⁶⁹ was used to calculate the electrostatic interaction. In all MD simulations, the program package GROMACS-5.1.3 ⁷⁰ was used. To calculate the diffraction pattern from MD trajectories, the program package Mercury-3.10.2 ⁷¹ was used. The procedure for obtaining the diffraction pattern is described in the textbook of Giacovazzo et al. ⁷² In the diffraction pattern calculation, the parallelepiped simulation cell was regarded as a triclinic Bravais lattice. Besides, we assumed that the space group was specified to “P1”, since the unit cell and space group necessary to obtain the diffraction pattern could not be determined from the experiment with LAS samples in the L_c phase.

1.3. Results and Discussion

XRD Experiment

In this section, we examine the two X-ray diffraction patterns of LAS 80 wt% aqueous slurry measured at different temperature conditions: $T = 298$ K at which LAS is in the L_c phase, and 358 K at which it is reported in the L_a phase.

Figure 1.3 shows the measured diffraction patterns in each temperature condition, which demonstrate the structural change by the phase transition. In both temperature condition, equally-spaced multiple diffraction peaks derived from the periodic lamellar structure were observed in the small angle region. The position of primary diffraction peak is $2\theta = 2.37^\circ$; $d = 37.3$ Å at 298 K where 2θ and d are the diffraction angle of X-ray and periodic spacing, respectively. It is slightly smaller at 358 K, $2\theta = 2.22^\circ$; $d = 39.8$ Å. This

shift indicates that an interval of the lamellar of the hydrated crystal increased with increasing temperature.

Another diffraction peaks were confirmed in the vicinity of $2\theta = 20^\circ$ ($2\theta = 17.8, 18.7, 20.0, 21.2, 22.7,$ and 23.4° ; $d = 5.0, 4.7, 4.4, 4.2, 3.9,$ and 3.8 \AA) mainly derived from distance of the most adjacent alkyl groups. At 298 K, the positions of the observed diffraction peaks are close to the reported values with assuming the arrangement of alkyl groups in the x - y plane is in the rectangular lattice structure ($2\theta = 21.2$ and 23.4° ; $d = 4.2$ and 3.8 \AA).⁷³ The other peak was also observed at $2\theta = 17.8^\circ$; $d = 5.0 \text{ \AA}$, which is not reported in the diffraction patterns for other surfactant systems. This peak might be originated from a periodic arrangement of counter ions, waters, or benzene rings within the LAS hydrated crystal, since this interval is too large to be regarded as the periodic interval of the nearest alkyl groups.

At 358 K, some of diffraction peaks $2\theta = 17.8$ and 23.4° corresponding to $d = 5.0$ and 3.8 \AA , disappeared. In contrast, a few sharp diffraction peaks still remained such as $2\theta = 21.2^\circ$; $d = 4.2 \text{ \AA}$ even at 358 K. They are qualitatively different from the generally-known broaden diffraction peaks derived from the L_α phase. Namely, the actual lamellar structure of LAS observed at 358 K has higher periodicity than that expected in the L_α phase.

On the other hand, according to the phase diagram of hydrated LAS suggested by Ma et al., the solution with a composition of LAS/water = 80/20 (w/w) should exhibit a lamellar L_α phase at 358 K. The inconsistency of our observation with that by Ma et al. may be due to their use of the polarized microscopy alone to confirm the phase.

Note that the number of water molecules located in an inter-lamellar hydrophilic region of the hydrated crystals is determined stoichiometrically under given conditions of T and P .⁹ The hydration level in the well-equilibrated hydrated crystal is uniquely determined. Although there is a possibility that experimental samples prepared here might contain hydrated crystals with different hydration numbers, it should be minor. Therefore, we assumed that the experimental XRD patterns come mainly from hydrated crystals with unique hydration numbers.

The more detailed structure of the LAS hydrated crystals at different temperatures will be discussed in the next section on the basis of our MD simulations.

Comparison of the Experimental and Simulated XRD Patterns

A comparison of the experimental diffraction patterns and those calculated from MD trajectories of LAS hydrated crystals with different hydration numbers are made. Figure 1.4 plots the diffraction patterns calculated from the MD trajectory of the LAS anhydrate, hemi-, mono-, di-, tetrahydrate crystals at 298 K. The calculated diffraction pattern based on the MD trajectory for the LAS monohydrate crystal almost reproduced the experimental diffraction patterns at 298 K: $2\theta = 7.29^\circ$ (corresponding to the third peak from the lamellar repeat spacing), 17.8, 18.6 ($\doteq 18.7$), 20.2 ($\doteq 20.0$), 21.1 ($\doteq 21.2$), 22.7, and 23.5° ($\doteq 23.4^\circ$) ($d = 36.3, 5.0, 4.7, 4.4, 4.2, 3.9, \text{ and } 3.8 \text{ \AA}$). The consistency of monohydrate crystal is clear when we compare the diffraction patterns obtained from other hydration level. Therefore, we conclude that the lamellar structure observed in the XRD experiment at ambient temperature is consistent with the monohydrate LAS hydrated crystal structure

simulated by MD. We note that there are still minor differences between them such as excess / deficiency peaks, small shifts of peak positions, and differences in relative peak intensity. These differences may be attributed to different water distribution in space from that of monohydrate crystals. The structural stability of the monohydrate system may be attributed to achieving filling free spaces and making energetically-favorable interactions, with minimum hydrated water around LAS hydrophilic groups. Figure 1.5(a) shows radial distribution function between sulfur atom of LAS and oxygen atom of water $g_{S-O}(r)$ under the same temperature and pressure condition with different hydration numbers. The first peak of the $g_{S-O}(r)$ in the monohydrate system (yellow) is sharpest among the systems. It indicates that greater amount of water molecules are arranged around the sulfate atoms of LAS with energetically favorable interactions. Figure 1.5(b) shows mass density of the calculated systems. The monohydrate system exhibit the highest density among the five systems, which indicates that the monohydrate system has less free volumes than the other systems under the same temperature and pressure condition, partially attributed to the energetically-favorable water-sulfate group interaction shown in Figure 1.5(a).

Figure 1.6(a) shows an example of the arrangement of the alkyl groups in the sectional plane extracted from the MD trajectory for the monohydrate crystal at 300 K. The initial arrangement of the alkyl groups before the structure relaxation cycle by a series of MD simulations was a rectangular lattice with a dimension of 4.2 Å in the direction along C-C bond and 3.8 Å in the orthogonal direction, whereas the arrangement after the structure relaxation cycle is a rectangular lattice with a dimension of 4.6 Å along C-C bond and 4.0 Å in the orthogonal.

In addition to these dimensional changes of a lattice, the adjacent alkyl groups along the orthogonal direction of C-C bond were shifted of C-C bond with a half distance of adjacent alkyl groups along C-C bond direction from initial arrangement in the structural relaxation process. This shift is accompanied by the change of a lattice shape from a rectangular to a face-centered rectangular lattice. As a result, a separation distance of the most adjacent alkyl groups is about 3.9 Å, which is the origin of the diffraction peak at $2\theta = 22.7^\circ$ in Figure 1.3. There remain, however, some XRD peaks (at $2\theta = 19.3, 19.7$ and 22.2° ; $d = 4.6, 4.5$ and 4.0 Å) which cannot be assigned only by the d -spacing values of the face-centered rectangular lattice. Figure 1.6(a) also shows that alkyl groups in the upper and lower leaflets of the bilayer did not completely overlap in the direction of the molecular axis after the structural relaxation cycle. The periodicities in positions of alkyl groups between upper and lower monolayers might contribute to diffraction peaks observed in the XRD experiment.

Figure 1.6(b) shows the projection planes of the upper and lower alkyl groups aligned to overlap each other. We can confirm the periodic spacing corresponding to 4.7, 4.4 and 3.8 Å of the monoclinic lattice structure. Another periodic spacing can be confirmed with Figure 1.6(c). After the structural relaxation cycle, the hydrophilic group consisting of benzene ring and sulfonate group were bent by about 40° with respect to the tilted alkyl groups. The LAS hydrophilic groups are salt-bridged between the facing lamellas via sodium ions. In this configuration, the spacing between adjacent hydrophilic groups is about 5.0 Å, and the lamellar repeat spacing is 36.3 ± 0.1 Å ($\doteq 37.3$ Å).

Thus, we succeeded in assigning the d -spacing corresponding to the pronounced diffraction peaks of $2\theta = 7.29, 17.8, 18.6, 20.2, 21.1, 22.7,$ and 23.5° , which strongly supports our evaluation that the diffraction pattern calculated from MD trajectory for monohydrate crystal at 298 K well reproduces the experimental XRD on the LAS sample in the L_c phase.

It should be noticed that structural change from the rectangular to the face-centered rectangular lattice occurred spontaneously in the process of structural relaxation. It implies that MD simulations have a possibility to predict molecular structure of unknown hydrated crystals of surfactants by adopting proper initial configurations based on the repeat-spacing information provided by the XRD experiment.

In summary, the L_c structures with different hydration levels were obtained by repeating the rearrangement and the structural relaxation from the artificial configurations based on the limited number of d -spacing values, and the L_c structure of the monohydrate system best reproduced the diffraction pattern. It is experimentally confirmed that SDS can form dihydrate,⁷ monohydrate,¹² hemihydrate,¹³ and anhydrate¹⁵ L_c phases. Thus, we consider that LAS could also form the L_c phases with hydration numbers other than the monohydrate. If we prepare and examine much more samples with different water/LAS composition, it is possible to find other hydration crystals of LAS with different hydration numbers. Crystal structures other than the monohydrate system that did not match the experimental XRD pattern.

Crystal Structures of Other than the Monohydrate System

The crystal structure of LAS under the ambient conditions was found to be the monohydrate. However, recent studies on SDS reported that different crystalline polymorphs can be produced by performing temperature drop experiments at various temperature conditions.⁷⁴ Therefore, the structures of the other hydrates might be observed depending on the conditions. In this Section, we describe the crystal structures other than the monohydrate system did not match the present experimental XRD pattern. Table 1.1 shows the area per molecule S in the x - y plane, the tilt angle of the alkyl group φ , and the lamellar repeat spacing d_L for each hydrated crystal structure. Here, φ is defined as the angle between a vector connecting C1 to C18 carbon atoms (noted in Figure 1.1) and the z -axis, and averaged over simulation time and LAS molecules. As increasing the hydration number, S and φ both increased. d_L for anhydrate and tetrahydrate systems are larger than those observed in the other systems. The mechanisms of these differences are understood by captured images and number density profiles of each atom along the z -axis as summarized in Figure 1.7. In the case of anhydrous crystals, the sodium ions are mainly located at the space between lamellae along the bilayer normal (Figure 1.7(a) and (b)), whereas in higher hydrated system, sodium ions are also more frequently found in the vicinity of sulfonate group along the lamella plane (Figure 1.7(e)–(j)). Most water molecules exist near the benzene ring in hemihydrate and monohydrate systems (Figure 1.7(c)–(f)), while stoichiometrically-excess water in dihydrate and tetrahydrate systems, were located between lamellae with forming a thin aqueous layers (Figure 1.7(g)–(j)). The oxygen atoms of water located near the benzene ring uniformly coordinates to sodium ions (Figure 1.7(a), (c), (e), (g), and (i)). Based on these observations, we judged that the

increase in S originates from the local configuration in which sodium ions or hydration waters are located near the hydrophilic group. An increase in φ is caused in order to fill the additional free volume generated by the increase in S . We consider that the water molecules near the benzene ring contribute to stabilize the crystal structure by (1) filling free spaces around the benzene rings with realizing closer atom packing in the crystal, and (2) making energetically-favorable interactions of the polar functional group of LAS (charge-dipolar interaction) with sodium ions, as suggestion by Laughlin.⁹ The trend of increases in S and φ , accompanied by decrease in d_L , with hydration number of the crystals is consistent with the trend observed in the anhydrides and monohydrates of SDS crystals reported by Smith et al.¹⁵ Therefore, the trend is a common between LAS and SDS, and might be observed for other ionic surfactants systems. Figure 1.8 provides another beneficial information about local configuration in the LAS hydrated crystals. The benzene rings are randomly oriented in the monohydrate system, while those have higher periodic structure in the dihydrate and tetrahydrate systems. In the dihydrate system, benzene rings exhibited the “Herringbone Pattern” with two adjacent molecules of LAS as an asymmetric unit. In tetrahydrate system, they formed another kind of periodic structure with five molecules of LAS as an asymmetric unit. The observed many diffraction peaks in the XRD pattern (see Figure 1.4), which do not originate from the lamellar interval and the packing period of the alkyl chain in dihydrate and tetrahydrate crystals, may be assigned to these lateral long period structures of benzene rings. As described above, the experimental XRD pattern shows the best match to the XRD pattern calculated from MD trajectory in the

monohydrate system. It implies that the in-plane orientation of the benzene ring is relatively disordered in the LAS sample at 298 K.

Structural Change Caused by Thermally Induced Phase Transition of LAS

According to the experimental XRD pattern shown in Figure 1.3, LAS 80 wt % aqueous slurry does not exhibit L_α phase at 358 K. In this section, we explore the possible structural change caused by temperature by comparing the diffraction patterns calculated from MD trajectories for each hydration level at 360 K with the experimental diffraction pattern at 358 K. For further comparison, the diffraction patterns calculated from MD trajectory of the tetrahydrate system at 400 K (in the L_α phase) was examined. This is because the tetrahydrate system contains the same amount of water as designed in the experiment (LAS/water = 80/20 (w/w)), with considering the fact that all excess water separated from the hydrated crystal come into the inter-lamellar hydrophilic region in the L_α phase.

Figure 1.9 shows the diffraction patterns calculated from the MD trajectories for the monohydrate system at 360 K and the tetrahydrate system at 400 K and the experimental diffraction patterns measured at 358 K. Since the influx of water between the lamellas was assumed during the phase transition to the L_β phase,²⁸ there was concern that the diffraction pattern could not be reproduced by the monohydrate system. Unexpectedly, the major diffraction peak positions ($2\theta = 6.72, 18.3, 19.1, 20.0, 21.0, \text{ and } 21.9^\circ$) including the small-angle peak are identical between simulated ($T = 360$ K) and experimental ($T = 358$ K) results, though a minor difference could be detected.

Therefore, we decided that the structure of the monohydrate obtained by the MD simulation at 360 K is the closest to the experimental structure. Table 1 shows the area per molecule S in the x - y plane, the tilt angle of the alkyl group φ and the lamellar repeat spacing d_L for monohydrate system at 300 and 360 K and for tetrahydrate system at 400 K. Here, φ is defined as the angle between a vector connecting C4 to C16 carbon atoms (noted in Figure 1.1) and the bilayer normal. With increasing temperature, the tilt angle φ changed from $48 \pm 2^\circ$ at 300 K to $37 \pm 4^\circ$ at 360 K. In contrast, the lateral position of centers of mass of LAS molecules did not change so much during 500 ns long MD simulations at 360 K. Besides, as shown in Figure 1.10(a), the conformation of the alkyl group remained nearly all-trans at 360 K. Thus, the tilt angle change directly leads to an increase of d_L (from 36.3 ± 0.1 to 38.9 ± 0.1 Å).

Figure 1.11 shows distributions of azimuth angle of a vector connecting C9 and C10 atoms of LAS against the bilayer normal in three lamellar systems. In the L_c phase at 300 K, almost all C-C bonds in the cross-section were aligned in the same direction which causes the narrow distribution as shown in Figure 1.11(a). In contrast, the bonds were randomly orientated at 360 K as shown in Figure 1.10(b). It results in wider distribution of azimuth angle in Figure 1.11(b) than in Figure 1.11(a). The observed structure at 360 K can be assigned to the $L_{\beta'}$ phase, because LAS molecules show rotational motion around the long axis of the tilted alkyl chain. With a transition to the $L_{\beta'}$ phase, arrangement of the alkyl chain in the cross-sectional lattice changed from the face-centered rectangular to the hexagonal, and the Na^+ exchange at the inter-lamellar layer and a decreasing the periodicity of the hydrophilic group were observed. These changes are presumed to be the factors

causing the disappearance of the XRD peaks observed only in the L_c phase ($d = 5.0$ and 3.8 Å) shown in Figure 1.3. These results suggest that the phase transition found around 350 K in the phase diagram of Ma et al.⁶¹ is a transition from L_c to $L_{\beta'}$ phase.

On the other hand, as shown in Figure 1.9, the diffraction pattern from MD trajectory for the tetrahydrate system at 400 K demonstrates no evident sharp peaks corresponding to highly periodic structure found in the L_c or $L_{\beta'}$ phase, while it remains showing diffraction peak in the small angle region, which is derived from the d_L , and a broad diffraction peak in the wide angle region. Although we could not have undertaken the corresponding experiment for the difficulty of the experimental setup in this study, the origin of diffraction peaks changes at 400 K can be speculated according to the previous study by Mathevet et al.⁷⁵ They obtained the diffraction pattern derived from the L_α phase at 463 K, though the system, which consisted of LAS anhydride with a guanidinium cation, was slightly different from the present chapter. The authors described that the diffraction pattern contains sharp diffraction peaks related to lamellar repeat spacing in small-angle region, and a diffusive peak originated to liquid-like conformation of the alkyl chains in the wide-angle. In addition, as shown in Figure 1.10(c), (d) several water molecules penetrated into the hydrophobic region, which was encouraged with disordered alkyl groups. The liquid-like state of the alkyl chains in the L_α phase was also confirmed by broad distributions of azimuth of C-C bond vector shown in Figure 1.11(c) as well as almost structureless radial distribution function between C9 atoms shown in Figure 1.12. Consequently, we concluded that the lamellar structure obtained in the tetrahydrate system at 400 K was in the L_α phase.

The d_L estimated by the MD simulation at 400 K was $37.5 \pm 0.1 \text{ \AA}$, which is smaller than that observed in the $L_{\beta'}$ phase by MD simulation at 360 K, despite a possible influx of water into the hydrophilic regions between lamellar, or the increase of the d_L caused by the thermal expansion. The origin of the getting thin of the d_L could be understood by assuming that molecular orientation of LAS in L_{α} phase is disordered with their random conformation, due to the increase of the occupied area by the existence of the permeated water molecules.

Though it is very difficult to observe reverse phase change from disordered structure to ordered one in the cooling process from 400 K to 300 K (data not shown), this is a general problem of MD simulation caused by limited-sampling of atomic configurations within a finite simulation time. On the other hand, macroscopic properties of each lamellar system, such as membrane area, its thickness, and tilt angle of LAS, converged well in 500 ns long MD simulations. So, we decided that each system reached an equilibrium state under given conditions, and made discussions on molecular configuration for each phase.

As a conclusion, we succeeded in relating changes in molecular configuration of LAS molecule in the hydrated crystals in the thermally induced phase transition process to the structural change in lamellar (L_c , $L_{\beta'}$ and L_{α}) observed in the experimental diffraction patterns.

1.4. Conclusions

In order to determine the molecular configuration of the surfactant hydrated crystals in the L_c phase, and to understand the structural change during thermally induced phase

transition from the L_c to $L_{\beta'}$ and L_α phases, the XRD experiment and MD simulation were carried out for aqueous LAS systems. There were two issues to be overcome to investigate the molecular configuration in the L_c phase. The first issue is unknown hydration number of LAS in the L_c phase and the second is the initial arrangement of molecules. In order to overcome these problems, we adapted crystallographic spacing of LAS obtained by the XRD experiment as the initial guess of molecular configuration for MD simulations. Through the relaxation process for the assumed crystal structure, molecular configurations of the anhydrate, hemi-, mono-, di-, and tetrahydrate structures of LAS hydrated crystals were successfully prepared. We found that molecular configuration obtained in the monohydrate system is most suitable for the LAS hydrated crystal structure at 300 K, since the diffraction pattern calculated from the monohydrate system well coincided with the experimental XRD pattern. Detailed analysis on local molecular configurations in the L_c phase revealed the periodic intervals which contribute to diffraction peaks in the observed diffraction pattern. Further MD simulations were conducted with raising temperature from 300 K to 360 K for each hydrated system, and 400 K for tetrahydrate system, producing the $L_{\beta'}$ and liquid crystal L_α phase of LAS molecule assembly. By comparing experimental and simulated diffraction patterns, we found that the lamellar structure of LAS 80 wt% aqueous slurry at 358 K, which was conventionally considered to be L_α phase, is the lamellar in the $L_{\beta'}$ phase. We have firstly elucidated the relationships between the phase transitions in lamellar of LAS hydrated crystals (L_c , $L_{\beta'}$ and L_α) and local molecular configurations of LAS molecule by combining the XRD structural analysis and all-atom MD simulation. The

strategy we adopted in this chapter will be widely applicable for predicting molecular structure of unknown hydrated crystals of surfactants.

Table 1.1. Area per molecule S , the lamellar repeat spacing d_L and tilt angle of the alkyl group φ of LAS crystal

	S (\AA^2)	d_L (\AA)	φ ($^\circ$)
0 H ₂ O	23.0 ± 0.1	41.5 ± 0.1	33 ± 4
$\frac{1}{2}$ H ₂ O	26.3 ± 0.2	37.2 ± 0.1	43 ± 4
1 H ₂ O	27.2 ± 0.1	36.3 ± 0.1	46 ± 2
2 H ₂ O	27.6 ± 0.1	38.8 ± 0.2	45 ± 3
4 H ₂ O	27.7 ± 0.1	41.5 ± 0.1	48 ± 2

Table 1.2. Area per molecule S , the lamellar repeat spacing d_L and tilt angle of the alkyl group φ of lamellar structure of LAS for each simulation condition

	S (\AA^2)	d_L (\AA)	φ ($^\circ$)
1H ₂ O at 300 K (L_c)	27.2 ± 0.1	36.3 ± 0.1	46 ± 2
1H ₂ O at 360 K ($L_{\beta'}$)	27.2 ± 0.1	38.9 ± 0.1	37 ± 4
4H ₂ O at 400 K (L_α)	37.1 ± 0.9	37.5 ± 0.1	31 ± 17

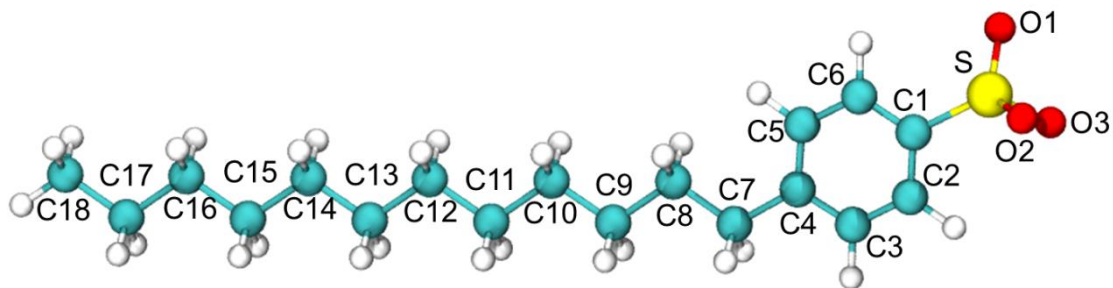


Figure 1.1. A chemical structure of linear alkylbenzene sulfonate (LAS).

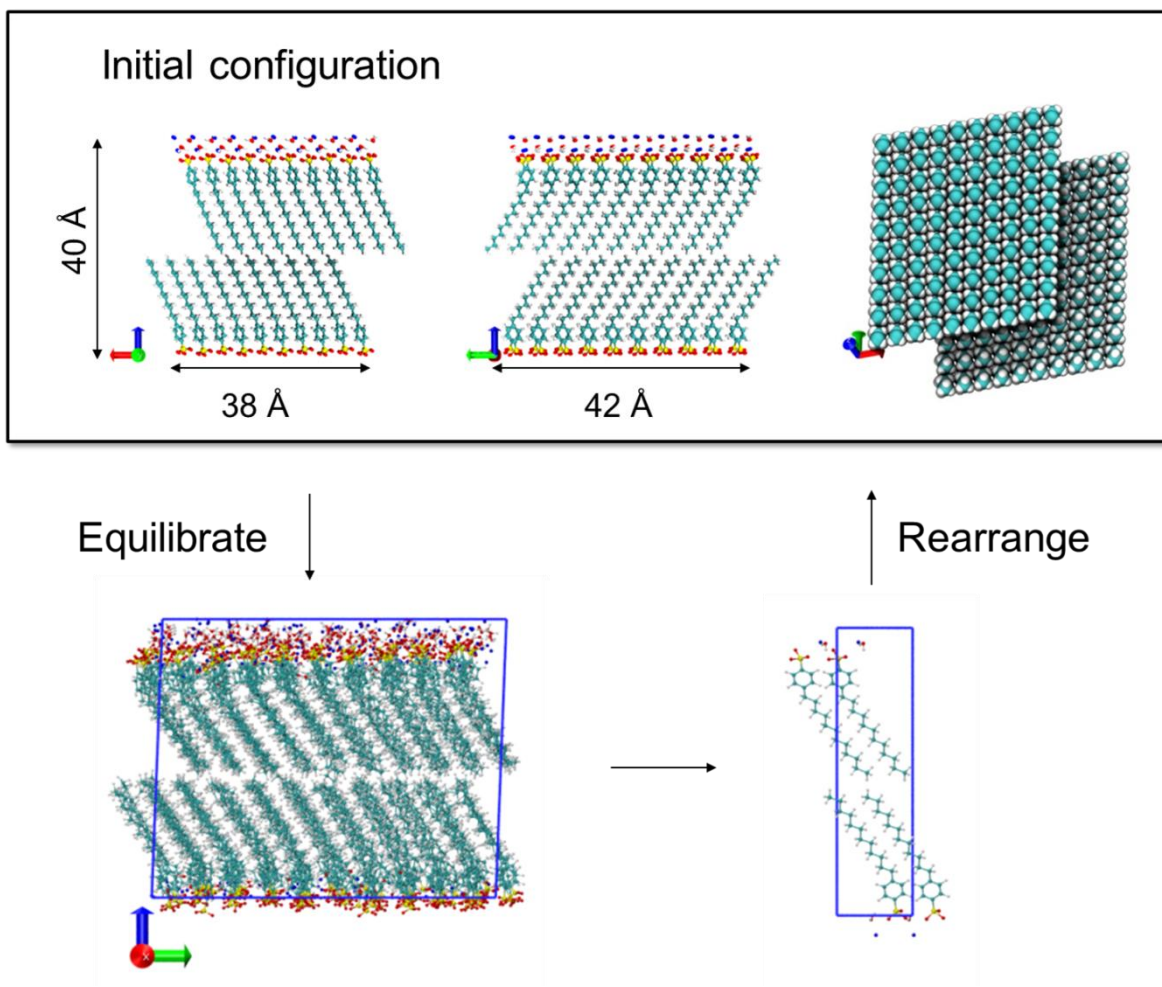


Figure 1.2. Schematic diagram of the cycle of structure relaxation process of initial configuration of hydrated crystal of LAS for a MD simulation.

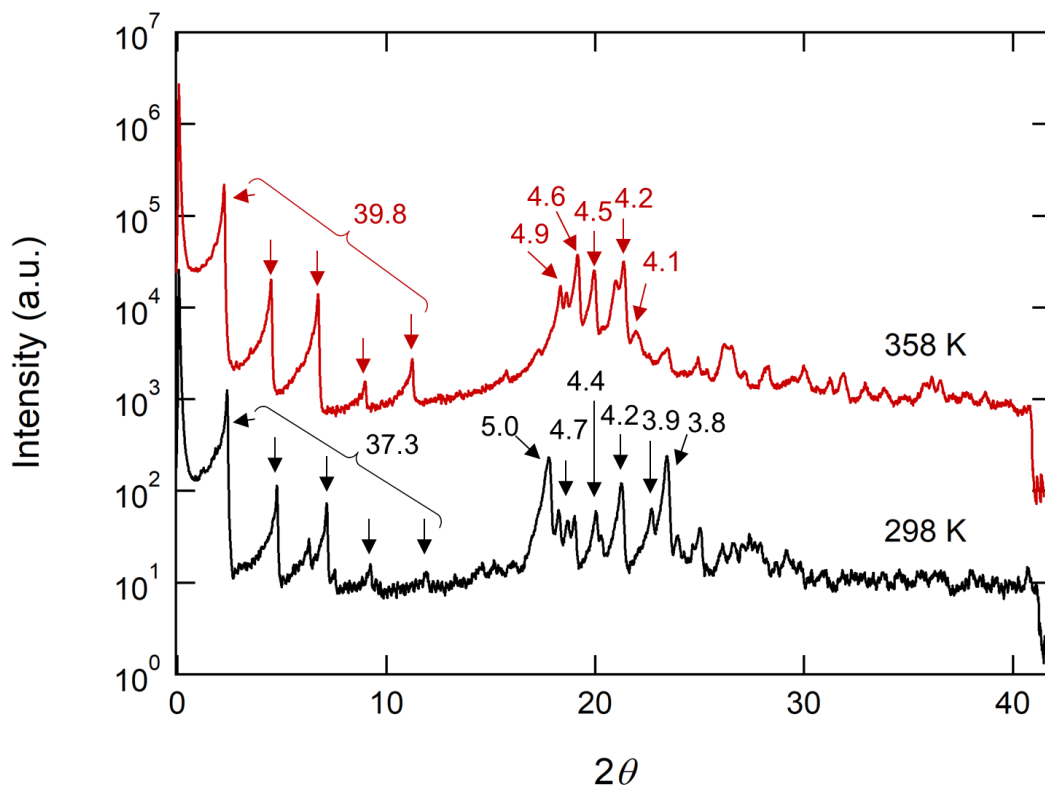


Figure 1.3. The XRD patterns measured with a sample of LAS/water = 80/20 (w/w) at 298 K (black) and 358 K (red). Pronounced peaks assigned to the lamellar repeat spacing and the packing periods of alkyl chain are indicated by arrows and d -spacing values as Å.

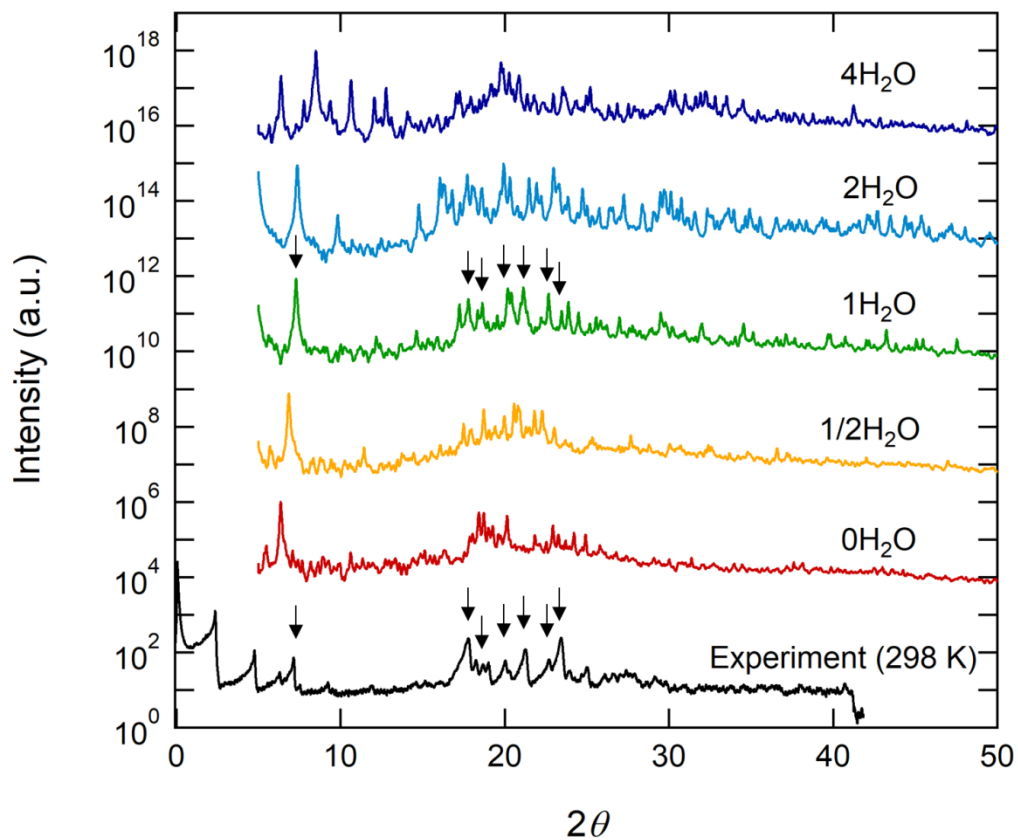


Figure 1.4. The XRD patterns calculated from MD trajectories for anhydrate (red), hemihydrate (yellow), monohydrate (green), dihydrate (cyan), and tetrahydrate (blue) systems at 300 K. The experimental XRD pattern at 298 K (black) is also shown as a reference. Downward black arrows indicate consistent peak positions between the experimental and simulated (monohydrate) diffraction patterns.

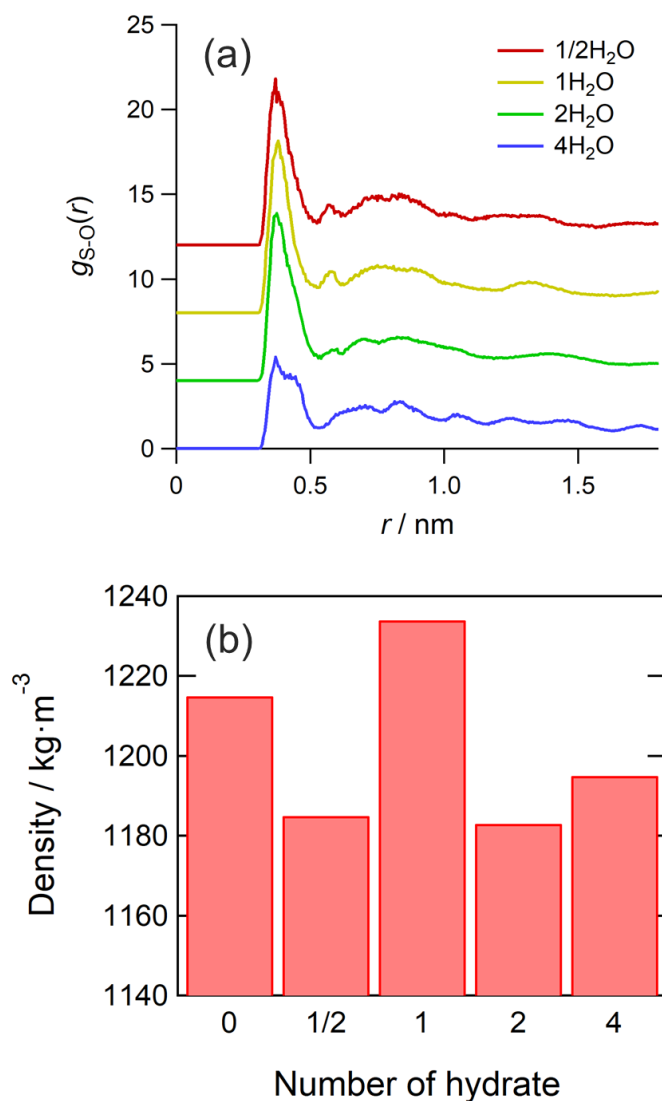


Figure 1.5. (a) Radial distribution function $g(r)$ between sulfur atom of LAS and oxygen atom of water in four systems with different hydration levels. Peak shape of the monohydrate system is relatively sharp with other systems. (b) System density at each hydration level including anhydrate.

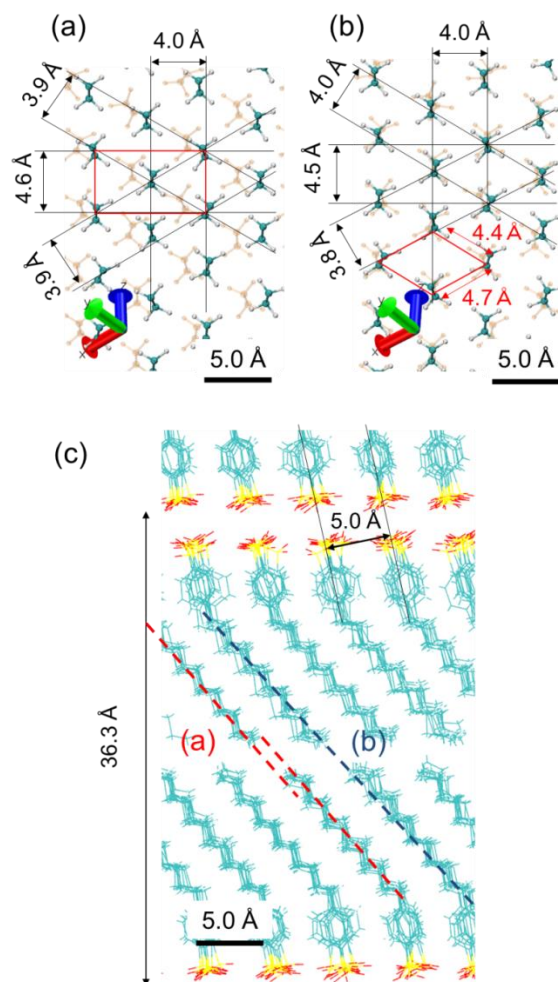


Figure 1.6. MD snapshot images of LAS monohydrate system focused on (a) lateral section of alkyl chain and its packing periods in upper layer (lower layer are indicated in orange color), (b) packing periods between the upper and the lower layer, (c) normal section of lamellar and its interval and the head-group period. Unit cell of lateral direction are indicated by red line in (b). The direction of cross-sectional planes in (a) and (b) were indicated by dashed lines in (c).

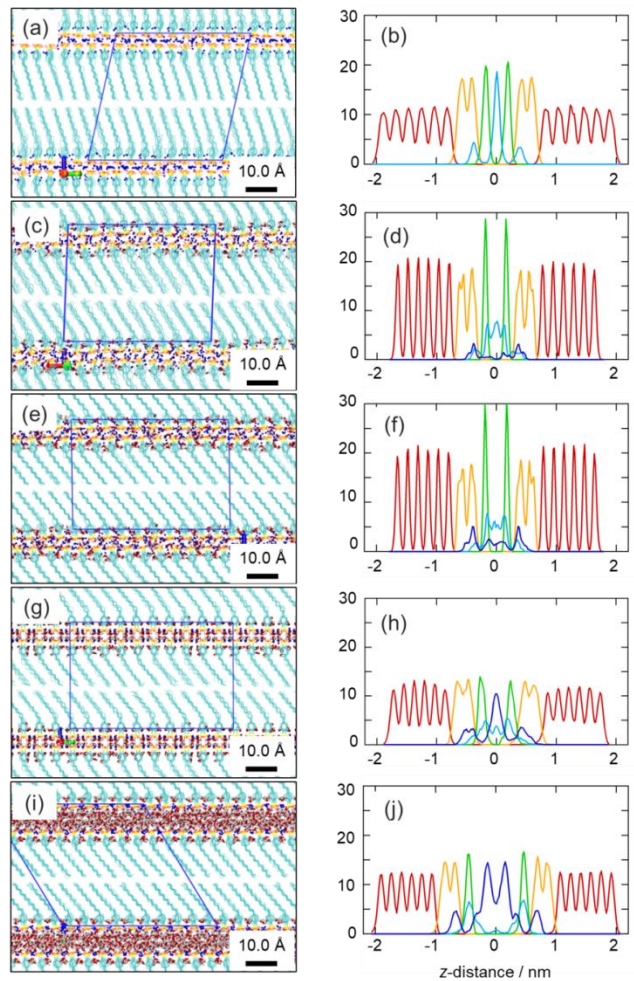


Figure 1.7. Side views of MD simulation unit cell for the (a) anhydrate, (c) hemihydrate, (e) monohydrate, (g) dihydrate, and (i) tetrahydrate systems at 300 K, and number density profiles of atoms for (b) anhydrate, (d) hemihydrate, (f) mono-hydrate, (h) dihydrate, and (j) tetrahydrate systems. Difference in line colors of the number density profiles indicate difference in atom kinds; red: aliphatic carbon, yellow: aromatic carbon, green: sulfur, cyan: sodium, blue: oxygen of water.

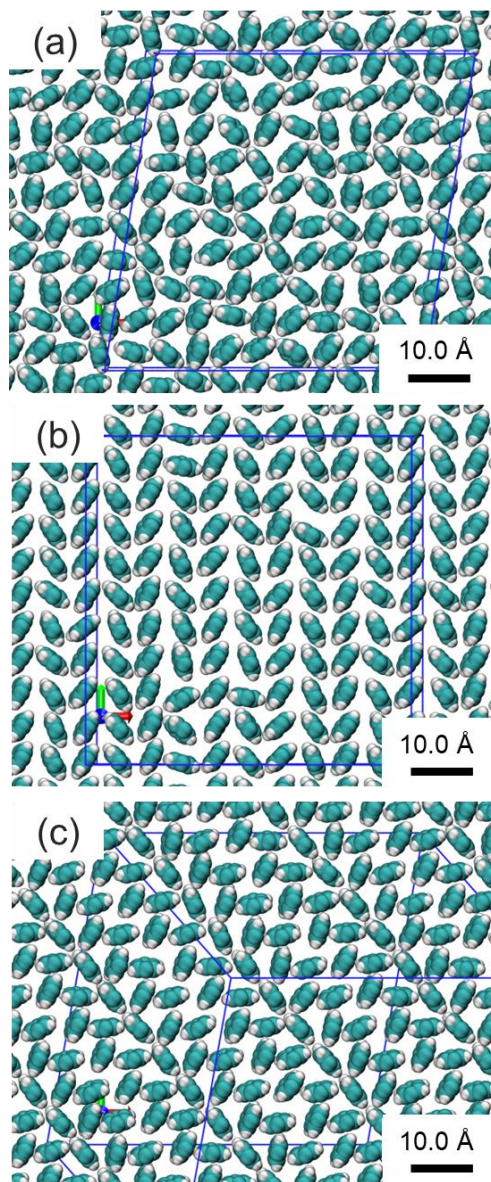


Figure 1.8. Arrangement of the benzene rings of LAS projected on the x-y plane for (a) monohydrate, (b) dihydrate and (c) tetrahydrate systems.

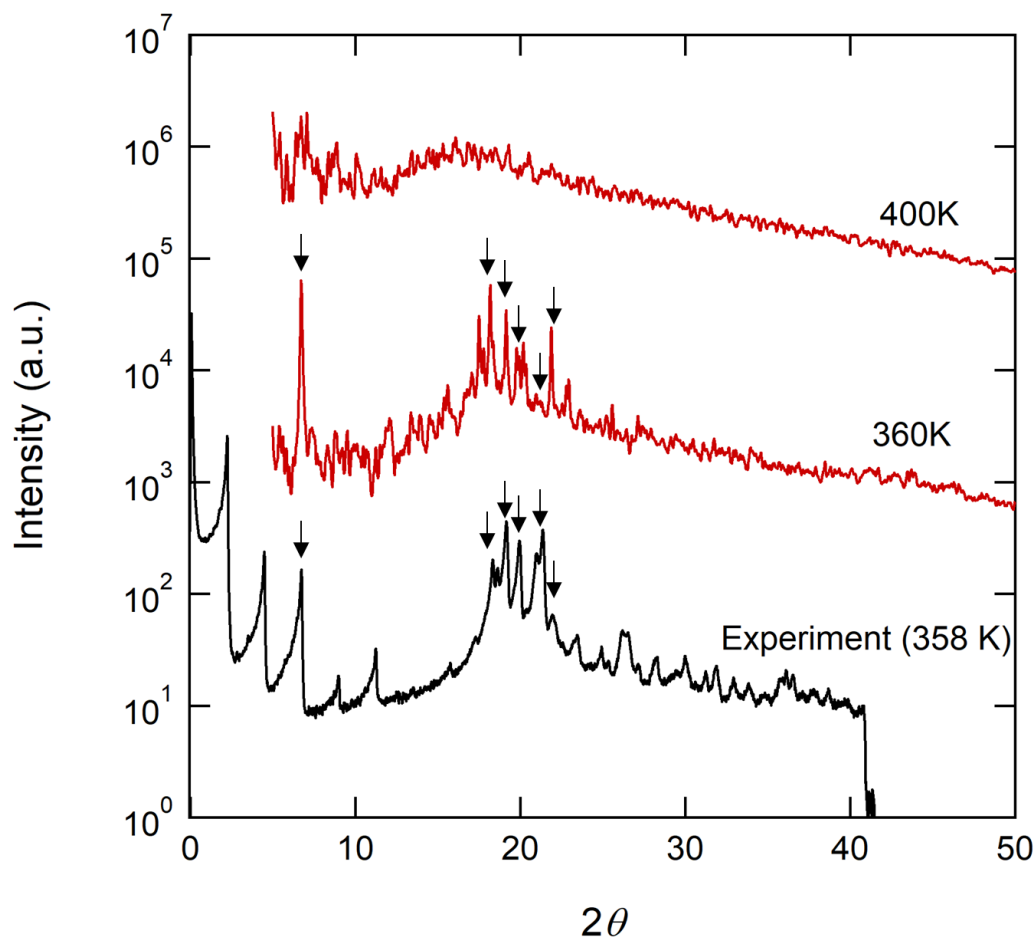


Figure 1.9. The XRD pattern obtained by the XRD experiment on a sample of LAS/water = 80/20 (w/w) at 358 K (black), and the XRD patterns calculated from MD trajectories for the LAS monohydrate system at 360 K and LAS tetrahydrate system at 400 K (red). Downward black arrows indicate peak positions consistent between the experimental and simulated (monohydrate) XRD patterns.

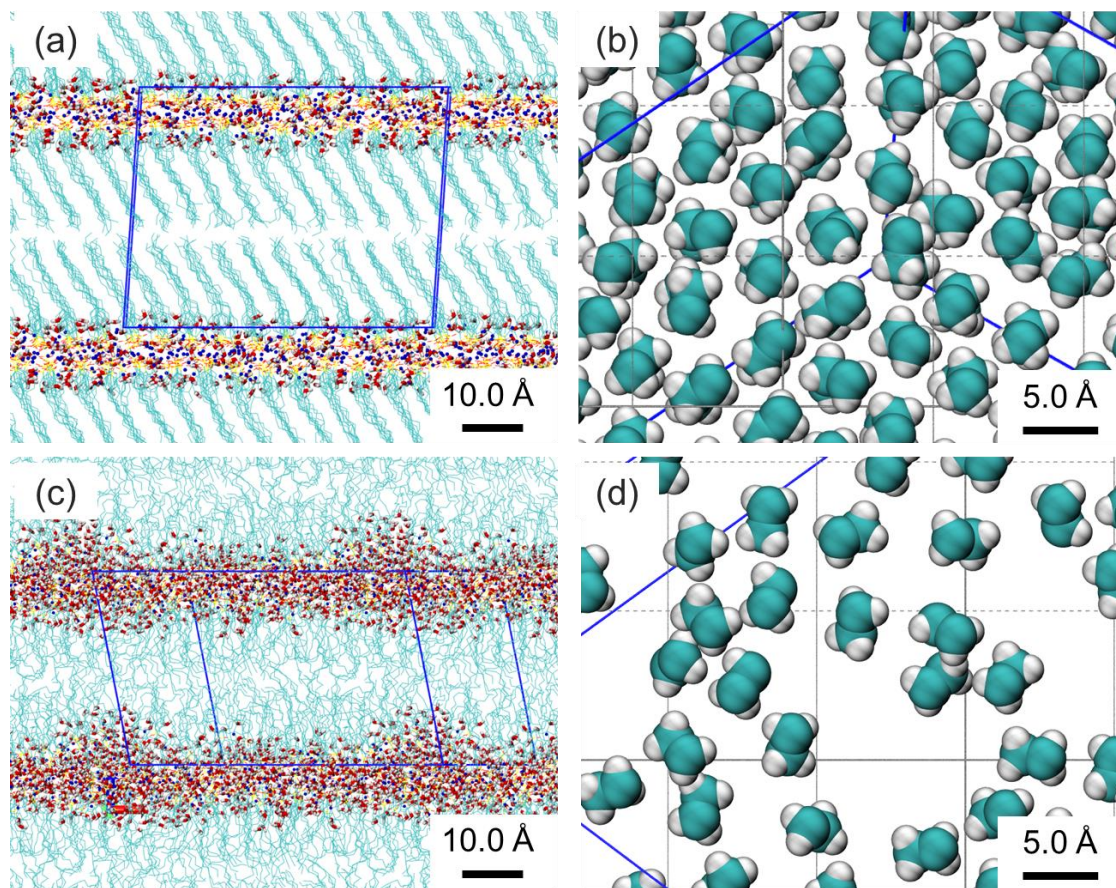


Figure 1.10. Side views of MD simulation unit cell for (a) monohydrate system at 360 K, and (c) tetrahydrate system at 400 K. Panels (b) and (d) draw arrangement of the alkyl groups of C9 and C10 on the x - y plane sectioned at $z = 10 \text{ \AA}$ from. $z = 0$ corresponds to the center of mass of the bilayer.

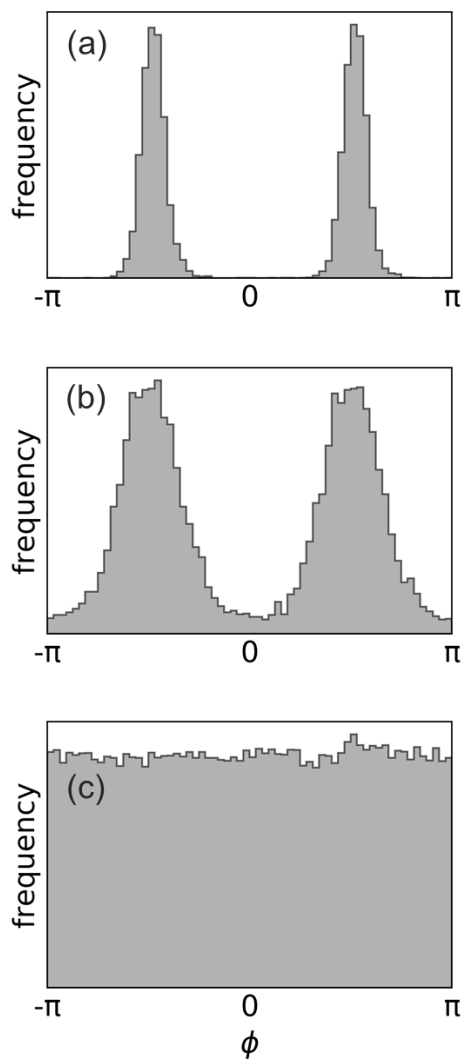


Figure 1.11. Azimuth distribution of bond vector formed by C9 and C10 atoms (a) monohydrate at 300 K (L_c), (b) monohydrate at 360 K ($L_{\beta'}$) and (c) tetrahydrate at 360 K (L_a).

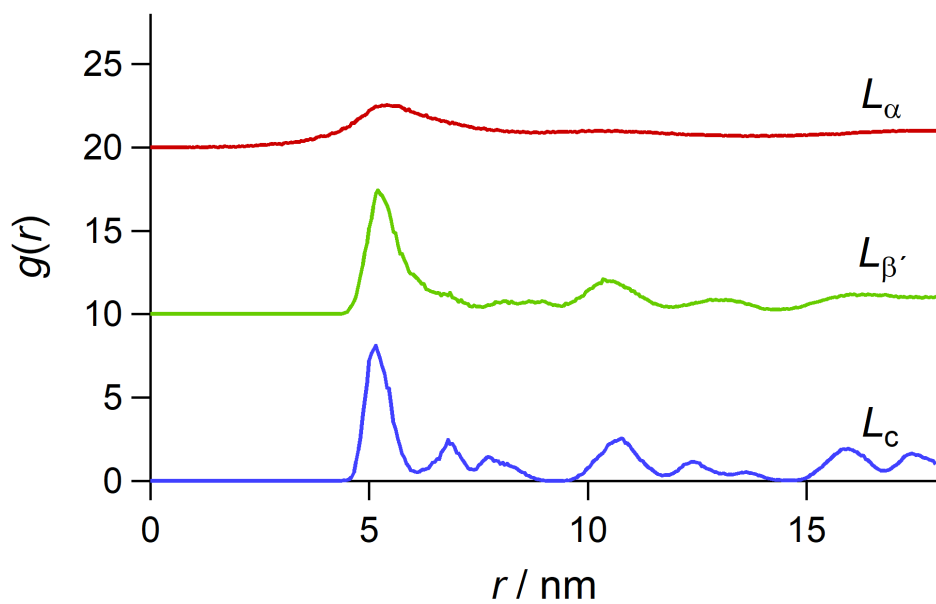


Figure 1.12. Radial distribution function between C9 atoms in the L_c (blue), $L_{\beta'}$ (green) and L_α (red) systems corresponded to Figure 1.11. The results of the $L_{\beta'}$ and L_α were shifted up for make it easy to see.

Chapter 2. Molecular Behavior of Linear Alkylbenzene Sulfonate in Hydrated Crystal, Tilted Gel, and Liquid Crystal Phases Studied by Molecular Dynamics Simulation

2.1. Introduction

As discussed in Chapter 1, lamellar structures show various subphases, depending on temperature, pressure, and hydration.⁷ Generally, these subphases are classified depending on their structure and dynamics. However, the conformation of the surfactants in these lamellar phases is still not fully understood.

Sperline et al. investigated the conformation of sodium dodecyl sulfate (SDS)³⁸⁻⁴⁰ and sodium linear alkylbenzene sulfonate (LAS)^{41,42} in the L_c phase using infrared spectroscopy (FT-IR) and linear dichroism (LD) measurements. SDS in the L_c phase of a monohydrate crystal has a *gauche* conformation at the root of the alkyl chain segment bound to the OSO_3^- , whereas it has an all-*trans* conformation in a crystal with different hydration numbers. SDS³⁹ and LAS⁴¹ in the $L_{\beta'}$ phase have alkyl groups inclined by about 45° with respect to the bilayer normal. It is supposed that the double *gauche* conformation produces a uniform tilt of the alkyl chains, which may allow the surfactant molecules in the $L_{\beta'}$ phase to twist with very low translational diffusivity. A molecular dynamics (MD)

simulation study on dipalmitoyl phosphatidylcholine (DPPC) bilayers by Tu et al. tried to investigate a relationship between chain conformation and reorientation ability in the $L_{\beta'}$ phase.³⁵

It has also been reported that the *gauche* conformation is reduced for SDS and LAS in the L_{α} phase adsorbed on an Al_2O_3 surface, which is attributed to the strong electrostatic interaction between the head groups (OSO_3^- or SO_3^-) of the surfactants and the matrix surface.^{40,42} We can thus expect that a similar reduction of the *gauche* conformation may occur in the bulk L_{α} phase with a lower hydration number through salt-bridging among the head groups of the surfactant via counter ions. However, within our knowledge, this has not been previously reported.

In present chapter, the structure and dynamics of LAS molecules in the L_c , $L_{\beta'}$, and L_{α} phases are investigated using 1 μs long all-atomistic MD simulations. The initial configurations of the molecules in these phases were obtained in chapter 1, which combined X-ray diffraction measurement and MD simulation. The difference in dynamics is investigated for the lateral translational diffusion. Conformational dynamics is also analyzed separately for each segment of the LAS molecule, namely sulfonates, benzene rings, and alkyl chains. The lateral diffusion is found to be rapid in the L_{α} phase, but undetectably slow in the L_c and $L_{\beta'}$ phases. In the L_{α} phase, reorientational relaxation is found to be rapid and uniform, whereas in the L_c and $L_{\beta'}$ phases, the SO_3^- and benzene rings show much slower reorientational relaxation than that for the alkyl chains. A conformational pattern analysis reveals that a high *gauche* fraction defined around the odd-numbered C-C bonds of the alkyl chains, is the main cause of the different conformational

relaxations of LAS in the $L_{\beta'}$ and L_{α} phases. The orientation of the SO_3^- group and benzene ring are locked by the salt bridges among the SO_3^- groups and sodium (Na^+) ions not only in the L_c and $L_{\beta'}$ phases, but also in the fluid L_{α} phase. As a result, the orientation for the C-C bonds in the LAS alkyl chains is kept even in the L_{α} phase.

Chapter 2 is organized as follows. In Section 2.2, the MD simulations are described in detail. In Section 2.3, the results of analyses, focusing on lateral diffusion and reorientation, are presented. The relationship between the dynamics and conformational pattern of LAS alkyl chains is also discussed. Finally, conclusions are given in Section 2.4.

2.2. Simulation details

Figures 1.7(e), 1.10(a) and (c) show the equilibrated structures of the L_c , $L_{\beta'}$, and L_{α} phases, respectively, which were used as initial configurations in present chapter. The lamellar structure is arranged on the x - y plane and stacked along the z -axis under three-dimensional periodic boundary condition. It is composed of 200 LAS molecules, 200 water molecules ($N_h = 1$ for the L_c and $L_{\beta'}$ phases) or 800 water molecules ($N_h = 4$ for the L_{α} phase), and 200 Na^+ ions, where N_h is the hydration number of LAS. The three phases were in different thermodynamic conditions: $T = 300$ K and $P = 0.1$ MPa for the L_c phase, $T = 360$ K and $P = 0.1$ MPa for the $L_{\beta'}$ phase, and $T = 400$ K and $P = 0.1$ MPa for the L_{α} phase, where T and P are the temperature and hydrostatic pressure, respectively. A 1 μs long MD simulation was conducted for each system in the isothermal and isobaric conditions given

above. The other general conditions in execution of MD simulation are same with that described in Chapter 1.

2.3. Results and Discussion

Lateral Diffusion

The lateral self-diffusion coefficients D_L for LAS, Na^+ , and water in the L_c , $L_{\beta'}$, and L_{α} phases were calculated as

$$D_L = \lim_{t \rightarrow \infty} \frac{1}{4t} \text{MSD}(t), \quad (2.1)$$

where $\text{MSD}(t)$ is the two-dimensional mean squared displacement:

$$\text{MSD}(t) = \langle (\mathbf{r}_i(t) - \mathbf{r}_i(0))^2 \rangle. \quad (2.2)$$

In Eq. (2.2), $\mathbf{r}_i(0)$ and $\mathbf{r}_i(t)$ are the lateral locations of the center of mass of SO_3^- , Na^+ , or water on the x - y plane at times 0 and t , respectively. The collective motion of each monolayer was subtracted from the calculated MSD.^{76,77}

Figure 2.1(a) shows that the calculated MSD values for SO_3^- and Na^+ are undetectably small throughout the 500 ns in the L_c phase. The MSD for water slightly increased with time, but remained very small (0.51 nm^2), even at $t = 500 \text{ ns}$. Thus, LAS, Na^+ , and water did not diffuse laterally in the L_c phase within the considered time scale. Figure 2.1(b)

shows the calculated MSD values for SO_3^- , Na^+ , and water in the $L_{\beta'}$ phase. The calculated MSD values for SO_3^- and Na^+ are still as small as the intermolecular distance between adjacent LAS molecules (0.44 nm^2), even at $t = 500 \text{ ns}$. Lateral diffusion is very slow in this phase, too. In contrast, Figure 2.1(c) shows that the calculated MSD values for SO_3^- , Na^+ , and water in the L_{α} phase linearly increase with increasing t . The linear increase of MSD indicates that lateral diffusion occurred.

Table 2.1 lists the D_L values calculated using Eq. (2.1). In the L_c phase, the D_L values for SO_3^- and Na^+ could not be accurately determined due to their too small D_L values because of insufficient sampling of MSD. Although there are no reported values of D_L for LAS in the L_c phase, an extremely small value of $D_L = 4 \times 10^{-11} \text{ cm}^2/\text{s}$ has been reported for DPPC bilayers at low temperature (below the transition temperature from the L_{β} phase to the L_{α} phase).⁷⁸ Whereas, D_L for the water, ($D_{L,\text{water}} < 3 \times 10^{-10} \text{ cm}^2/\text{s}$) is much smaller than that for bulk water ($10^{-5} \text{ cm}^2/\text{s}$) at the same temperature. This indicates that water molecules are strongly confined in the small space between the hydrophilic surfaces of the lamellae.

For the $L_{\beta'}$ phase, the D_L values for SO_3^- and Na^+ , $D_{L,\text{sulfo}}$ and $D_{L,\text{sodium}}$, also could not be determined accurately, while the both D_L values are estimated to be in the order of $10^{-10} \text{ cm}^2/\text{s}$ from Figure 2.1(b). $D_{L,\text{sulfo}}$ and $D_{L,\text{sodium}}$ are roughly consistent to the D_L for DPPC in the L_{β} phase ($< 5 \times 10^{-10} \text{ cm}^2/\text{s}$) determined using fluorescence recovery after photobleaching.⁷⁹ In contrast, $D_{L,\text{water}} = 2.3 \pm 0.1 \times 10^{-9} \text{ cm}^2/\text{s}$, which is one order of magnitude greater than $D_{L,\text{sulfo}}$ and $D_{L,\text{sodium}}$. This indicates that water in the $L_{\beta'}$ phase has a relatively high lateral mobility compared with those for LAS and Na^+ .

For the L_α phase, $D_{L,\text{sulfo}} = 2.7 \pm 0.1 \times 10^{-7} \text{ cm}^2/\text{s}$, which is 1000 times greater than $D_{L,\text{sulfo}}$ for the $L_{\beta'}$ phase and is the same order of magnitude as the value for dioleoylphosphatidylcholine (DOPC) in the L_α phase determined by ^1H pulsed field gradient NMR diffusion measurements⁸⁰ ($D_{L,\text{DOPC}} = 2.6 \times 10^{-7} \text{ cm}^2/\text{s}$, $T = 333 \text{ K}$, 30 wt% aqueous solution). The large lateral diffusion coefficient for LAS in the L_α phase is in accordance with the general discussion of the classification of these lamellar subphases.²⁸

For the L_α phase, $D_{L,\text{water}} = 6.2 \pm 5 \times 10^{-6} \text{ cm}^2/\text{s}$, which is much larger than $D_{L,\text{sodium}} = 6.8 \pm 0.2 \times 10^{-7} \text{ cm}^2/\text{s}$. This difference may be attributed to a weaker coulomb interaction between water molecules and the SO_3^- head group compared to that between Na^+ ion and SO_3^- . Furthermore, the increase in the amount of highly diffusive water molecules not directly hydrated to Na^+ or SO_3^- may have a contribution to the high $D_{L,\text{water}}$. Note that there are four water molecules per LAS molecule in the L_α phase ($N_h = 4$). The number density profile along the z -axis shown in Figures 2.2(a)–(c) indicate that almost all Na^+ ions were solvated around SO_3^- , while water molecules migrated over a wider z -range, penetrating deeper into the hydrocarbon region in the L_α phase.

Reorientation of LAS

Next, conformational relaxation, which was caused by orientation around the molecular axis in the L_c , $L_{\beta'}$, and L_α phases, was investigated for LAS molecules. The time auto-correlation function $C_{\text{Reorient}}(t)$ can be expressed as

$$C_{\text{Reorient}}(t) = \frac{1}{2} \langle 3 \cos^2 \theta(t) - 1 \rangle, \quad (2.3)$$

where θ is the angle between two vectors $\mathbf{e}'_{ijk}(0)$ and $\mathbf{e}'_{ijk}(t)$ at $t = 0$ and $t = t$, respectively. $\mathbf{e}'_{ijk}(0)$ and $\mathbf{e}'_{ijk}(t)$ are projections of $\mathbf{e}_{ijk}(0)$ and $\mathbf{e}_{ijk}(t)$, respectively, onto the x - y plane, where \mathbf{e}_{ijk} is the unit vector that defines the orientation of each segment of LAS, namely SO_3^- (sulfo), benzene ring (benz), alkyl group bound to the benzene ring (root), and terminal alkyl group (term). The abbreviations in the parentheses are used in the following discussion. We define \mathbf{e}_{ijk} as a unit vector along the cross product of two vectors formed by the three atomic coordinates \mathbf{r}_i , \mathbf{r}_j , and \mathbf{r}_k in each segment.

\mathbf{r}_i , \mathbf{r}_j , and \mathbf{r}_k are defined by the following three atoms for each segment: O1, S, and C1 for sulfo, C1, C3, and C5 for benz, C4, C7, and C8 for root, and C16, C17, and C18 for term. The symbol of the atom is presented in Figure 1.1. An example of \mathbf{e}_{ijk} is shown in Figure 2.3 for SO_3^- .

Figures 2.4(a)–(d) the calculated $C_{\text{Reorient}}(t)$. The relaxation time τ for $C_{\text{Reorient}}(t)$ was obtained by fitting an analytical function to $C_{\text{Reorient}}(t)$. In most cases, $C_{\text{Reorient}}(t)$ can be approximated by a single exponential function, $\exp(-t/\tau)$. For sulfo and benz, as shown in Figures 2.4(a) and 2.4(b), respectively, two-step relaxation processes were observed. Therefore, a double exponential function, $A\exp(-t/\tau^{\text{fast}}) + B\exp(-t/\tau^{\text{slow}})$, was adopted as the fitting function, for which two relaxation times, τ^{fast} and τ^{slow} , were obtained. For root and term in the L_c and $L_{\beta'}$ phases, as shown in Figures 2.4(c) and (d), respectively, $C_{\text{Reorient}}(t)$ converged to a constant value greater than zero. For these cases, a function of the form $A\exp(-t/\tau) + C_{\text{Reorient},\infty}$ was adopted, where τ and $C_{\text{Reorient},\infty}$ were the fitting parameters. In

the fitting process, constraint conditions $A + B = 1$ for the double exponential function and $A + C_{\text{Reorient},\infty} = 1$ for the single exponential function with an offset value were applied.

Table 2.2 lists the calculated τ and $C_{\text{Reorient},\infty}$ values. For the L_c phase, τ_{benz} is the largest ($\tau_{\text{benz}}^{\text{slow}} > 20 \mu\text{s}$; $\tau_{\text{benz}}^{\text{fast}} = 56 \pm 1 \text{ ns}$), followed by τ_{sulfo} ($\tau_{\text{sulfo}}^{\text{slow}} > 3 \mu\text{s}$, $\tau_{\text{sulfo}}^{\text{fast}} = 33 \pm 1 \text{ ns}$). Values of τ^{slow} greater than $1 \mu\text{s}$ indicate that the conformations of SO_3^- and benzene ring only slightly relaxed from their initial configuration in the L_c phase during the $1 \mu\text{s}$ long MD simulation. τ_{root} and τ_{term} (18 ± 1 and $8.6 \pm 0.3 \text{ ps}$, respectively) are much smaller than τ_{sulfo} and τ_{benz} . These τ values, in the order of picoseconds, indicate that the LAS alkyl chain relaxed to its equilibrium conformation even in the L_c phase, even though surfactant molecules in the L_c phase are generally considered not to exhibit reorientation.^{28,38} The observed reorientational relaxation in the present MD simulations is related to *gauche* defects in the crystal structure, as discussed in detail in the following subsection.

For the $L_{\beta'}$ phase, $\tau_{\text{sulfo}}^{\text{slow}} = 690 \pm 10 \text{ ns}$ and $\tau_{\text{benz}}^{\text{slow}} > 2 \mu\text{s}$ are shorter than that for the L_c phase. $\tau_{\text{root}} = 15 \pm 1 \text{ ps}$ and $\tau_{\text{term}} = 5.1 \pm 0.2 \text{ ps}$, which are remarkably shorter than τ_{sulfo} and τ_{benz} and whose magnitude is similar to that for the L_c phase. In general, it is believed that reorientation around the molecular axis of linear surfactants occurs in the $L_{\beta'}$ phase. However, the estimated τ values in our MD simulations indicate that reorientation occurs at only the alkyl chains in the $L_{\beta'}$ phase.

For the fluid L_α phase, the relaxation time is within 5 ns for most segments of LAS: $\tau_{\text{sulfo}}^{\text{slow}} = 1.2 \pm 0.1 \text{ ns}$, $\tau_{\text{benz}}^{\text{slow}} = 3.9 \pm 0.1 \text{ ns}$, $\tau_{\text{root}} = 18 \pm 1 \text{ ps}$, and $\tau_{\text{term}} = 3.1 \pm 0.2 \text{ ps}$. These short τ values, with large $D_{\text{L},\text{sulfo}}$ for the L_α phase, illustrate that not only lateral diffusion

but also intra-molecular conformational changes occur frequently in the L_α phase, as observed for the lipid bilayers in the L_α phase.

$\tau_{\text{sulfo}}^{\text{slow}}$ and $\tau_{\text{benz}}^{\text{slow}}$ showing remarkably large values in the L_c and $L_{\beta'}$ phases can be explained as follows. Figure 2.5(a) shows the radial distribution function between the Na^+ and the oxygen atom of SO_3^- , $g_{\text{O-Na}^+}(r)$. The first peak of $g_{\text{O-Na}^+}(r)$ is very sharp and higher than 30 for three lamellar systems. Thus, the reorientation of the SO_3^- group can be assumed to be restricted by salt-bridging among the SO_3^- groups via Na^+ ions. This can make $\tau_{\text{sulfo}}^{\text{slow}}$ large. As shown in Figure 2.6, salt bridges are found everywhere in the inter-lamellae space in the L_c and $L_{\beta'}$ phases ($N_h = 1$). They are also observed in the L_α phase because of the low hydration number ($N_h = 4$).

For the L_c and $L_{\beta'}$ phases, as shown in Figure 2.5(b), the first peak of the radial distribution function between the centers of mass of the benzene rings, $g_{\text{Bz-Bz}}(r)$, is which is shorter than the width of the benzene ring on the x - y plane (6.0 Å). This means that some adjacent benzene rings are located at intervals shorter than the benzene ring width. Therefore, reorientation of the benzene rings should be significantly inhibited by the excluded volume of the adjacent benzene rings in the L_c and $L_{\beta'}$ phases, which corresponds to a large $\tau_{\text{benz}}^{\text{slow}}$ value. In contrast, the first peak of $g_{\text{Bz-Bz}}(r)$ for the L_α phase is lower and broader, indicating that the reorientation is allowed without strong steric hindrance.

Conformation of Alkyl Chain

As discussed above, the reorientation of the alkyl chain of LAS, which occurred independently of the head group, was observed for the L_c and $L_{\beta'}$ phases, although lateral translational diffusion hardly occurred, leading to a very small D_L . With the center of mass of LAS molecules almost fixed, the reorientation must occur in a restricted space. To clarify this mechanism, first the *gauche* fraction was evaluated as a function of C-C bond position in the alkyl chain. Then, the conformational pattern analysis proposed by Tu et al.³⁵ was performed to determine which conformation was primarily responsible for the reorientation.

Figure 2.7(a) shows the numbering of the C-C bonds adopted here. “B0” is defined to be the C7-C8 bond corresponding to α - β carbons of the alkyl group bound to the benzene ring. “B1” and “B2” are C8-C9 and C9-C10 bonds, respectively, followed by “B3” and the others. In total, ten C-C bonds were investigated in the conformational pattern analysis. Three conformers (*gauche+* ($g+$), *trans* (t), and *gauche-* ($g-$)) are defined for each C-C bond with the classification shown in Eq. (2.4).

$$0 < \varphi \leq \frac{2}{3}\pi : g +, \quad \frac{2}{3}\pi < \varphi \leq \frac{4}{3}\pi : t, \quad \frac{4}{3}\pi < \varphi \leq 2\pi : g -. \quad (2.4)$$

Figure 2.7(b) shows the calculated fraction of each conformation along the C-C bond. The *gauche* fraction, which is the sum of $g+$ and $g-$, increased in the order L_α , $L_{\beta'}$, and L_c . The fraction qualitatively corresponds to the calculated $C_{\text{Reorient},\infty,\text{root}}$ and $C_{\text{Reorient},\infty,\text{term}}$ values in the previous section. Note that a small *gauche* fraction corresponds to a high $C_{T,\infty}$, which reflects a residual orientational order of the alkyl chain. The *gauche* fractions for the

odd numbered C-C bonds (B1, B3, B5, and B7) were significantly larger than those for the even numbered C-C bonds (B0, B2, B4, B6, and B8) in the L_c and $L_{\beta'}$ phases. This odd-even effect was also observed for the fluid L_{α} phase.

The odd-even effect in the alkyl chain conformation has been confirmed by nuclear magnetic resonance for DPPC bilayers in the L_{α} phase,⁸¹ and by FT-IR for several kinds of phospholipid bilayer in the L_{α} phase and liquid n -alkanes.⁸² A conformational pattern analysis³⁵ showed that only the conformations such as *kink* and *jog*, which give rise to the odd-even effect, do not show a bend along the chain.⁸¹ We discuss the relationship between the odd-even effect and the conformational patterns by investigating the ratio of particular conformational patterns for each lamellar phase.

Figure 2.8 shows 11 kinds of representative conformational pattern of the alkyl chain that do not show a significant bend of the chain. *Gauche* fraction with respect to the odd-numbered bonds from B1 to B7 can be analyzed for these possible conformational patterns. The labels of the conformational patterns in Figure 2.8 are based on the numbers of $g+$ and $g-$ conformations,⁸¹ where “0 g ” represents the zero *gauche* conformation (all-*trans*), “1 g ” represents the one *gauche* conformation, “2 g 1 *kink*” represents a pair of $g+$ and $g-$ (or $g-$ and $g+$) conformations in adjacent odd-numbered C-C bonds, and so on. However, with this notation, the *gauche* position is arbitrary.

Table 2.3 shows the calculated probability distribution for each conformational pattern. The values in parentheses are partial contributions from the *gauche* conformation of the B1 bond, and the values without parentheses are the total contributions from B1 to B7. It is clear that the 0 g pattern is dominant (about 72 %) for the L_c phase. The remaining is mostly

the 1g and 2g1 *kink* patterns. For the $L_{\beta'}$ phase, the 0g pattern is most significant (about 37%), followed by the 1g and 2g1 *kink* patterns. For the L_{α} phase, the 0g pattern is no longer dominant but considerable (4% or less). The combined 1g and 2g1 *kink* patterns represent 15%, with various kinds of conformational pattern making up the rest.

Conventionally, it is believed that the L_c phase is composed of only the 0g pattern. This is inconsistent with the present simulations, where non-0g patterns account for 18% of patterns for the L_c phase (Table 2.3). However, a detailed FT-IR and LD study reported that there are *gauche* defects at the root of alkyl chains of SDS in the monohydrate crystal (the L_c phase).³⁸ The 1g and 2g1 *kink* patterns found in the L_c phase of LAS in this chapter are consistent with these experimental observations.

Origin of Odd-even Effect

In the following, we discuss the conformational patterns in which the B1 bond is involved. The results are presented in Table 2.3. The high *gauche* fraction at the odd-numbered bonds in Figure 2.7(b) can be explained as follows. For the L_c phase, the value of 15% for the *gauche* conformation at the B1 bond corresponds to the total probability of finding a *gauche* conformation at the B1 bond (14.6%, a summation over the values in parentheses in Table 2.3). Particularly, the 1g and 2g1 *kink* patterns are the main conformations (12.9%) for the *gauche* defects. For the $L_{\beta'}$ phase, the value of 32% for the *gauche* conformation at the B1 bond does not correspond to the total probabilities of the patterns with a *gauche* conformation at the B1 bond (20.3%). This 12% difference is accounted for by conformational patterns other than the 11 major patterns in Figure 2.8,

possibly *gauche* conformations in the even-numbered C-C bonds. Thus, the odd-even behavior of the *gauche* fraction for the L_c and $L_{\beta'}$ phases can be related to the ratio of the major conformational patterns of the LAS alkyl chains shown in Table 2.3. For the L_{α} phase, the high *gauche* probability at the B1 bond cannot be explained by the 11 major conformational patterns, since they are mainly from random conformations at high temperatures.

The *gauche* fraction at other odd-numbered bonds can also be interpreted by the probability of each conformational pattern listed in Table 2.4. For example, for the B3 bond, the total *gauche* probability summed over the 11 major conformational patterns is 4.8% for the L_c phase which correspond well to the *gauche* fractions at the B3 bond, 4.8% given in Figure 2.7(b).

The odd-even effect in the *gauche* fraction along the alkyl chain was also observed for the L_{α} phase, as shown in Figure 2.7(b). This is due to the restricted orientation of particular C-C bonds of the alkyl chain in the L_{α} phase. Figure 2.9 shows that the SO_3^- and odd-numbered C-C bonds tend to be oriented along the bilayer normal with higher order than that of the even-numbered C-C bonds. The low order of the even-numbered C-C bonds is caused by the connection to the odd-numbered ones via sp_3 carbon with a bend angle of 109.5° . The even-numbered C-C bonds are thus inclined to the bilayer normal. However, the tilted orientation of alkyl chains hinders such structure sterically in the lamellar. The structure should bend again at the next odd-numbered bond with the *gauche* conformation, restoring an orientation that is nearly parallel to the bilayer normal. This mechanism repeats

to the tail ends and gives the odd-even effect for the *gauche* fraction, as shown in Figure 2.7(b).

Parallel orientation to the z -axis found for the odd-numbered C-C bonds could be explained by the salt bridge between SO_3^- and Na^+ , as discussed above for Figure 2.5(a). The extremely small amount of water between lamellae also causes salt bridges that extend to the whole space of the inter-lamellae layers (see Figure 2.6). These salt-bridged SO_3^- groups are forced to be oriented parallel to the z -axis, resulting in higher ordered C-C bonds bound to the benzene ring. The odd-even effect following this mechanism partially occurs even in the L_α phase because of its small hydration number ($N_h = 4$) compared with that for phospholipid bilayers in the L_α phase ($N_h = 20$ or more).

Conformational patterns also explain why relaxation of the reorientation can occur in the tilted alkyl tails in the L_c and $L_{\beta'}$ phases. As shown in Figure 2.8, the direction of the tilt of the terminal alkyl group in the $1g$ and $2g1$ *kink* patterns is the same as that found in the $0g$ pattern. Therefore, it is possible to change the pattern from $0g$ to $1g$ or $2g1$ *kink* by reorientation without changing the direction of the alkyl group. This is the mechanism by which conformational relaxation of alkyl groups can occur even in the L_c and $L_{\beta'}$ phases. It is also inferred that these conformations in the L_c and $L_{\beta'}$ phases greatly contribute to the lamellar structure by keeping the direction of the alkyl chain unchanged.

2.4. Conclusions

The lamellar structure produced by linear surfactants exhibits several subphases, such as L_c , L_β , $L_{\beta'}$, and L_α phases depending on temperature, pressure, and hydration. In this chapter, 1 μ s long MD simulations were performed for the lamellar structure of sodium LAS in the L_c , $L_{\beta'}$, and L_α phases to clarify the dynamics of LAS molecules in these phases. Lateral diffusion was observed only in the L_α phase. The lateral self-diffusion coefficient was on the same order of magnitude as that found for phospholipid bilayers in the L_α phase. In the L_c and $L_{\beta'}$ phases, the conformation of LAS molecules is relaxed by the reorientational motion of the segments, namely SO_3^- group, benzene ring, and flexible alkyl chain, with different time constants. For all three phases (L_c , $L_{\beta'}$, and L_α), a significant odd-even effect was observed in the *gauche* conformation fraction along the alkyl chain of LAS. The conformational pattern analysis revealed that the odd-even effect results from particular conformational patterns. The high order of C-C bond orientation at the odd-numbered bonds is caused by the salt bridges between the SO_3^- group and Na^+ ions, and sometimes spreads over the inter-lamellae space under a low hydration level. Furthermore, it was found that the transition of conformational patterns from *0g* to *1g* or *2g1* *kink* allows the alkyl group to relax by reorientation, even in the L_c and $L_{\beta'}$ phases. The conformational degree of freedom greatly contributes to the lamellar structure by keeping the direction of the alkyl chain.

The findings in this chapter are applicable to the discussion of the microscopic states of molecules in the lamellar structure of other LAS isomers.

Table 2.1. Calculated D_L values for sulfonate (SO_3^-), sodium ion (Na^+), and water (units: $10^{-7} \text{ cm}^2/\text{s}$).

	$D_{L,\text{sulfo}}$	$D_{L,\text{sodium}}$	$D_{L,\text{water}}$
L_c	-	-	< 0.003
L_β	< 0.002	< 0.002	0.023±0.001
L_α	2.7±0.1	6.8±0.2	62±5

Table 2.2. Calculated τ and $C_{\text{Reorient}, \infty}$ for SO_3^- (sulfo), benzene ring (benz), aliphatic carbon bonded to benzene (root), and terminal aliphatic carbon (term) in LAS molecules. Two relaxation times for sulfonate and benzene ring were observed, as shown in the table (upper: τ^{fast} and lower: τ^{slow}).

	τ_{sulfo} (ps)	τ_{benz} (ps)	τ_{root} (ps)	$C_{\text{Reorient}, \infty, \text{root}}$	τ_{term} (ps)	$C_{\text{Reorient}, \infty, \text{term}}$
L_c	$3.3 \pm 0.1 \times 10^4$ $> 3 \times 10^6$	$5.6 \pm 0.1 \times 10^4$ $> 2 \times 10^7$	18 ± 1	0.78 ± 0.01	8.6 ± 0.3	0.3 ± 0.1
$L_{\beta'}$	$3.3 \pm 0.1 \times 10^4$ $6.9 \pm 0.1 \times 10^5$	$5.0 \pm 0.1 \times 10^4$ $> 2 \times 10^6$	15 ± 1	0.61 ± 0.01	5.1 ± 0.2	0.04 ± 0.01
L_α	$1.4 \pm 0.1 \times 10^2$ $1.2 \pm 0.1 \times 10^3$	$3.7 \pm 0.1 \times 10^2$ $3.9 \pm 0.1 \times 10^3$	18 ± 1	0	3.1 ± 0.2	0

Table 2.3. Calculated probability distribution for conformational patterns of alkyl chain of LAS in three lamellar phases. The values in parentheses are partial contributions from the *gauche* conformation of the B1 bond, and the values without parentheses are the total contributions from B1 to B7 bonds.

	0g	1g	2g1 <i>kink</i>	3g2 <i>kink</i>	4g3 <i>kink</i>	2g2 <i>jog</i>	2g3 <i>jog</i>	3g <i>kink</i> <i>jog</i>	3g2	3g3	4g3
L_c	71.9 (-)	14.0 (10.9)	4.1 (2.0)	0.4 (0.3)	0.2 (0.2)	0.3 (0.1)	0.5 (0.5)	0.5 (0.5)	0.1 (0.1)	0 (0)	0 (0)
$L_{\beta'}$	36.6 (-)	20.9 (10.9)	7.9 (3.1)	1.6 (0.9)	0.6 (0.6)	1.3 (0.7)	1.5 (1.5)	1.7 (0.5)	0.7 (0.3)	0.5 (0.5)	0.2 (0.2)
L_{α}	3.6 (-)	11.4 (3.5)	3.6 (1.4)	1.1 (0.7)	0.2 (0.2)	2.3 (1.3)	1.1 (1.1)	1.0 (1.0)	1.2 (0.7)	1.0 (1.0)	0.3 (0.3)

Table 2.4. Calculated probability distribution of conformation patterns for alkyl chain of LAS which contribute to the *gauche* conformation in the B3 (upper), B5 (middle) and B7 bonds (lower) in the L_c , $L_{\beta'}$ and L_{α} phases.

	0g	1g	2g1 <i>kink</i>	3g2 <i>kink</i>	4g3 <i>kink</i>	2g2 <i>jog</i>	3g <i>kink</i> <i>jog</i>	3g2	2g3 <i>jog</i>	3g3	4g3
L_c	-	0.4	3.0	0.3	0.2	1.3	0.2	0.1	-	0	0
	-	0.2	4.1	0.4	0.2	1.2	0.3	0.1	-	0	0
	-	2.6	2.1	0.2	0.2	1.3	0.5	0	0	0	0
$L_{\beta'}$	-	1.1	5.2	0.9	0.6	0.6	0.8	0.7	-	0.2	0.2
	-	1.4	7.9	1.6	0.6	0.7	0.9	0.7	-	0.2	0.2
	-	7.5	4.8	0.7	0.6	0.6	1.7	0.3	1.5	0.5	0.2
L_{α}	-	2.8	2.6	0.7	0.2	1.0	0.5	1.2	-	0.5	0.3
	-	2.6	3.6	1.1	0.2	1.3	0.5	1.2	-	0.5	0.3
	-	2.6	2.2	0.4	0.2	1.0	1.0	0.5	1.1	1.0	0.3

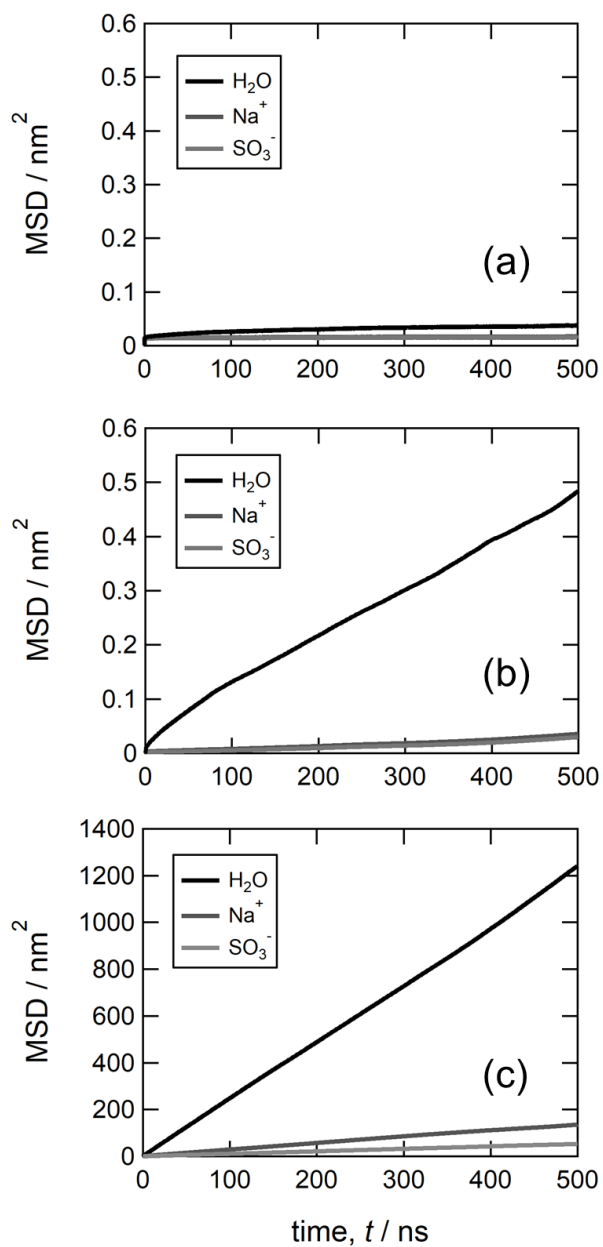


Figure 2.1. Lateral mean square displacement (MSD) of H_2O , Na^+ and SO_3^- groups in (a) L_c , (b) $L_{\beta'}$ and (c) L_α phase.

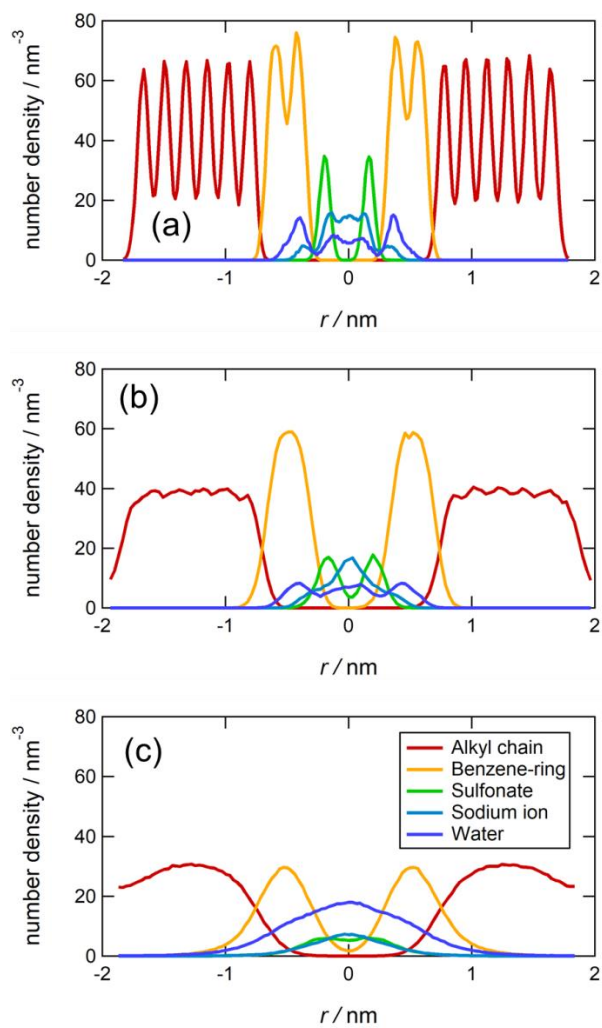


Figure 2.2. Number density profiles along the z -axis for each segment of LAS, Na^+ , and water in (a) L_c , (b) $L_{\beta'}$, and (c) L_{α} phase which correspond to Figure 1.7(e), Figures 1.10(a) and (c), respectively.

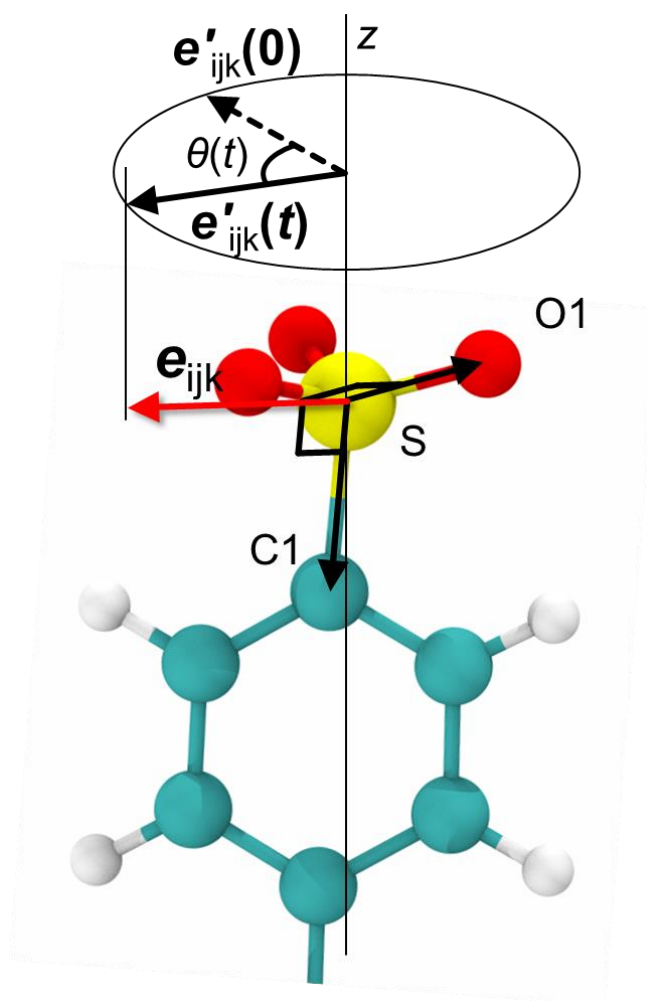


Figure 2.3. Definition of e_{ijk} and $\theta(t)$ in the autocorrelation function $C_{\text{Reorient}}(t)$ for SO_3^- .

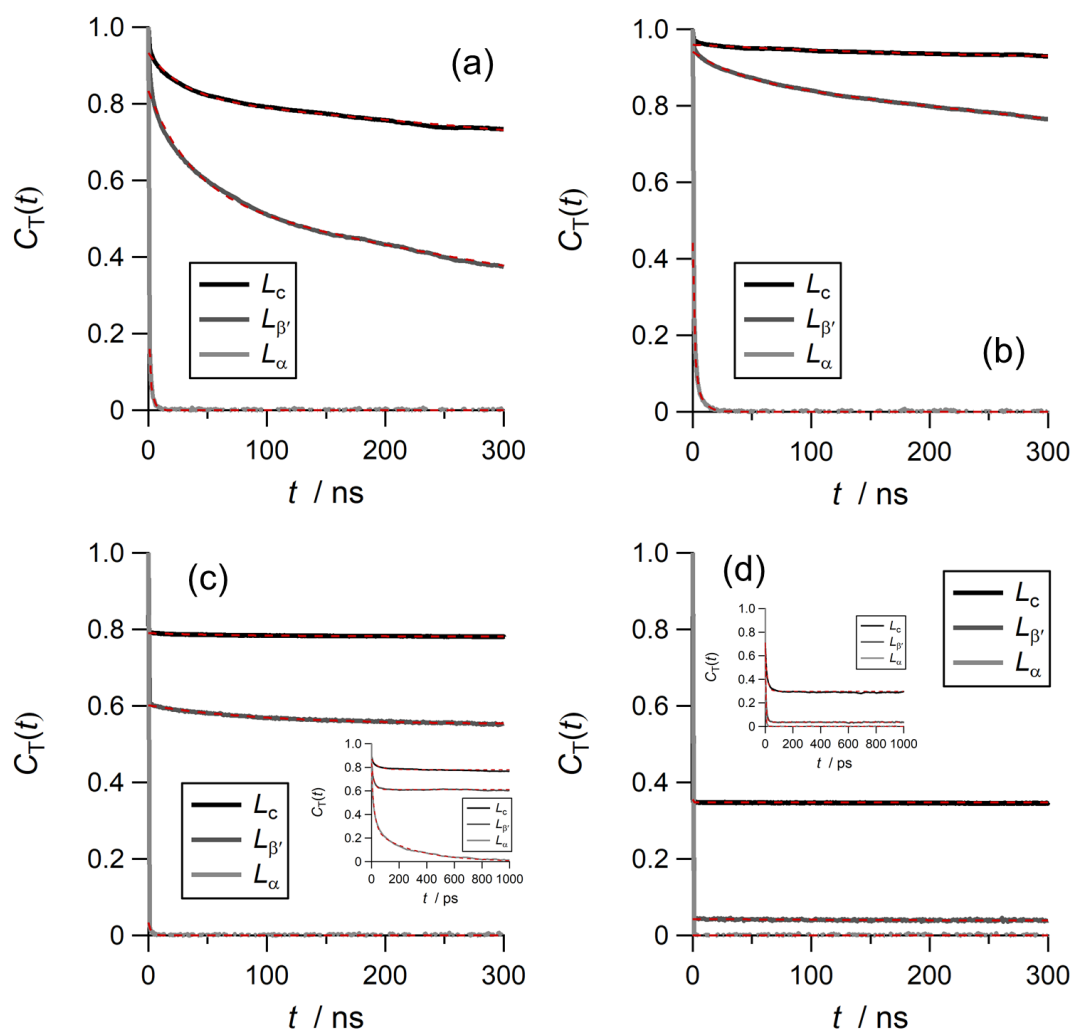


Figure 2.4. Calculated reorientation autocorrelation function $C_{\text{Reorient}}(t)$ of each part of the LAS molecule. (a) SO_3^- group: sulfo, (b) benzene ring: benz, (c) the alkyl group near the benzene ring: root and (d) terminal of alkyl chain: term. Fitting lines are indicated by red dashed lines. Insets on the panels (c) and (d) are zoomed images of $C_{\text{Reorient}}(t)$ in the first 10 ns period.

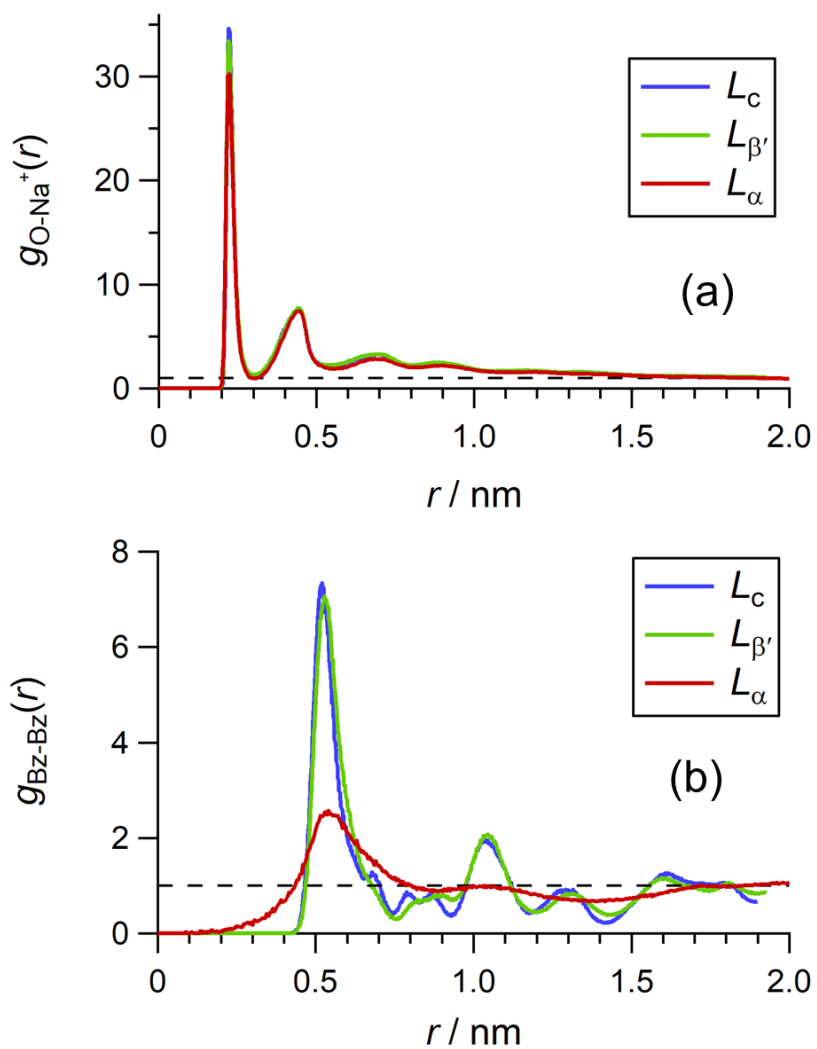


Figure 2.5. Calculated radial distribution function (a) between the sulfonate oxygen and Na^+ , $g_{O-Na^+}(r)$, and (b) between the centers of mass of the benzene ring, $g_{Bz-Bz}(r)$, in the L_c , $L_{\beta'}$, and L_α phases. Dashed line indicates $g(r) = 1$.

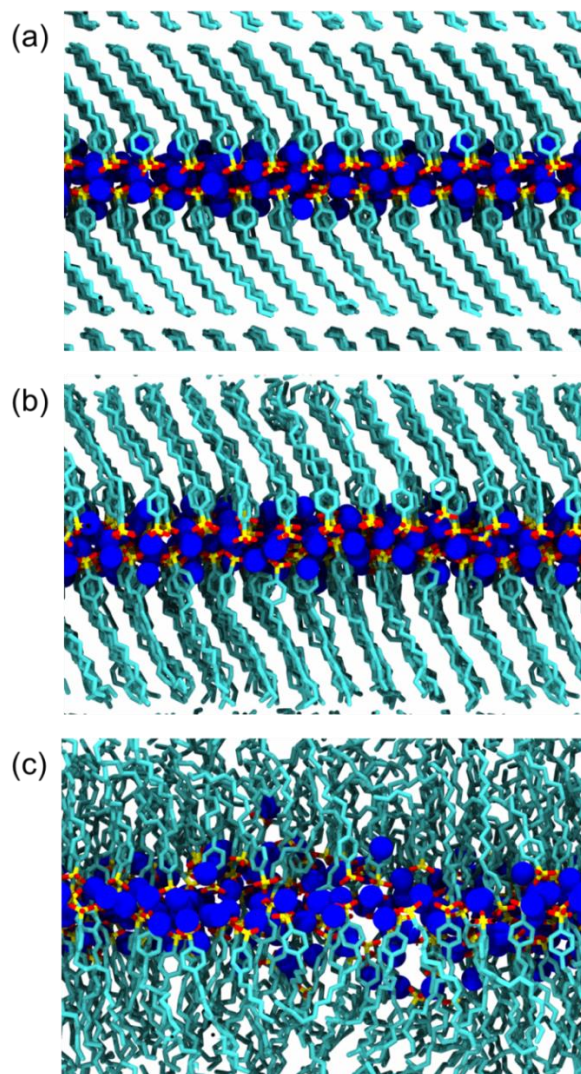


Figure 2.6. Captured images of lamellar structures of LAS at the inter-lamellae region in the (a) L_c ($N_h = 1$), (b) $L_{\beta'}$ ($N_h = 1$) and (c) L_{α} phase ($N_h = 4$). Blue spheres represent sodium ions, most of which form salt-bridges with SO_3^- groups (bars in yellow: sulfur, and red: oxygen). Cyan-colored bars are carbons in LAS, while hydrogen atoms in LAS and water molecules are not shown.

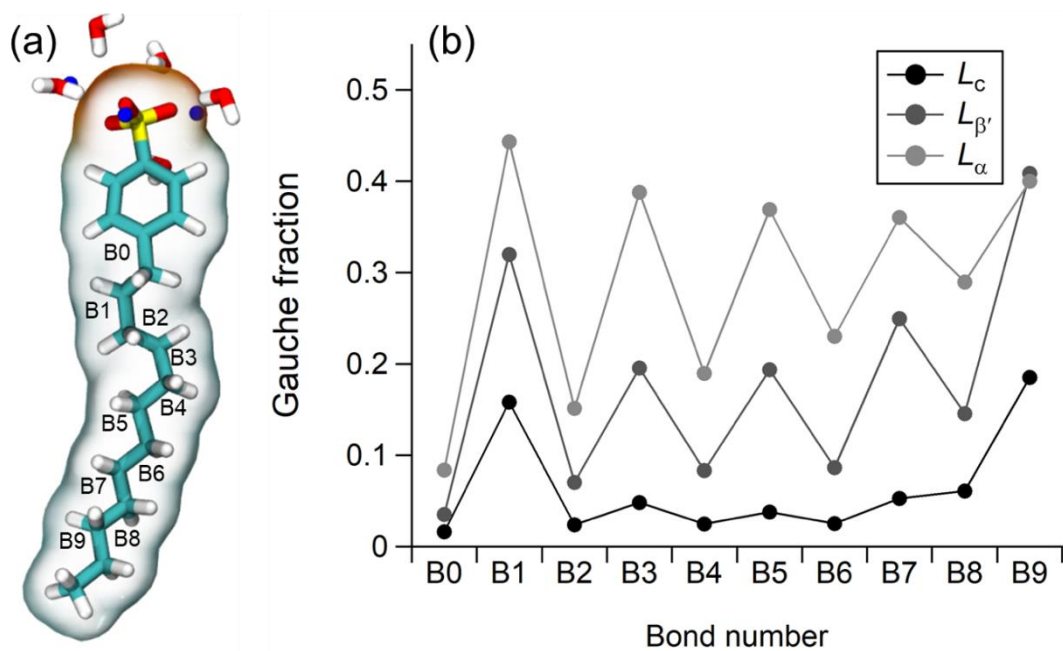


Figure 2.7. (a) Labels of CC covalent bonds used in the conformational analyses, and (b) calculated *gauche* fraction as a function of the position of C-C bond in the alkyl chain in the L_c , $L_{\beta'}$, and L_{α} phases.

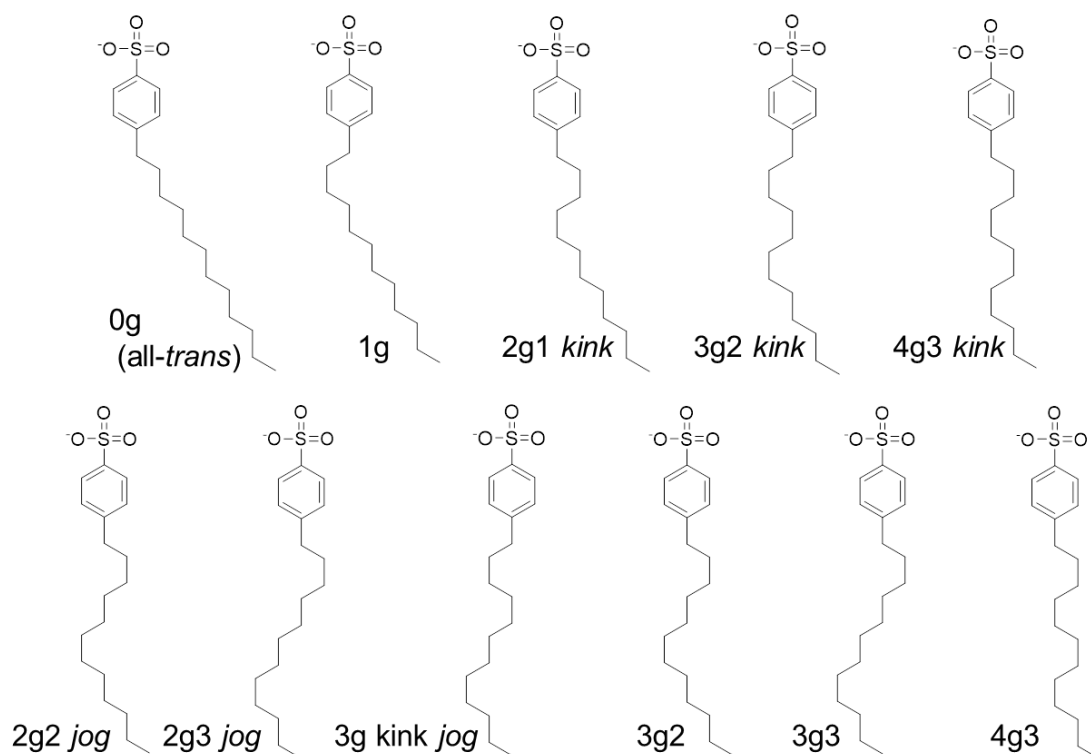


Figure 2.8. Two-dimensional chemical structure of the 11 major conformational patterns of LAS alkyl chains.

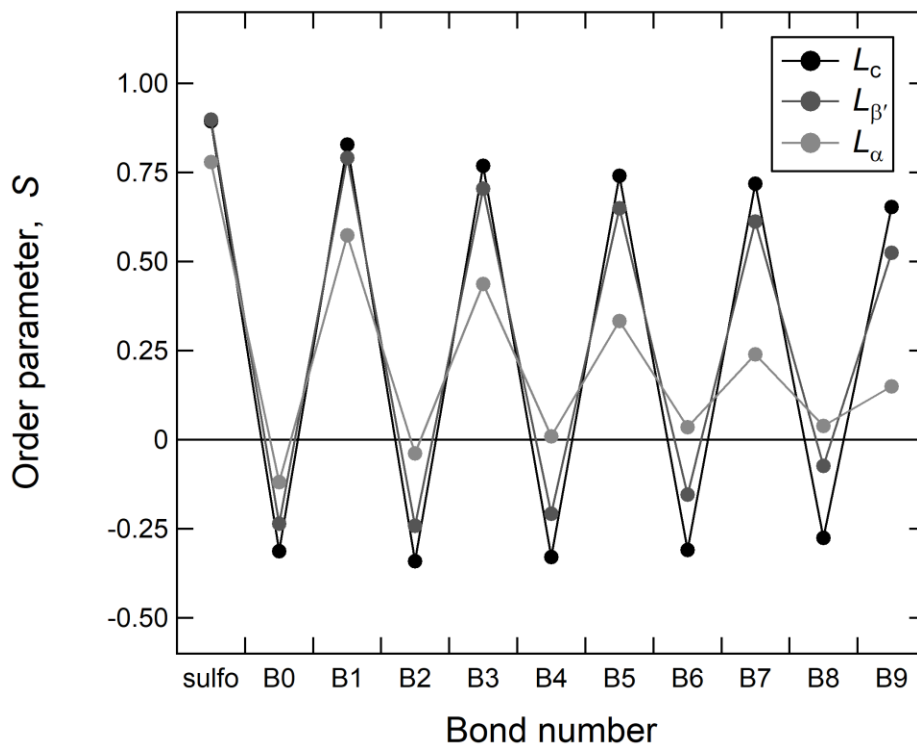


Figure 2.9. Order parameters $S = \frac{1}{2} \langle 3 \cos^2 \theta - 1 \rangle$ of S-C1 bond in the SO_3^- group and each C-C bond in the alkyl chain of LAS, where θ is the angle between the bond and the bilayer normal (the z axis). Calculated S for the S-C1 bond and the odd-numbered C-C bonds near the benzene ring showed a value close to 1 in each phase. In the L_c and $L_{\beta'}$ phases, calculated S are negative for the all even-numbered C-C bonds, while only the first two even-numbered C-C bonds (B0, B2) are negative in the L_{α} phase.

Chapter 3. Molecular dynamics study of solubilization of cyclohexane, benzene, and phenol into mixed micelles composed of sodium dodecyl sulfate and octaethylene glycol monododecyl ether

3.1. Introduction

Solubilization, an important property of micelles,⁸⁻¹⁰ is applied in a variety of fields, including cleaning,^{6,83} cosmetics,^{84,85} pharmaceuticals,^{86,87} and oil recovery in oil fields.⁸⁸ In these applications, multiple surfactants are commonly used. In particular, in cleaning and cosmetics, it is common to use a combination of multiple surfactants to obtain the desired lathering and texture.^{11,89,90} The surfactants form a mixed micelle in solution.

The mixing of surfactants affects the physical properties of micelles. For example, sodium dodecyl sulfate (SDS), which is widely used as a detergent, is often mixed with octaethylene glycol monododecyl ether ($C_{12}E_8$) to reduce skin irritation. The mixing of a small amount of $C_{12}E_8$ into SDS greatly reduces the critical micelle concentration.^{8,11} Furthermore, it has been reported that solubilization is also affected by mixing surfactants.^{45,46} The effects are due to the molecular-level interaction between micelles and solute molecules. However, little is known about the microscopic effects of the mixing of surfactants on the solubilization.

Molecular dynamics (MD) simulations can be used to clarify the influence of mixing of the surfactants on solubilization from a microscopic viewpoint. Many studies have applied MD simulations to investigate solubilization.⁴⁷⁻⁵¹ However, few of them considered mixed micelles, possibly because there are few experimental data on their aggregation number and composition.

In this chapter, we investigate a mixed micelle composed of SDS and C₁₂E₈ (see Figure 3.1), for which the aggregation number is known from experiments. We carried out MD simulations to examine solubilization for various SDS/C₁₂E₈ compositions. From the MD simulations for each composition, the corresponding equilibrium micelle structure was obtained. Then, the free energy profile, $\Delta G(r)$, for the solubilization of solute molecules from the bulk water phase into the micelle center was calculated using the thermodynamics integration method based on MD simulations. To focus on the relationship between the molecular interactions and solubilization of solute molecules, the cyclic compounds, cyclohexane, benzene, and phenol, which commonly consist of six carbons (C₆) and have similar molecular size but different polarity, were examined. Based on $\Delta G(r)$, we discuss the relationship between the solubilization of the solute molecules and the mixing state of the surfactant molecules.

The rest of this chapter is organized as follows. In section 3.2, the MD simulations are described in detail. In section 3.3, the equilibrium structure of the mixed micelles of SDS/C₁₂E₈, the $\Delta G(r)$ for the solubilization of the C₆ cyclic compounds into the mixed micelle, and the relationship between the micelle structure and $\Delta G(r)$ are discussed. Finally, in section 3.4, a conclusion of this chapter is presented.

3.2. Simulation details

In this chapter, we conducted MD simulations for the mixed micelle solution with the compositions of SDS/C₁₂E₈ = 100/0, 80/20, 60/40, 40/60, 20/80, and 0/100 (mol/mol), and then carried out simulations for the mixed micelle solution in which cyclohexane, benzene, and phenol molecules were to be solubilized.

For the first MD simulation, the aggregation number of the mixed micelles was taken to be that determined experimentally using the time-resolved fluorescence quenching technique.⁹¹ Although the aggregation number of the mixed micelles is available as a function of experimentally prepared composition, there is no information about the microscopic SDS/C₁₂E₈ composition in the micelles. Here, it is assumed that the mixing ratios of these two are the same.

The dodecyl sulfate (DS) ions of SDS and C₁₂E₈ molecules were randomly placed such that the end of the hydrophobic group and the hydrophilic group were oriented toward the inside and outside of the micelle, respectively. The numbers of DS ions and C₁₂E₈ molecules in the six mixed micelles satisfied the respective compositions (Table 3.1). The micelle was placed at the center of a cubic cell with a side length of 120 Å, and 50,000 water molecules were placed in the remaining part of the cell. Na⁺ ions, whose number was the same as that of DS ions, were randomly placed in the bulk water phase. Ten initial configurations were prepared independently for each composition, thus, for a total of 60 configurations. Energy minimization was first carried out using the steepest descent

method⁶² for each initial configuration. NVT ensemble MD simulation at temperature $T = 300$ K was performed for 20 ps, and NPT ensemble MD simulation at $T = 300$ K and pressure $P = 0.1$ MPa was performed for 1 ns to equilibrate the structure of the micelles and the distribution of ions and water molecules. Then, NPT ensemble MD simulation at $T = 300$ K and $P = 0.1$ MPa was performed for 10 ns for each micelle without solute as a production run.

For the solubilization MD simulation, cyclohexane, benzene, and phenol molecules were introduced into each of the micellar solutions prepared in the first simulation. There, one cyclohexane, benzene, or phenol molecule was inserted near the centers of mass of the micelle. The solute molecule was moved from the micelle center of mass to the bulk water phase at a constant rate of 10 \AA/ns . The coordinates at which the solute was placed were obtained for distances of 1, 5, 10, 15, 20, 25, 30, 35, 40, 45, and 50 \AA from the centers of mass of the micelle. We performed 1 ns for cyclohexane and benzene and for 10 ns for phenol in NPT ensemble MD simulations. In these MD simulations, the average force⁹²

$$F(r) = \left(\sum_{i \in N_s} \frac{M_m}{M_m + M_s} \mathbf{F}_i(r) - \sum_{j \in N_m} \frac{M_s}{M_m + M_s} \mathbf{F}_j(r) \right) \cdot \mathbf{u}, \quad (3.1)$$

was evaluated while constraining the distance r between the centers of mass of the micelle and the solute molecule using the SHAKE/RATTLE algorithm.⁹³ Here, $\mathbf{F}_i(r)$ is the force acting on atom i , M is the mass, and N is the number of atoms. The subscripts m and s attached to M and N indicate micelle and solute molecules, respectively. \mathbf{u} is a unit vector orienting toward the solute center of mass from the micelle center of mass. For solute

molecules moving from the bulk water phase to the micelle center of mass, the free energy profile⁹⁴ as a function of r can be evaluated as

$$\Delta G(r) = \int_{r_0}^r \langle F(r') \rangle dr', \quad (3.2)$$

where reference point $r = r_0$ is set in the bulk water phase. $\langle \dots \rangle$ represents an ensemble average. The TIP4P model was used as the water model.⁶⁶ CHARMM35r⁹⁵ was adopted for the force field of the polyoxyethylene (POE) group of C₁₂E₈, and CHARMM36⁹⁶ was used for those of other components. Other general MD conditions are same of previous chapters. Packmol⁹⁷ was used to construct the micelle structure. The MD simulation package GROMACS-5.0.4 was used.⁷⁰

3.3. Results and Discussion

In this section, we discuss the relationship between the micelle structural change caused by a composition change of the mixed micelle and the solubilization of the solute molecules into the micelle.

Structure of mixed micelle

Figure 3.2 shows the radial density profiles $\rho(r)$ of the hydrophilic and hydrophobic groups of DS ions and C₁₂E₈ molecules, Na⁺ ions, and water molecules in the mixed micellar solution for six compositions. As clearly shown in the figure, the distributions

change considerably depending on the composition, indicating that the micelle structure formed by hydrophobic groups and hydrophilic ones changes significantly. From the figure, we can also find that distribution of the hydrophobic and hydrophilic groups shifts to greater r with increasing $C_{12}E_8$ fraction. This is consistent with the increase in the amount of long $C_{12}E_8$ molecules as well as the change of the micellar size given in Table 3.1.

Hydrophilic group

Here, we focus on the distribution width of $\rho(r)$ for the hydrophilic POE group of $C_{12}E_8$. For SDS/ $C_{12}E_8 = 80/20$ and $60/40$ (i.e., low $C_{12}E_8$ content), the full width at half maximum of $\rho(r)$ for the hydrophilic group was 6.2 and 7.5 Å, respectively. These values are only 52% and 63% of that (11.9 Å) for SDS/ $C_{12}E_8 = 0/100$, and are close to that for the sulfate group of SDS (5.3 Å) (Figures. 3.2(b)–(f)). The mechanism that produces this compact structure of the POE group is discussed below.

Rosen and Kunjappu reported that, in a mixed micelle of SDS and $C_{12}E_m$, there are strong attractive interactions between the different surfactant molecules in the micelle.⁸ It was also pointed out that the POE group in $C_{12}E_m$ becomes positively charged by forming a complex with the Na^+ ion, and that electrostatic attraction is generated between this complex and the hydrophilic group of the counter anionic surfactant.

From the atomic trajectories obtained in our MD simulations, given in Figure 3.3(a), it was observed that the POE group captures a Na^+ ion in solution and wraps around it to form a crown-ether-like complex. Furthermore, it was also observed that the POE group retained the Na^+ ion for several nanoseconds and then released it, changing to a

conformation similar to the extended chain shown in Figure 3.3(b). Figure 3.3(c) shows the calculated radius of gyration, R_G , of a typical single POE group (black line) when it captures a Na^+ ion and R_G of other 29 POE groups (gray lines) in the system. The black line clearly shows that R_G was about 4 Å when the POE captures a Na^+ ion and it increased to about 7 Å after the release of the Na^+ ion. Our MD calculations were thus able to clarify the structure suggested by experiments. Note that the gray lines show that they cover their full fluctuations (average and standard deviation of R_G over all the POE groups were $R_{G,\text{avg}} = 5.1$ Å and $R_{G,\text{std}} = 0.7$ Å, respectively). This indicates that our statistics is enough to evaluate free energy of solubilization.

To analyze this quantitatively, C_{12}E_8 in which three or more oxygen atoms of the POE group simultaneously exist at a distance of 4 Å or less from a Na^+ ion⁹⁸ was regarded as the molecule that captured a Na^+ ion. Figures 3.4(a) and (b) show the number of such C_{12}E_8 molecules and the ratio of such C_{12}E_8 molecules to the total number of C_{12}E_8 molecules, respectively. The POE group that captures the Na^+ ion was observed for all compositions except for pure SDS and C_{12}E_8 micelles. In mixed micelles with $\text{SDS}/\text{C}_{12}\text{E}_8 = 80/20$ or $60/40$, a large number of Na^+ ions were attached to the POE groups, i.e., 50% and 45% of C_{12}E_8 molecules captured Na^+ ions, respectively. The tendency to form the complex was particularly strong when SDS content was high. Thus, the radial density distribution of the POE group narrowed in the mixed micelle with high SDS content because the POE group captured a Na^+ ion to form a complex, becoming compact.

Furthermore, the interaction between C_{12}E_8 molecules and DS ions in the micelle was investigated using the radial distribution function $g(r)$ for the oxygen atom of the sulfate

group, Os, the oxygen atom of the POE group, Op, and the Na⁺ ion. The results are presented in Figure 3.5(a) together with a schematic drawing in Figure 3.5(b) for the bridging geometry between hydrophilic POE and sulfate groups by the Na⁺ ion, which is inferred from the radial distribution functions as discussed below. The first peak positions of $g_{\text{Os-Na}}(r)$ and $g_{\text{Op-Na}}(r)$ are both at about 2.2 Å, representing direct bindings of the oxygen atoms to the Na⁺ ion. They are close to the sum of the atomic radius of O and the ionic radius of Na⁺. The second peak of $g_{\text{Os-Na}}(r)$ found at 4.4 Å represents a still high correlation between the Na⁺ ion and other three sulfate oxygen atoms covalently bonded to the sulfur atom as shown schematically in Figure 3.5(b). Further, with respect to $g_{\text{Os-Op}}(r)$ representing the correlation between oxygen atom of the sulfate group and oxygen atom of the POE group, a small and broad but clear distribution is observed at around 3.0 Å. Since the two oxygen atoms have charges of the like sign, repulsive forces should act between them. However, the distance between them is very short. This corresponds to the case where the two oxygen atoms are strongly bound to the central Na⁺ ion as shown above. Oxygen atoms in the folded POE group (Op) surround a Na⁺ ion as shown in Figure 3.3(a). Then, the oxygen of sulfate group (Os) is located such that the angle formed by Op-Na⁺ and Os-Na⁺ vectors is approximately 90° since a small peak of $g_{\text{OsOp}}(r)$ is found at 3.1 Å (= 2.2 Å × √2) as shown in Figure 3.5(b). Further, the second correlation is found at around 4.5 Å. This may also be explained to be an indirect correlation between the two oxygen atoms via the Na⁺ ion and the covalent bonds in the sulfate group. The Na⁺ ion, thus, bridges the two hydrophilic groups by its strong coulomb interactions.

Hydrophobic core

SDS and C₁₂E₈ have the same hydrophobic dodecyl group, which forms the hydrophobic core of the micelle. However, as shown in Figure 3.2, in the mixed micelle, the hydrophobic group of SDS is distributed outside the C₁₂E₈ alkyl group in the micelle core. This is considered to be related to the bridging between the Op and Os atoms by a Na⁺ ion discussed above. As shown in Figure 3.5(c), the trapping of the Na⁺ ion by the POE group can occur anywhere in the POE group irrespective of the conformation of the POE, that is, whether the POE is folded or extended. Then, the Na⁺ ion can be bound to the Op atom in the vicinity of the alkyl group and near the terminal hydroxyl group. If the capture of Na⁺ ions occurs near the end hydroxyl group, this site will interact strongly with the Os atom. On the other hand, when the POE has an unfolded conformation, the hydrophobic groups of C₁₂E₈ will be distributed more inward toward the micelle center compared to the hydrophobic group of SDS. This may be explained as follows. As shown in Figure 3.5(c), if Os atom is bound to any Op atoms in a C₁₂E₈ via Na⁺ ion, the hydrophobic core of SDS should be located outer than that of the C₁₂E₈ in the mixed micelles. Furthermore, since the sulfate anion of SDS is more hydrophilic than POE group of C₁₂E₈^{99,100}, it should be located outer than that of C₁₂E₈. In fact, top of the peak of the number density profile for sulfate group and Na⁺ ion is located at outer positions than that of POE groups as shown in Figure 3.6 (e.g. in SDS/C₁₂E₈ = 80/20, $r_{\max}^{\text{sulfate}} = 19.6 \text{ \AA}$ and $r_{\max}^{\text{POE}} = 17.5 \text{ \AA}$). Thus, it was found that the interaction between SDS and C₁₂E₈ through Na⁺ ions causes the radial distribution of the surfactants within the micelle to become heterogeneous.

Free energy profiles $\Delta G(r)$ of solute molecules

In the previous subsection, it was revealed that a mixing of the surfactants changes the structure of the hydrophilic group of the micelle and the radial density distribution of the hydrophobic group. Now, it is interesting to discuss about the change in solubilization ability caused by this structural change.

Validity of free energy profile calculation

Figure 3.7 shows the free energy profile, $\Delta G(r)$, of a solute molecule transferred from the bulk water phase to the micelle center of mass. Structural relaxation of POE group is slow taking a few nanoseconds, attributed to its slow conformational change. However, statistical sampling for $\Delta G(r)$ is sufficient by taking an average over many surfactant molecules involved in the micelles. As clearly shown in Figure 3.8, trajectory of a solute molecule, for example, at $r = 20 \text{ \AA}$ where the highest number density of POE group is found for SDS/C₁₂E₈ = 60/40, covers entire spherical shell, which indicates that the solute molecule fully experiences micellar environment produced by the surfactant molecules. Further, the force was averaged over ten independent 10 ns-long trajectories starting from ten different initial configurations. First, the simulation results are compared with those reported in previous studies. For benzene, $\Delta G(r)$ at the center of an SDS micelle was reported by Ingram et al. to be -16 kJ/mol ,⁵⁸ and by Matubayasi et al. to be -21 kJ/mol ,⁵⁴ which is in fair agreement with the value for the SDS micelles obtained here ($-10 \pm 9 \text{ kJ/mol}$). For the solubilization of cyclohexane into SDS micelles, the calculated free energy of transfer from the bulk water to the micelle in Figure 3.7(a) was $-22 \pm 10 \text{ kJ/mol}$. This is

in good agreement with the value $\Delta G = -20$ kJ/mol we previously obtained for n-hexane with the same carbon number.⁴⁹ These results indicate that the free energy calculation performed here is valid. $\Delta G(r)$ decreased almost monotonically for these two solutes. However, Mondal et al. reported that benzene solubilized into SDS is not located at the center of the micelle.⁵⁶ The difference comes from Jacobian of the polar coordinate, $4\pi r^2$. Our distribution function is normalized by the volume of spherical shell, i.e. the density distribution, while the distribution function by Mondal et al. is not normalized, i.e. the number distribution. When we take $4\pi r^2$ into account, a peak is found at $r = 25$ Å as shown in Figure 3.9. Thus, there is no contradiction between our result and that by Mondal et al. Further, excess free energy, $\Delta G(r)$, of benzene into SDS micelle reported by Matubayashi et al.⁵⁴ shows plateau in the hydrophobic region, which is consistent with the present study.

Stable binding site of solute molecules to mixed micelle

$\Delta G(r)$ values for cyclohexane and benzene show a decreasing tendency with decreasing r . This means that these molecules are more stable when transferred to the center of the micelle core. In contrast, for phenol, a minimum values, ΔG_{\min} was observed in the vicinity of the boundary between the hydrophobic core and the hydrophilic shell, and $\Delta G(r)$ significantly increased with decreasing r in the micelle core. It has been reported that phenol is well absorbed by SDS micelles.¹⁰¹ However, location of the phenol molecule is not necessarily at the center of the micelles. It can be adsorption at micellar surface with so called palisade layer structure. In fact, our ΔG function for phenol shows its minimum at the surface.

We have also calculated the radial density distribution, $f(r) = \exp(-\Delta G(r)/RT)$, of phenol and methanol molecules in pure SDS micelle, the latter is from Fujimoto et al.¹⁰² The results are shown in Figure 3.10. The $f(r)$ of phenol shows maximum values at the boundary between hydrophilic and hydrophobic regions (i.e., palisade layer), and it distributes more on the surface of the micelle than methanol. Recent studies also showed that the phenol in the hydrocarbon region of the micelles¹⁰³ and of phospholipid bilayers¹⁰⁴ is unstable, while the most favorable site is the boundary between the hydrophilic and hydrophobic regions for Triton X-100 micelles.

Thus, there is no contradiction between our present results and other experimental and computational studies. Further, in our previous research, for the solubilization of amphiphilic molecules with polar groups such as long-chain alcohol and amine, the minimum $\Delta G(r)$ was also observed at the palisade layer, that is, at the boundary between the hydrophilic and hydrophobic groups of the micelles.¹⁰² These are based on the same mechanism as that of the present case.

On the other hand, as shown in Figures 3.7(a) and (b), a small barrier is observed at around 30 Å from micelle center for $\Delta G(r)$ of phenol in SDS rich micelle. Contribution from the surfactant and water to $\Delta G(r)$ has been analyzed by Date et al.,⁵¹ though the barrier was not found in their calculation. According to their study, the dominant factor of the increase of $\Delta G(r)$ at micelle-water interface is water. A repulsive interaction increases more quickly than that of attractive one at the micelle-water interface when phenol is transferred from the hydrophobic region to the bulk water. They discussed that excluded volume effect which is the largest contribution of repulsive interaction can be found only

for water molecules near phenol, while attractive interactions between water and phenol are found at relatively long distance. Further, a very small barrier was found for the contribution from Na^+ . Thus, the barrier observed in the present study may be attributed to the contributions from water and Na^+ ion.

Surfactant composition dependence of $\Delta G(r)$

The stable distance r that gives the minimum $\Delta G(r)$ for phenol changes with surfactant composition. For the pure SDS micelle, the stable distance $r = 15 \text{ \AA}$. As the C_{12}E_8 content increases, the stable distance gradually increases; for the pure C_{12}E_8 micelle, the stable distance $r = 20 \text{ \AA}$. This is due to a shift of the palisade layer to a larger r value with increasing micelle radius.

Figure 3.11 plots the value of $\Delta G(r)$ near the center of the micelle ($r = 1.0 \text{ \AA}$) where cyclohexane and benzene are stable. As shown in the figure, for these molecules, $\Delta G(r = 1.0 \text{ \AA})$ is almost independent of surfactant composition. The structural change of the hydrophilic group of the mixed micelle occurs at around $r = 20 \text{ \AA}$. It is considered that the solubilization near the center of the micelle is not strongly affected by this structural change. Furthermore, in the vicinity of the micelle center, there is a separation of the distributions of the SDS and C_{12}E_8 dodecyl groups. However, these are the same hydrophobic alkyl chains that form the hydrophobic micelle core, and have the same interactions with solute molecules. Therefore, the influence of the structural change of the micelle core on solubilization is considered to be small.

Figure 3.11 also shows the ΔG ($r = 1.0 \text{ \AA}$) values for phenol. For all compositions, $\Delta G(r)$ reaches 15 kJ/mol, and thus phenol is highly unstable in the center of the mixed micelle. This is considered to be due to the loss of the hydrogen bond of the hydroxyl group by the transfer of phenol to the hydrophobic core. Figure 3.12 shows the proportion of phenol that provides the hydrogen atom of its hydroxyl group to the oxygen atom of the POE group. For all compositions, when phenol is constrained at $r = 1 \text{ \AA}$, the hydroxyl group is rarely hydrogen-bonded to the oxygen atom of the POE group. The ratio of the hydroxyl group of phenol that provides an hydrogen atom to the oxygen atom of the POE group is obviously increased at $r = 10 \text{ \AA}$. This increase is greatest in mixed micelles with high $C_{12}E_8$ content. Therefore, this hydrogen bond is the main driving force that draws phenol molecules to the outside of the micelle core. As a result, the center of micelles is an unstable environment for phenol.

3.4 Conclusions

The equilibrium structures of micelles with six compositions (SDS/ $C_{12}E_8$) and the free energy profile $\Delta G(r)$ of the solubilization of cyclohexane, benzene, and phenol were investigated using MD simulations. Two characteristic structural changes occurred in the mixed micelles. (i) With high SDS content, the POE group captured a Na^+ ion in solution and wrapped around it to form a crown-ether-like complex. (ii) The hydrophobic dodecyl groups of SDS and $C_{12}E_8$ were separately distributed in the mixed micelle core. Despite these structural changes of the micelle, the binding strength of the considered solute

molecules to the micelle did not significantly change. Since these hydrophobic solute molecules were distributed away from the hydrophilic group, they were only slightly affected by it.

When functionality is added to micelles via surfactant mixing, the original micelle characteristics should be retained from an industrial viewpoint. In this sense, the mixture of SDS and C₁₂E₈ considered here is excellent in that the solubilization performance was maintained while the micelles took on the characteristics of the individual surfactants. As shown in this chapter, it is possible to evaluate the solubilization ability of mixed micelles and analyze it at the molecular level using MD simulations. In the future, we will enhance micelle design using MD simulations to add selectivity of solubilization via mixing.

Table 3.1. Aggregation number and number of SDS and C₁₂E₈ molecules prepared for each mixed micelle.

SDS / C ₁₂ E ₈ (mol / mol)	Aggregation Number	Number of molecules	
		SDS	C ₁₂ E ₈
100 / 0	60	60	0
80 / 20	68	54	14
60 / 40	76	46	30
40 / 60	84	34	50
20 / 80	92	18	74
0 / 100	100	0	100

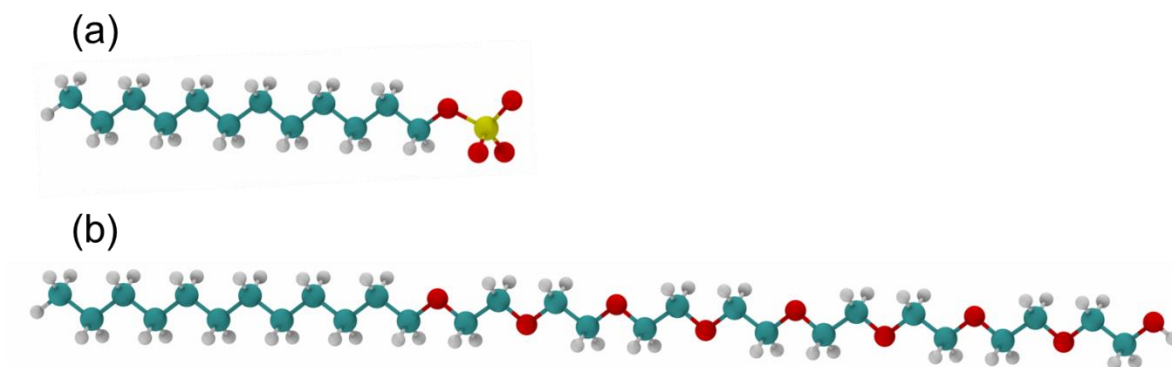


Figure 3.1. Chemical structures of (a) dodecyl sulfate ion in SDS and (b) octaethylene glycol monododecyl ether ($C_{12}E_8$). Gray: hydrogen atoms, cyan: carbon atoms, red: oxygen atoms, and yellow: sulfur atom.

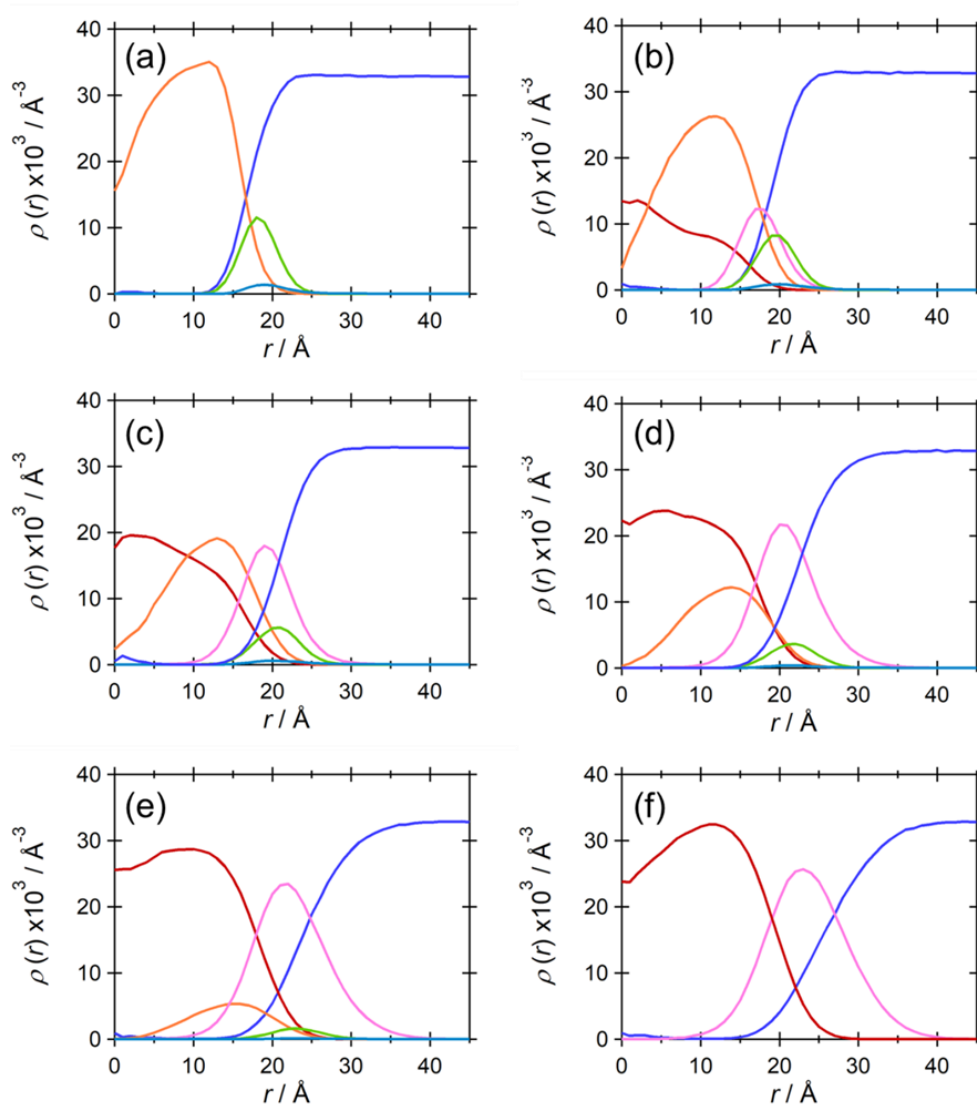


Figure 3.2. Radial density profile, $\rho(r)$, of mixed micelles consisting of SDS and C₁₂E₈ for SDS/C₁₂E₈ ratios of (a) 100/0, (b) 80/20, (c) 60/40, (d) 40/60, (e) 20/80, and (f) 0/100. Red: carbon atoms in alkyl chain of C₁₂E₈, pink: carbon and oxygen atoms in POE group of C₁₂E₈, orange: carbon atoms in alkyl chain of DS ion, green: sulfur and oxygen atoms in sulfate group of DS ion, cyan: Na⁺ ion, and blue: oxygen atom in water molecule.

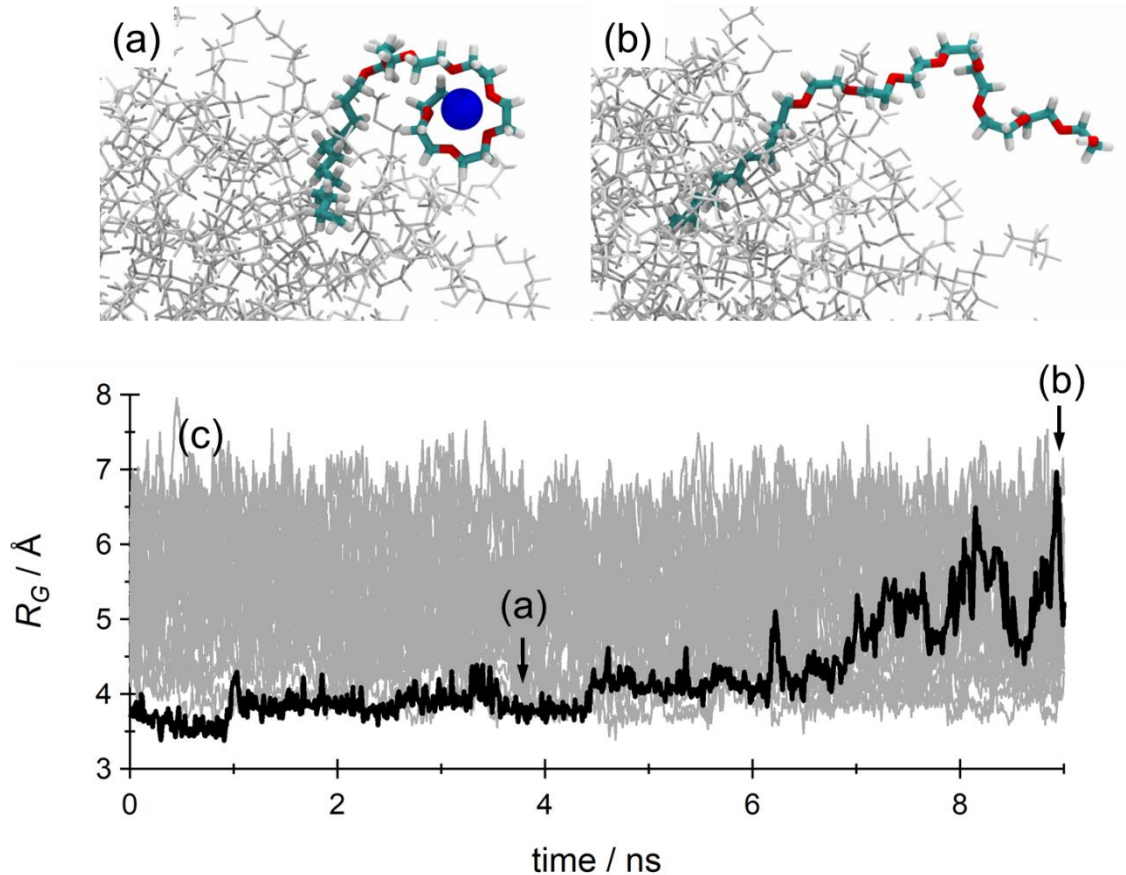


Figure 3.3. Typical MD snapshot of $C_{12}E_8$ in a mixed micelle system (SDS/ $C_{12}E_8 = 60/40$). (a) POE group capturing a Na^+ ion, (b) unfolded POE group after releasing the Na^+ ion, and (c) time evolution of the radius of gyration, R_G , of the POE group. Black arrows indicate the times corresponding to (a) and (b). In Figures (a) and (b), gray: hydrogen atoms, cyan: carbon atoms, red: oxygen atoms, blue sphere: Na^+ ion, and gray wires: other surfactant molecules. In Figure (c), typical single POE group shown in Figures (a) and (b) was highlighted by black line, and that for the other 29 molecules in the mixed micelle were shown by gray lines.

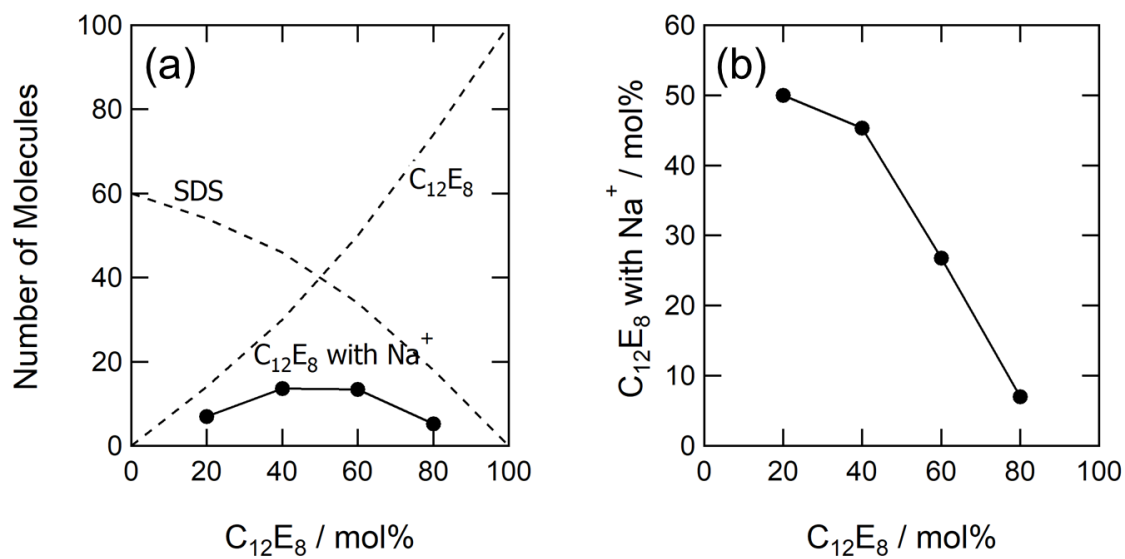


Figure 3.4. (a) Number of C₁₂E₈ molecules capturing Na⁺ ions via the POE group, (b) molar fraction of C₁₂E₈ capturing Na⁺ ions. In Figure (a), black dashed lines indicate the total number of SDS and C₁₂E₈ molecules in each composition.

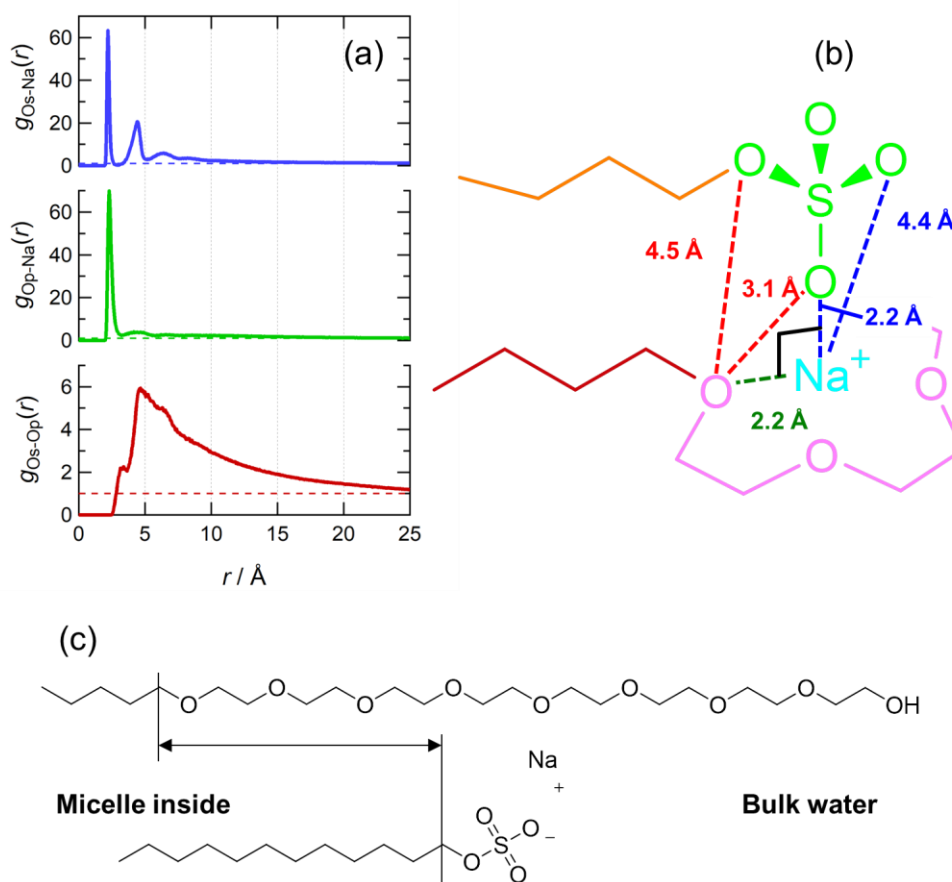


Figure 3.5. (a) The calculated radial distribution functions, $g(r)$, for oxygen atom of SDS (O_s)- Na^+ ion, oxygen atoms of C_{12}E_8 (O_p)- Na^+ , and $\text{O}_s\text{-O}_p$ for a mixed micelle system (SDS/ $\text{C}_{12}\text{E}_8 = 60/40$). $g_{\text{O}_s\text{-Na}}(r)$ and $g_{\text{O}_p\text{-Na}}(r)$ are shifted for clarity. (b) A schematic drawing for the bridging geometry between hydrophilic POE and sulfate groups by the Na^+ ion. (c) A schematic drawing for the location difference of hydrophobic group between SDS and C_{12}E_8 . In Figures (a), each dashed line indicate $g(r) = 1$.

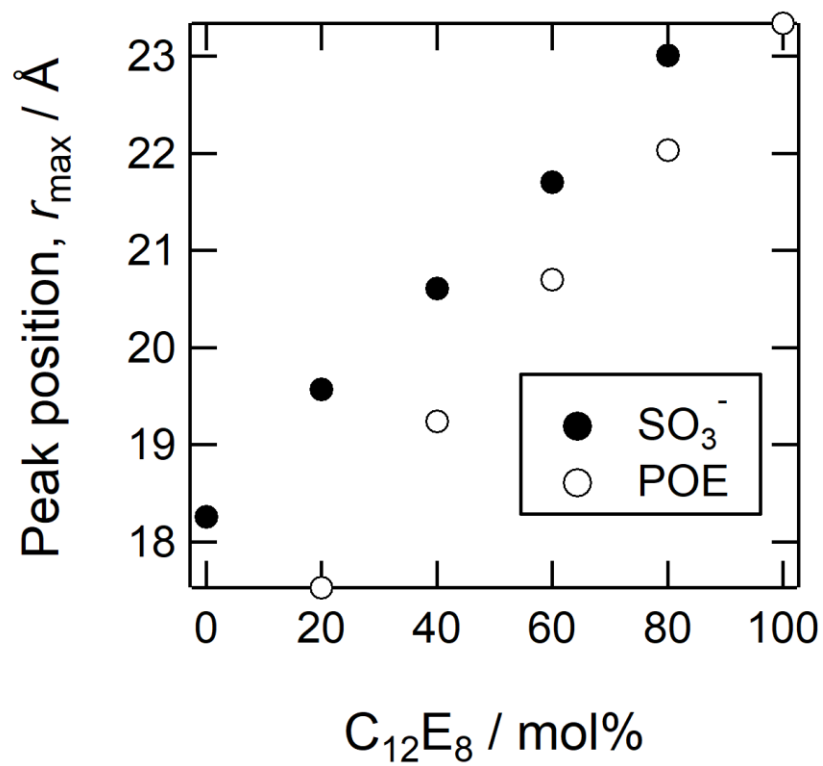


Figure 3.6. Peak positions of the calculated number density profile, r_{\max} , of sulfate group (SO_3^-) in SDS and POE group in C_{12}E_8 for several SDS/ C_{12}E_8 compositions evaluated from Figures 3.2(a)-(f).

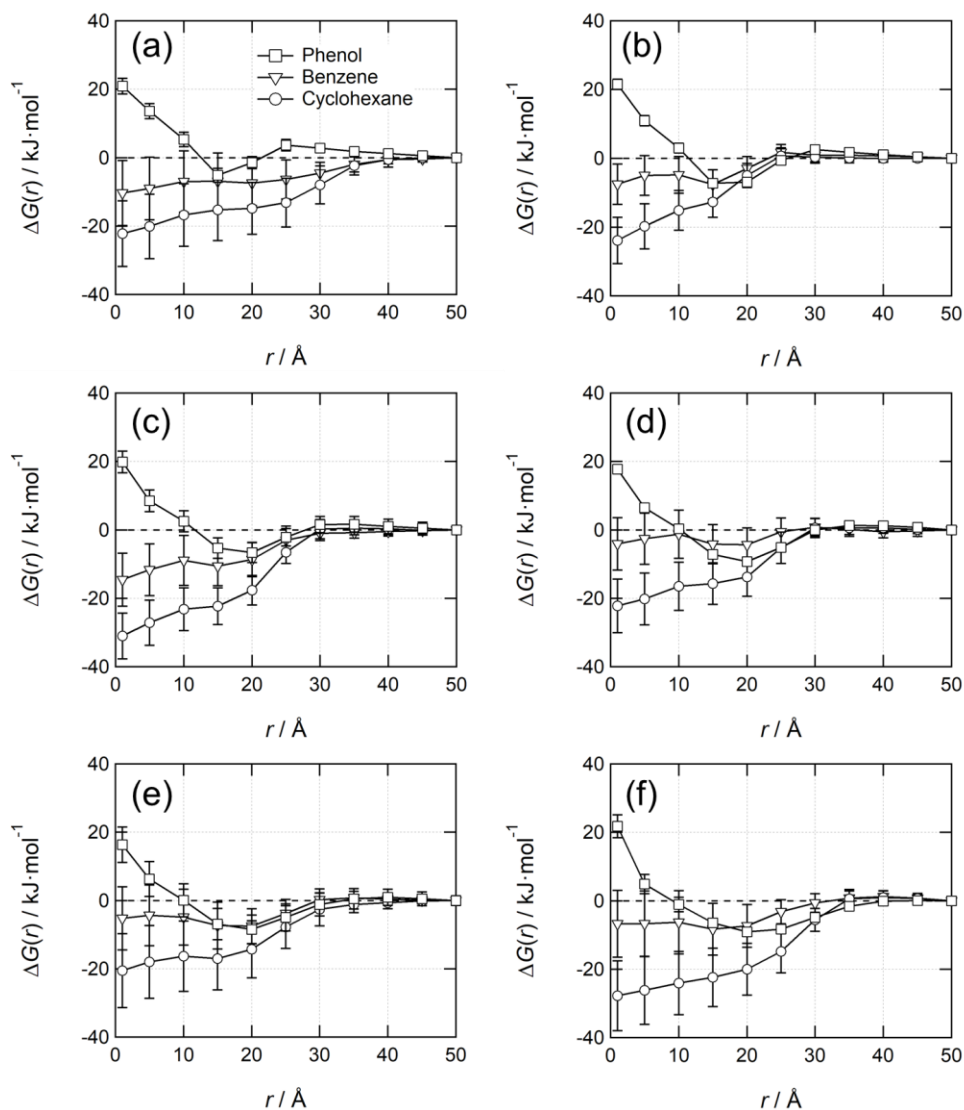


Figure 3.7. Free energy profile, $\Delta G(r)$, of solubilization of cyclohexane (circle), benzene (triangle), and phenol (square) from the bulk water phase to the center of mass of the micelle for SDS/C₁₂E₈ ratios of (a) 100/0, (b) 80/20, (c) 60/40, (d) 40/60, (e) 20/80, and (f) 0/100. Since statistics for phenol is ten times larger than cyclohexane and benzene, errors for the former is much smaller than the latter two.



Figure 3.8. Trajectories of center of mass of phenol molecule constrained at $r = 20 \text{ \AA}$ from micelle center of SDS/C₁₂E₈=40/60 plotted every 100 ps for total 100 ns MD simulations.

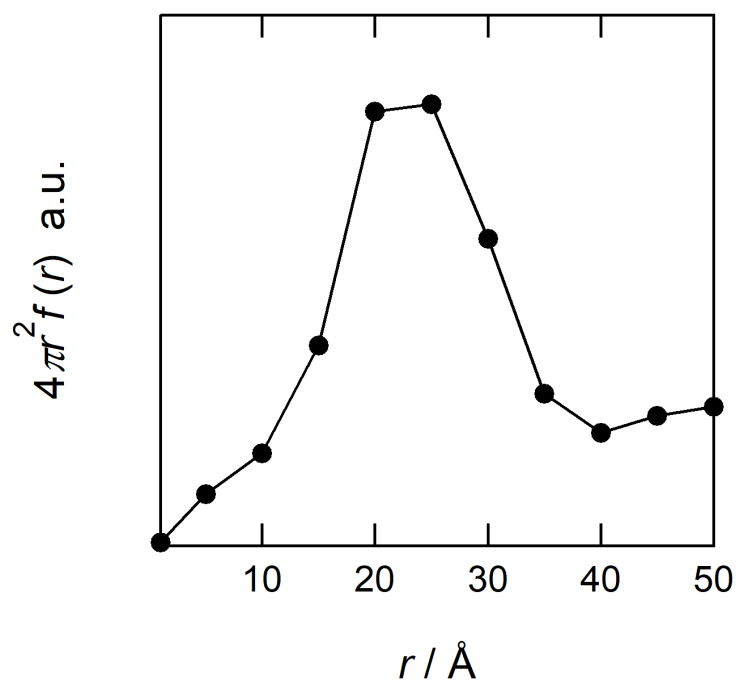


Figure 3.9. The calculated number distribution, $4\pi r^2 f(r)$, of benzene molecules in pure SDS micelle.

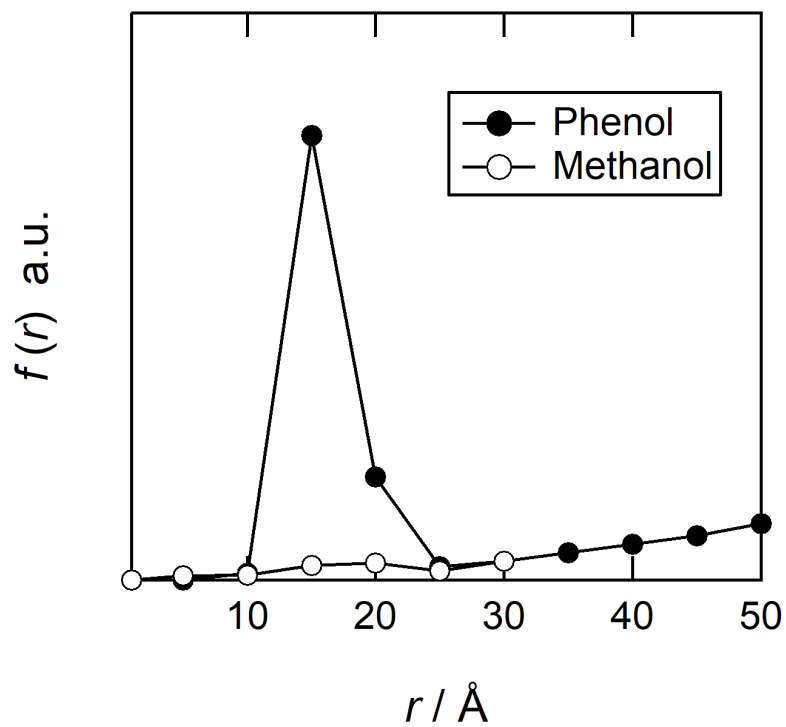


Figure 3.10. The calculated density distribution, $f(r) = \exp(-\Delta G(r)/RT)$, of phenol and methanol in pure SDS micelle. The $f(r)$ of methanol is from [Fujimoto et al.](#)¹⁰².

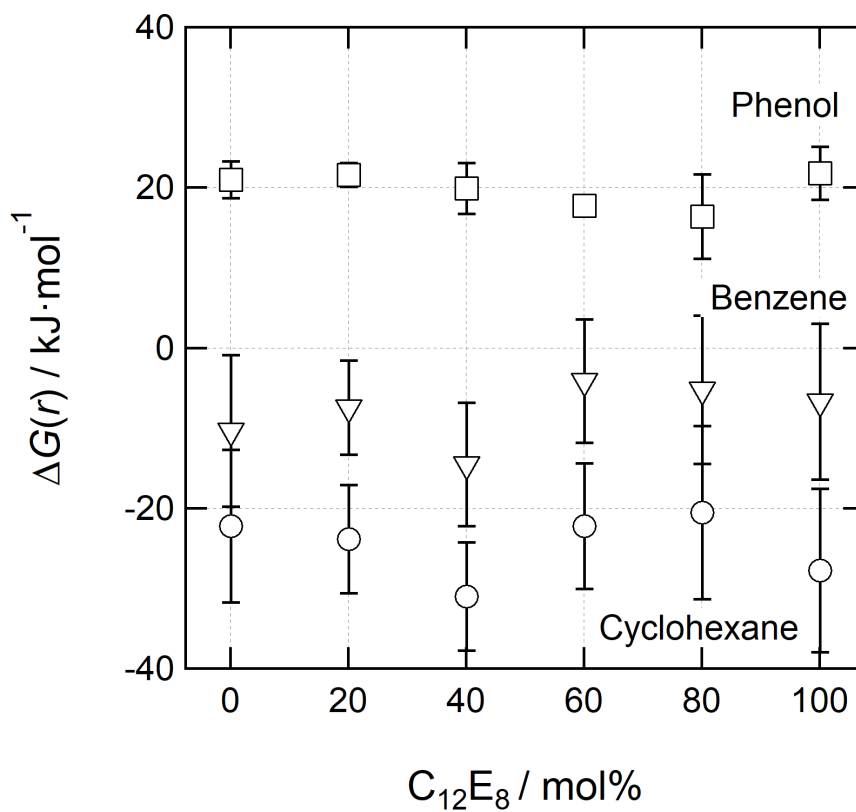


Figure 3.11. Free energy, $\Delta G(r)$, of cyclohexane (circle), benzene (triangle), and phenol (square) at $r = 1.0 \text{ \AA}$ for SDS/ $C_{12}E_8$ mixed micelles. Since statistics for phenol is ten times larger than cyclohexane and benzene, errors for the former is much smaller than the latter two.

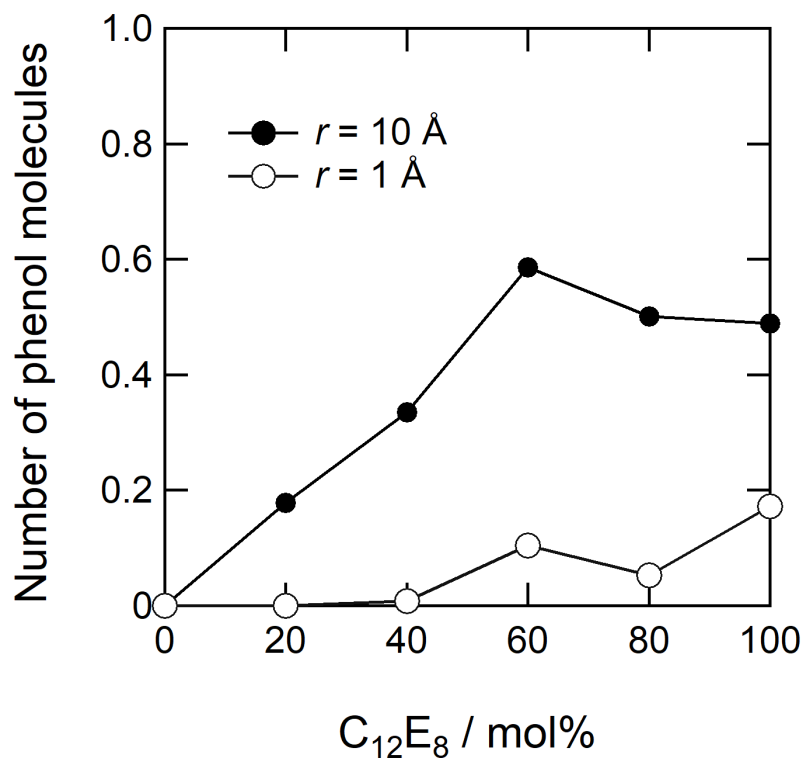


Figure 3.12. Number of phenol molecules providing the hydroxyl hydrogen atom to the POE group. Open circle: phenol is fixed at $r = 1.0 \text{ \AA}$. Solid circle: phenol is fixed at $r = 10 \text{ \AA}$.

Conclusion

Molecular dynamics (MD) simulations have been used to clarify detailed structure and molecular behaviors of hydrated crystal (L_c) and mixed micelles of surfactants that commonly used in industrial applications. In this dissertation, I have investigated the following topics particularly; (1) Structural formation of low-water content lamellae composed of alkylbenzene sulfonate (LAS), and (2) Solubilization by mixed micelles of sodium dodecyl sulfate (SDS) and octaethyleneglycol monododecyl ether ($C_{12}E_8$).

In Chapter 1, we first identified the L_c structure of LAS at ambient temperature by combining X-ray diffraction (XRD) with all-atom MD simulation. It is known that the L_c phase only a stoichiometrically small number of water molecules, and the number of water molecules located in the inter-lamellar layers may change when the system shows the thermally induced phase transition. Therefore, we explored possible crystal structures with five different hydration levels of 0, $\frac{1}{2}$, 1, 2, and 4 water per LAS using MD method which are compared with the d -spacing measured by XRD. Among them, only the diffraction pattern calculated for the monohydrate well explain the experimental diffraction pattern at 300 K. A structural change of the monohydrate from the L_c phase to the tilted gel ($L_{\beta'}$) phase was also observed by heating from 300 to 360 K in the MD simulations, where a cross-sectional structure of the alkyl groups of LAS molecules changed from a face-centered rectangular lattice to a hexagonal one. Further heating to 400 K resulted in a disordered liquid crystals (L_a) phase. Thus, change in configuration of LAS during

thermally induced phase transitions was well explored and characterized by the MD simulations with the aid of the XRD data.

In Chapter 2, we investigated the translational and conformational dynamics of LAS molecules in the L_c , $L_{\beta'}$, and L_α phases. In the L_α phase, the lateral diffusion of LAS is as fast as that of phospholipids in the L_α phase. The self-diffusion coefficient was undetectably small in the L_c and $L_{\beta'}$ phases. The conformation of LAS in the L_α phase relaxes very rapidly (~ 20 ps), whereas those in the L_c and $L_{\beta'}$ phases relax very slowly (\sim more than 50 ns). The time scale of the relaxations greatly depends on the segment of the LAS molecule in the latter two phases. The relaxation time for the SO_3^- head group and benzene ring was much longer than that for alkyl chains. Conformational pattern analyses of LAS alkyl chains revealed that high fraction of the *gauche* conformation for the odd-numbered C-C bonds aligns the chain parallel to the bilayer normal and is the main origin of the different relaxation time for the different segments in the chain. In the L_c , $L_{\beta'}$, and L_α phases, orientation of the SO_3^- group and the benzene ring is locked by the salt bridge among SO_3^- groups and sodium ions and by the steric hindrance by the alkyl chains, respectively. As a result, the orientational order found for the C-C bonds in the LAS alkyl chains is kept even in the L_α phase. This means that phase transition temperature of the lamellae can be controlled by limiting the conformational change of the alkyl chain.

In Chapter 3, MD simulations were performed for mixed micelles composed of SDS and C_{12}E_8 with six compositions ($\text{SDS}/\text{C}_{12}\text{E}_8 = 100/0, 80/20, 60/40, 40/60, 20/80,$ and $0/100$) to investigate the composition dependence of the mixed micelle structure and solubilization of cyclohexane, benzene, and phenol molecules by the micelles. The radial

density distribution of the hydrophilic polyoxyethylene (POE) group of C₁₂E₈ is very sharp for micelles with high SDS content because the POE group captures a Na⁺ ion in solution and wraps around it to form a compact crown-ether-like complex. The hydrophobic dodecyl groups of SDS and C₁₂E₈ were separately distributed in the mixed micelle core. $\Delta G(r)$ evaluated for each solute showed that despite the structural changes of the micelle the binding strength of the solute molecules to the micelle did not change significantly.

Throughout the present study, a few important findings for the development of detergents were obtained. In the studies on lamellar structure of LAS, we found that specific interaction and molecular topology such as salt bridge of inter-lamellar and steric hindrance of benzene ring, respectively, in the L_c phase are the main cause of the precipitation. Therefore, in order to develop high performance detergent with long term stability even at low temperatures, surfactant molecule which enhances the mobility of the hydrophilic group can be proposed as a candidate. From the solubilization study of the mixed micelles, no mixing ratio dependence was found for the solubilization free energy, $\Delta G(r)$, for the present three C₆ cyclic substances. It is presumed that the C₆ cyclic solutes are so small that the difference in the micelle structure does not affect much on the free energy. However, in the case of lipids and proteins with large molecular weight, the free energy of solubilization may be sensitive to the composition. Further, with respect to phenol, the number of hydrogen bonds between hydroxyl group of the phenol and the POE group depends much on the mixing ratio of the surfactants. The findings are all useful for the design of the surfactants for the solubilization.

References

- (1) Lee, A.; Seo, M. H.; Yang, S.; Koh, J.; Kim, H. The Effects of Mechanical Actions on Washing Efficiency. *Fibers Polym.* **2008**, *9* (1), 101–106.
- (2) Garrett, P. R. *Defoaming : Theory and Industrial Applications*; M. Dekker, 1993.
- (3) Pugh, R. J. Foaming, Foam Films, Antifoaming and Defoaming. *Adv. Colloid Interface Sci.* **1996**, *64*, 67–142.
- (4) Lim, S.-H.; Hudson, S. M. Application of a Fiber-Reactive Chitosan Derivative to Cotton Fabric as an Antimicrobial Textile Finish. *Carbohydr. Polym.* **2004**, *56* (2), 227–234.
- (5) Bhat, R.; Prajna, P. S.; Menezes, V. P.; Shetty, P. Antimicrobial Activities of Soap and Detergents. *Adv. Biores* **2011**, *2* (2), 52–62.
- (6) Drozd, J. C.; Desai, D. D. Liquid Laundry Detergents Based on Soap and α -Sulfo Methyl Esters. *J. Am. Oil Chem. Soc.* **1991**, *68* (1), 59–62.
- (7) Kékicheff, P.; Madelmont, C. G.; Ollivon, M. Phase Diagram of Sodium Dodecyl Sulfate-Water System: 1. A Calorimetric Study. *J. Colloid Interface Sci.* **1988**, *131* (1), 112–132.
- (8) Rosen, M. J.; Kunjappu, J. T. *Surfactants and Interfacial Phenomena*; John Wiley & Sons, 2012.
- (9) Laughlin, R. G. *The Aqueous Phase Behavior of Surfactants*; Academic Pr, 1994; Vol. 6.

- (10) Tanford, C. *The Hydrophobic Effect: Formation of Micelles and Biological Membranes 2d Ed*; J. Wiley., 1980.
- (11) Bera, A.; Ojha, K.; Mandal, A. Synergistic Effect of Mixed Surfactant Systems on Foam Behavior and Surface Tension. *J. Surfact. Deterg.* **2013**, *16*, 621–630.
- (12) Coiro, V. M.; Manigrasso, M.; Mazza, F.; Pochetti, G. Structure of a Triclinic Phase of Sodium Dodecyl Sulfate Monohydrate. A Comparison with Other Sodium Dodecyl Sulfate Crystal Phases. *Acta Crystallogr. Sect. C Cryst. Struct. Commun.* **1987**, *C43*, 850–854.
- (13) Coiro, V. M.; Mazza, F.; Pochetti, G. Crystal Phases Obtained from Aqueous Solutions of Sodium Dodecyl Sulfate. The Structure of a Monoclinic Phase of Sodium Dodecyl Sulfate Hemihydrate. *Acta Crystallogr. Sect. C Cryst. Struct. Commun.* **1986**, *C42*, 991–995.
- (14) Sundell, S. Crystal-Structure of Sodium Dodecylsulfate. *ACTA Chem. Scand. Ser. A-PHYSICAL Inorg. Chem.* **1977**, *31* (10), 799–807.
- (15) Smith, L. A.; Hammond, R. B.; Roberts, K. J.; Machin, D.; McLeod, G. Determination of the Crystal Structure of Anhydrous Sodium Dodecyl Sulphate Using a Combination of Synchrotron Radiation Powder Diffraction and Molecular Modelling Techniques. *J. Mol. Struct.* **2000**, *554* (2–3), 173–182.
- (16) Abe, Y.; Harata, K.; Fujiwara, M.; Ohbu, K. Intercalation of Cations in Crystalline Anionic Surfactants. *J. Chem. Soc. Perkin Trans. 2* **1999**, 85–98.

- (17) Abe, Y.; Harata, K.; Fujiwara, M.; Ohbu, K. Bilayer Structure of Glycolipid Crystals. Thermal Stability of the Crystal and State of the Alkyl Chain. *J. Chem. Soc. Perkin Trans. 2* **1998**, No. 1, 177–186.
- (18) Abe, Y.; Fujiwara, M.; Ohbu, K.; Harata, K. Crystal Structures of Methyl 6-O-Acyl- α -d-Galactopyranosides. *Carbohydr. Res.* **1995**, 275 (1), 9–16.
- (19) Abe, Y.; Harata, K.; Fujiwara, M.; Ohbu, K. Crystal Structures of Methyl 6-O-n-Alkanoyl- β -d-Glucopyranosides. *Carbohydr. Res.* **1995**, 269 (1), 43–51.
- (20) Abe, Y.; Harata, K.; Fujiwara, M.; Ohbu, K. Molecular Arrangement and Intermolecular Hydrogen Bonding in Crystals of Methyl 6-O-Acyl-d-Glucopyranosides. *Langmuir* **1996**, 12 (3), 636–640.
- (21) Moews, P. C.; Knox, J. R. The Crystal Structure of 1-Decyl. Alpha.-D-Glucopyranoside: A Polar Bilayer with a Hydrocarbon Subcell. *J. Am. Chem. Soc.* **1976**, 98 (21), 6628–6633.
- (22) Jeffrey, G. A.; Yeon, Y.; Abola, J. The Crystal Structures of Octyl α -D-Glucopyranoside Monohydrate and Hemihydrate: Mesogenic Structures with Interdigitizing Alkyl Chains. *Carbohydr. Res.* **1987**, 169, 1–11.
- (23) Zabel, V.; Müller-Farnow, A.; Hilgenfeld, R.; Saenger, W.; Pfannemüller, B.; Enkelmann, V.; Welte, W. Amphiphilic Properties of Synthetic Glycolipids Based on Amide Linkages. II. Crystal and Molecular Structure of N-(n-Octyl)-D-Gluconamide, an Amphiphilic Molecule in Head-to-Tail Packing Mode. *Chem. Phys. Lipids* **1986**, 39 (4), 313–327.

- (24) Lomer, T. R.; IUCr. The Crystal and Molecular Structure of Lauric Acid (Form A). *Acta Crystallogr.* **1963**, *16* (10), 984–988.
- (25) Goto, M.; Asada, E. The Crystal Structure of the B-Form of Stearic Acid. *Bull. Chem. Soc. Jpn.* **1978**, *51* (9), 2456–2459.
- (26) Pearson, R. H.; Pascher, I. The Molecular Structure of Lecithin Dihydrate. *Nature* **1979**, *281* (5731), 499–501.
- (27) Rietveld, H. M. Line Profiles of Neutron Powder-Diffraction Peaks for Structure Refinement. *Acta Crystallogr.* **1967**, *22* (1), 151–152.
- (28) Horta, B. A. C.; De Vries, A. H.; Hünenberger, P. H. Simulating the Transition between Gel and Liquid-Crystal Phases of Lipid Bilayers: Dependence of the Transition Temperature on the Hydration Level. *J. Chem. Theory Comput.* **2010**, *6* (8), 2488–2500.
- (29) Lombardo, G. M.; Pappalardo, G. C.; Punzo, F.; Costantino, F.; Costantino, U. A Novel Integrated X-Ray Powder Diffraction (XRPD) and Molecular Dynamics (MD) Approach for Modelling Mixed-Metal (Zn, Al)-Layered Double Hydroxides (LDHs). *Eur. J. Inorg. Chem.* **2005**, No. 24, 5026–5034.
- (30) Nishiyama, Y.; Johnson, G. P.; French, A. D. Diffraction from Nonperiodic Models of Cellulose Crystals. *Cellulose* **2012**, *19* (2), 319–336.
- (31) Coiro, V. M.; Mazza, F. Crystal Phases of Dodecyl Sulfates Obtained from Aqueous Solutions: Structure of the Rubidium Salt. *Acta Crystallogr. Sect. C Cryst. Struct. Commun.* **1989**, *C45*, 1132–1136.

- (32) Coiro, V. M.; Mazza, F. Crystal Phases of Dodecyl Sulfates Obtained from Aqueous Solutions: Structure of the Hexaaquamagnesium Salt. *Acta Crystallogr. Sect. C Cryst. Struct. Commun.* **1991**, *C47*, 1169–1173.
- (33) Kawai, T.; Umemura, J.; Takenaka, T.; Kodama, M.; Ogawa, Y.; Seki, S. Polarized Fourier Transform Infrared Spectra and Molecular Orientation of a Water-Dioctadecyldimethylammonium Chloride System in the Coagel and Gel Phases. *Langmuir* **1986**, *2* (6), 739–743.
- (34) Hauser, H.; Pascher, I.; Pearson, R. H.; Sundell, S. Preferred Conformation and Molecular Packing of Phosphatidylethanolamine and Phosphatidylcholine. *Biochim. Biophys. Acta - Rev. Biomembr.* **1981**, *650* (1), 21–51.
- (35) Tu, K.; Tobias, D. J.; Blasie, J. K.; Klein, M. L. Molecular Dynamics Investigation of the Structure of a Fully Hydrated Gel-Phase Dipalmitoylphosphatidylcholine Bilayer. *Biophys. J.* **1996**, *70* (2), 595–608.
- (36) Seddon, J. M.; Cevc, G. *Lipid Polymorphism: Structure and Stability of Lyotropic Mesophases of Phospholipids*; Marcel Dekker, Inc: New York, NY, USA, 1993.
- (37) Chernik, G. G. Phase Studies of Surfactant-Water Systems. *Curr. Opin. Colloid Interface Sci.* **1999**, *4* (6), 381–390.
- (38) Sperline, R. P. Infrared Spectroscopic Study of the Crystalline Phases of Sodium Dodecyl Sulfate. *Langmuir* **1997**, *13*, 3715–3726.
- (39) Sperline, R. P.; Song, Y.; Freiser, H. Fourier Transform Infrared Attenuated Total Reflection Spectroscopy Linear Dichroism Study of Sodium Dodecyl Sulfate

- Adsorption at the Al_2O_3 /Water Interface Using Al_2O_3 -Coated Optics. *Langmuir* **1992**, 8, 2183–2191.
- (40) Sperline, R. P.; Song, Y.; Freiser, H. Temperature Dependent Structure of Adsorbed Sodium Dodecyl Sulfate at the Al_2O_3 /Water Interface. *Langmuir* **1997**, 13, 3727–3732.
- (41) Sperline, R. P.; Song, Y.; Freiser, H. Fourier Transform Infrared Attenuated Total Reflection Linear Dichroism Study of Sodium Dodecylbenzenesulfonate Adsorption at the Alumina/Water Interface Using Al_2O_3 -Coated Optics. *Langmuir* **1994**, 10 (1), 37–44.
- (42) Sperline, R. P.; Song, Y. Temperature Independent Adsorbate Structure of 4-Octyl-, 4-Decyl-, and 4-Dodecylbenzenesulfonates at the Al_2O_3 / Water Interface. *Langmuir* **1997**, 13, 6985–6994.
- (43) Hua, X. Y.; Rosen, M. J. Synergism in Binary Mixtures of Surfactants: I. Theoretical Analysis. *J. Colloid Interface Sci.* **1982**, 90 (1), 212–219.
- (44) Rosen, M. J.; Zhao, F. Binary Mixtures of Surfactants. The Effect of Structural and Microenvironmental Factors on Molecular Interaction at the Aqueous Solution/Air Interface. *J. Colloid Interface Sci.* **1983**, 95 (2), 443–452.
- (45) Carey, M. C.; Small, D. M. The Characteristics of Mixed Micellar Solutions with Particular Reference to Bile. *Am. J. Med.* **1970**, 49 (5), 590–608.
- (46) Hammad, M. .; Müller, B. . Increasing Drug Solubility by Means of Bile Salt–phosphatidylcholine-Based Mixed Micelles. *Eur. J. Pharm. Biopharm.* **1998**, 46 (3), 361–367.

- (47) Karaborni, S.; Van Os, N. M.; Esselink, K.; Hilbers, P. A. J. Molecular Dynamics Simulations of Oil Solubilization in Surfactant Solutions. *Langmuir* **1993**, *9* (5), 1175–1178.
- (48) Fujimoto, K.; Yoshii, N.; Okazaki, S. Enthalpy and Entropy of Transfer of Alkanes from Water Phase to the Micelle Core. *Mol. Simul.* **2012**, *38* (5), 342–345.
- (49) Fujimoto, K.; Yoshii, N.; Okazaki, S. Molecular Dynamics Study of Solubilization of Immiscible Solutes by a Micelle: Free Energy of Transfer of Alkanes from Water to the Micelle Core by Thermodynamic Integration Method. *J. Chem. Phys.* **2010**, *133*, 074511.
- (50) Storm, S.; Jakobtorweihen, S.; Smirnova, I. Solubilization in Mixed Micelles Studied by Molecular Dynamics Simulations and COSMOmic. *J. Phys. Chem. B* **2014**, *118*, 3593–3604.
- (51) Date, A.; Ishizuka, R.; Matubayasi, N. Energetics of Nonpolar and Polar Compounds in Cationic, Anionic, and Nonionic Micelles Studied by All-Atom Molecular Dynamics Simulation Combined with a Theory of Solutions. *Phys. Chem. Chem. Phys.* **2016**, *18* (19), 13223–13231.
- (52) Garde, S.; Yang, L.; Dordick, J. S.; Paulaitis, M. E. Molecular Dynamics Simulation of C8E5 Micelle in Explicit Water: Structure and Hydrophobic Solvation Thermodynamics. *Mol. Phys.* **2002**, *100* (14), 2299–2306.
- (53) Kuhn, H.; Breitzke, B.; Rehage, H. A Molecular Modeling Study of Pentanol Solubilized in a Sodium Octanoate Micelle. *J. Colloid Interface Sci.* **2002**, *249* (1), 152–161.

- (54) Matubayasi, N.; Liang, K. K.; Nakahara, M. Free-Energy Analysis of Solubilization in Micelle. *J. Chem. Phys.* **2006**, *124* (15), 154908.
- (55) Yan, H.; Cui, P.; Liu, C.-B.; Yuan, S.-L. Molecular Dynamics Simulation of Pyrene Solubilized in a Sodium Dodecyl Sulfate Micelle. *Langmuir* **2012**, *28* (11), 4931–4938.
- (56) Mondal, S.; Ghosh, S.; De, S. Atomistic Level Molecular Dynamics Simulation on the Solubilization Mechanism of Aromatic Molecules in Anionic Micelles. *RSC Adv.* **2015**, *5* (126), 104493–104501.
- (57) Yordanova, D.; Ritter, E.; Gerlach, T.; Jensen, J. H.; Smirnova, I.; Jakobtorweihen, S. Solute Partitioning in Micelles: Combining Molecular Dynamics Simulations, COSMOMic, and Experiments. *J. Phys. Chem. B* **2017**, *121* (23), 5794–5809.
- (58) Ingram, T.; Storm, S.; Kloss, L.; Mehling, T.; Jakobtorweihen, S.; Smirnova, I. Prediction of Micelle/Water and Liposome/Water Partition Coefficients Based on Molecular Dynamics Simulations, COSMO-RS, and COSMOmic. *Langmuir* **2013**, *29* (11), 3527–3537.
- (59) Alexandridis, P.; Olsson, U.; Lindman, B. A Record Nine Different Phases (Four Cubic, Two Hexagonal, and One Lamellar Lyotropic Liquid Crystalline and Two Micellar Solutions) in a Ternary Isothermal System of an Amphiphilic Block Copolymer and Selective Solvents (Water and Oil). *Langmuir* **2002**, *14* (10), 2627–2638.

- (60) Gray, F. W.; Gerecht, J. F.; Krems, I. J. The Preparation of Model Long Chain Alkylbenzenes and a Study of Their Isomeric Sulfonation Products. *J. Org. Chem.* **1955**, *20* (4), 511–524.
- (61) Ma, J. G.; Boyd, B. J.; Drummond, C. J. Positional Isomers of Linear Sodium Dodecyl Benzene Sulfonate: Solubility, Self-Assembly, and Air/Water Interfacial Activity. *Langmuir* **2006**, *22* (21), 8646–8654.
- (62) Press, W. H. *Numerical Recipes 3rd Edition: The Art of Scientific Computing*; 2007.
- (63) Hoover, W. G. Canonical Dynamics: Equilibrium Phase-Space Distributions. *Phys. Rev. A* **1985**, *31* (3), 1695–1697.
- (64) Parrinello, M.; Rahman, A. Crystal Structure and Pair Potentials: A Molecular-Dynamics Study. *Phys. Rev. Lett.* **1980**, *45* (14), 1196–1199.
- (65) Hess, B.; Bekker, H.; Berendsen, H. J. C.; Fraaije, J. G. E. M. LINCS: A Linear Constraint Solver for Molecular Simulations. *J. Comput. Chem.* **1997**, *18* (12), 1463–1472.
- (66) Jorgensen, W. L.; Chandrasekhar, J.; Madura, J. D.; Impey, R. W.; Klein, M. L. Comparison of Simple Potential Functions for Simulating Liquid Water. *J. Chem. Phys.* **1983**, *79* (2), 926–935.
- (67) Klauda, J. B.; Brooks, B. R.; Mackerell, A. D.; Venable, R. M.; Pastor, R. W. An Ab Initio Study on the Torsional Surface of Alkanes and Its Effect on Molecular Simulations of Alkanes and a DPPC Bilayer. *J. Phys. Chem. B* **2005**, *109*, 5300–5311.

- (68) He, X.; Guvench, O.; MacKerell, A. D.; Klein, M. L. Atomistic Simulation Study of Linear Alkylbenzene Sulfonates at the Water/Air Interface. *J. Phys. Chem. B* **2010**, *114* (30), 9787–9794.
- (69) Essmann, U.; Perera, L.; Berkowitz, M. L.; Darden, T.; Lee, H.; Pedersen, L. G. A Smooth Particle Mesh Ewald Method. *J. Chem. Phys.* **1995**, *103* (19), 8577–8593.
- (70) Abraham, M. J.; Murtola, T.; Schulz, R.; Páll, S.; Smith, J. C.; Hess, B.; Lindahl, E. GROMACS: High Performance Molecular Simulations through Multi-Level Parallelism from Laptops to Supercomputers. *SoftwareX* **2015**, *1–2*, 19–25.
- (71) Macrae, C. F.; Edgington, P. R.; McCabe, P.; Pidcock, E.; Shields, G. P.; Taylor, R.; Towler, M.; Van De Streek, J. Mercury: Visualization and Analysis of Crystal Structures. *J. Appl. Crystallogr.* **2006**, *39* (3), 453–457.
- (72) Giacovazzo, C.; Monaco, H. L.; Artioli, G.; Viterbo, D.; Ferraris, G.; Giacovazzo, C.; Scordari, F.; Gilli, G.; Zanotti, G.; Catti, M. *Fundamentals of Crystallography*; Oxford University Press Oxford, 2002; Vol. 7.
- (73) Iwata, T. Stabilization of Emulsion by α -Gel. *Pharm. Tech. Japan* **2017**, *33.1*, 75–82.
- (74) Miller, R. M.; Poulos, A. S.; Robles, E. S. J.; Brooks, N. J.; Ces, O.; Cabral, J. T. Isothermal Crystallization Kinetics of Sodium Dodecyl Sulfate-Water Micellar Solutions. *Cryst. Growth Des.* **2016**, *16* (6), 3379–3388.
- (75) Mathevet, F.; Masson, P.; Skoulios, A. Smectic Liquid Crystals from Supramolecular Guanidinium Alkylbenzenesulfonates. *Liq. Cryst.* **2002**, *8* (10), 2248–2254.

- (76) Klauda, J. B.; Brooks, B. R.; Pastor, R. W. Dynamical Motions of Lipids and a Finite Size Effect in Simulations of Bilayers. *J. Chem. Phys.* **2006**, *125* (14), 144710.
- (77) Roark, M.; Feller, S. E. Molecular Dynamics Simulation Study of Correlated Motions in Phospholipid Bilayer Membranes. *J. Phys. Chem. B* **2009**, *113*, 13229–13234.
- (78) Fahey, P. F.; Webb, W. W. Lateral Diffusion in Phospholipid Bilayer Membranes and Multilamellar Liquid Crystals. *Biochemistry* **1978**, *17* (15), 3046–3053.
- (79) Wu, E.; Jacobson, K.; Papahadjopoulos, D.; En-Shinn, W.; Jacobson, K.; Papahadjopoulos, D. Lateral Diffusion in Phospholipid Multibilayers Measured by Fluorescence Recovery after Photobleaching. *Biochemistry* **1977**, *16* (17), 3936–3941.
- (80) Filippov, A.; Orädd, G.; Lindblom, G. The Effect of Cholesterol on the Lateral Diffusion of Phospholipids in Oriented Bilayers. *Biophys. J.* **2003**, *84* (5), 3079–3086.
- (81) Seelig, A.; Seelig, J. Dynamic Structure of Fatty Acyl Chains in a Phospholipid Bilayer Measured by Deuterium Magnetic Resonance. *Biochemistry* **1974**, *13* (23), 4839–4845.
- (82) Senak, L.; Davies, M. A.; Mendelsohn, R. A Quantitative IR Study of Hydrocarbon Chain Conformation in Alkanes and Phospholipids: CH₂ Wagging Modes in Disordered Bilayer and HII Phases. *J. Phys. Chem.* **1991**, *95* (6), 2565–2571.

- (83) Turro, N. J.; Yekta, A. Luminescent Probes for Detergent Solutions. A Simple Procedure for Determination of the Mean Aggregation Number of Micelles. *J. Am. Chem. Soc.* **1978**, *100* (18), 5951–5952.
- (84) Corazza, M.; Lauriola, M.; Zappaterra, M.; Bianchi, A.; Virgili, A. Surfactants, Skin Cleansing Protagonists. *J. Eur. Acad. Dermatology Venereol.* **2010**, *24* (1), 1–6.
- (85) Effendy, I.; Maibach, H. I. Detergent and Skin Irritation. *Clin. Dermatol.* **1996**, *14* (1), 15–21.
- (86) Rangel-Yagui, C. O.; Pessoa Jr, A.; Tavares, L. C. Micellar Solubilization of Drugs. *J. Pharm. Pharm. Sci* **2005**, *8* (2), 147–163.
- (87) Kataoka, K.; Harada, A.; Nagasaki, Y. Block Copolymer Micelles for Drug Delivery: Design, Characterization and Biological Significance. *Adv. Drug Deliv. Rev.* **2012**, *64*, 37–48.
- (88) Shah, D. O. *Improved Oil Recovery by Surfactant and Polymer Flooding*; Elsevier, 2012.
- (89) Rieger, M. *Surfactants in Cosmetics*; Routledge, 2017.
- (90) Golemanov, K.; Denkov, N. D.; Tcholakova, S.; Vethamuthu, M.; Lips, A. Surfactant Mixtures for Control of Bubble Surface Mobility in Foam Studies. *Langmuir* **2008**, *24* (18), 9956–9961.
- (91) Alargova, R. G.; Kochijashky, I. I.; Sierra, M. L.; Kwetkat, K.; Zana, R. Mixed Micellization of Dimeric (Gemini) Surfactants and Conventional Surfactants: II. CMC and Micelle Aggregation Numbers for Various Mixtures. *J. Colloid Interface Sci.* **2001**, *235* (1), 119–129.

- (92) Fujimoto, K.; Yoshii, N.; Okazaki, S. Free Energy Profiles for Penetration of Methane and Water Molecules into Spherical Sodium Dodecyl Sulfate Micelles Obtained Using the Thermodynamic Integration Method Combined with Molecular Dynamics Calculations. *J. Chem. Phys.* **2012**, *136* (1), 014511.
- (93) Andersen, H. C. Rattle: A “Velocity” Version of the Shake Algorithm for Molecular Dynamics Calculations. *J. Comput. Phys.* **1983**, *52* (1), 24–34.
- (94) Straatsma, T. P.; Berendsen, H. J. C. Free Energy of Ionic Hydration: Analysis of a Thermodynamic Integration Technique to Evaluate Free Energy Differences by Molecular Dynamics Simulations. *J. Chem. Phys.* **1988**, *89* (9), 5876–5886.
- (95) Lee, H.; Venable, R. M.; MacKerell, A. D.; Pastor, R. W. Molecular Dynamics Studies of Polyethylene Oxide and Polyethylene Glycol: Hydrodynamic Radius and Shape Anisotropy. *Biophys. J.* **2008**, *95* (4), 1590–1599.
- (96) Klauda, J. B.; Venable, R. M.; Freites, J. A.; O’connor, J. W.; Tobias, D. J.; Mondragon-Ramirez, C.; Vorobyov, I.; Mackerell, A. D.; Pastor, R. W. Update of the CHARMM All-Atom Additive Force Field for Lipids: Validation on Six Lipid Types. *J. Phys. Chem. B* **2010**, *114*, 7830–7843.
- (97) Martínez, L.; Andrade, R.; Birgin, E. G.; Martínez, J. M. PACKMOL: A Package for Building Initial Configurations for Molecular Dynamics Simulations. *J. Comput. Chem.* **2009**, *30* (13), 2157–2164.
- (98) Barlow, D. J.; Thornton, J. M. Ion-Pairs in Proteins. *J. Mol. Biol.* **1983**, *168* (4), 867–885.

- (99) Hansch, C.; Leo, A.; Hoekman, D. *Exploring QSAR: Hydrophobic, Electronic, and Steric Constants*; 1995.
- (100) Schreiber, L. Review of Sorption and Diffusion of Lipophilic Molecules in Cuticular Waxes and the Effects of Accelerators on Solute Mobilities. *J. Exp. Bot.* **2006**, *57* (11), 2515–2523.
- (101) Treiner, C.; Mannebach, M.-H. Correlation Analysis of Solubilization Data in Aqueous Cationic and Anionic Micellar Solutions: Case of the Halocarbons. *J. Colloid Interface Sci.* **1987**, *118* (1), 243–251.
- (102) Fujimoto, K.; Yoshii, N.; Okazaki, S. Molecular Dynamics Study of Free Energy of Transfer of Alcohol and Amine from Water Phase to the Micelle by Thermodynamic Integration Method. *J. Chem. Phys.* **2012**, *137*, 094902.
- (103) Ritter, E.; Yordanova, D.; Gerlach, T.; Smirnova, I.; Jakobtorweihen, S. Molecular Dynamics Simulations of Various Micelles to Predict Micelle Water Partition Equilibria with COSMOMic: Influence of Micelle Size and Structure. *Fluid Phase Equilib.* **2016**, *422*, 43–55.
- (104) Palaiokostas, M.; Ding, W.; Shahane, G.; Orsi, M. Effects of Lipid Composition on Membrane Permeation †. *Soft Matter* **2018**, *14*, 8496–8508.

List of Publications

Chapter 1

Takeda, K.; Andoh, Y.; Shinoda W.; Okazaki, S. Structure of Hydrated Crystal (L_c), Tilted Gel ($L_{\beta'}$), and Liquid Crystal (L_α) Phases of Linear Alkylbenzene Sulfonate (LAS) Studied by X-ray Diffraction and Molecular Dynamics Simulation, *Langmuir*, **2019**, 35 (27), 9011–9019

Chapter 2

Takeda, K.; Andoh, Y.; Shinoda W.; Okazaki, S. Molecular Behavior of Linear Alkylbenzene Sulfonate in Hydrated Crystal, Tilted Gel, and Liquid Crystal Phases Studied by Molecular Dynamics Simulation, *Langmuir*, *Accepted*

Chapter 3

Takeda, K.; Fujimoto, K.; Yoshii N.; Okazaki, S. Molecular dynamics study of solubilization of cyclohexane, benzene, and phenol into mixed micelles composed of sodium dodecyl sulfate and octaethylene glycol monododecyl ether, *J. Comput. Chem.*, *Accepted*

Acknowledgements

I would like to express my sincere gratitude to Professor Susumu Okazaki at Nagoya University, for providing his continuous guidance, encouragement, and valuable discussion, throughout of this study. I am also deeply grateful to Associate Professor Wataru Shinoda, Associate Professor Noriyuki Yoshii, Dr. Yoshimichi Andoh, and Dr. Kazushi Fujimoto at Nagoya University for lending their expertise on MD simulation, and profitable suggestion. I would like to thank all members of Okazaki group for kind support in my student life.

I am gratefully acknowledge people related Kao Corporation; Dr. Tatsushi Wakisaka, Takahiro Kawaguchi, Dr. Atsushi Tanaka, and Hiroki Kubo for giving great opportunity of studying by MD simulation, financial support, and permitting my study as a student; Dr. Takaya Sakai and Yukiko Tabuchi for experimental support and fruitful discussion; Dr. Takuji Kume for useful suggestion and guidance on X-ray scattering; all colleagues of Analytical Science Research Laboratories for valuable discussion and encouragement.

I appreciate the facilities of the Information Technology Center at Nagoya University; the Institute for Solid State Physics, the University of Tokyo; Research Center for Computational Science, Okazaki for the use of supercomputer.

Finally, I would like to express my greatest thanks to my family. Hiromi and Akari Takeda for always believing my endeavor and encourage.

Kosuke Takeda

September 2019